Development of high-speed laser diagnostics for the investigation of scalar heterogeneities in engines

by

Michael E. Cundy

A dissertation submitted in partial fulfillment
of the requirements for the degree of
Doctor of Philosophy
(Mechanical Engineering)
in the University of Michigan
2012

Doctoral Committee:

Professor Volker Sick, Chair
Professor Steven L. Ceccio
Professor James F. Driscoll
Michael C. Drake, General Motors Corporation

You cannot solve what you cannot see.

- Dave Reuss

This dissertation is dedicated to those close to me over the past few years.

ACKNOWLEDGEMENTS

I would like to thank my advisor, Professor Volker Sick, for his guidance over the years in both academic and professional matters. I have been fortunate to have him as my advisor. I would like to thank my peers in my lab who have helped me get acclimated, offered insight into the research process, and helped me with experiments. Their camaraderie helped make these past few years enjoyable. I would like to thank Jay Smith, who has been a close friend and mentor. I would also like to thank Claudia Fajardo, Rui Zhang, Ali Alharbi, Mike Mosburger, Brian Peterson, Kevin Peterson, Louise Lu, and Christopher Jainski. From General Motors, I would like to thank Dave Reuss, Mike Drake, and Todd Fansler for many fruitful discussions. Torsten Schucht, from LaVision GmbH, was a pleasure to work with on measurements with a spark plug absorption probe. Philipp Trunk at the Technische Universitat Darmstadt was a great help in the lab and a great host during my stay in Germany. These experiments may not have been completed without such great help.

The work in TUD was sponsored by the DFG (Deutsche Forschungsgemeinschaft), EXC 259, and General Motors R&D within the GM-UM Collaborative Research Laboratory on Engine Systems Research at The University of Michigan. Dr. Isaac Boxx, from DLR Stuttgart, loaned us a UV objective. Dr. Joachim Deppe, from LaVision Göttingen, provided many fruitful discussions.

TABLE OF CONTENTS

LIST OF FIGURES

LIST OF TABLES

LIST OF ABBREVIATIONS

AOI	Angle of incidence
ATDC	After top-dead center
BTDC	Before top-dead center
CAD	Crank angle degree
DNS	Direct numerical simulation
FOV	Field of view
FWHM	Full width half max
HCCI	Homogeneous charge compression ignition
LIF	Laser induced fluorescence
PIV	Particle image velocimetry
PTV	Particle tracking velocimetry
RANS	Reynolds averaged Navier Stokes
RMS	Root-mean-square
SC	Stratified charge
SG	Spray guided
SIDI	Spark-ignition direct-injection
TDC	Top-dead center

ABSTRACT

The development of advanced engine concepts are, to a large extent, hindered by the lack of suitable multidimensional optical diagnostics that can measure heterogeneities in engines. The combustion process is a complex function of species concentration, temperature, pressure, and flow fields. Fine-tuning the combustion process for efficient combustion with low emissions therefore requires detailed knowledge of these parameters as they vary with space and time. Novel optical diagnostic techniques which probe relevant quantities can either be used to address a specific problem, as with misfires and partial burns in a spark ignition direct-injection (SIDI) stratified charge (SC) gasoline engines; to develop models, such as boundary layer temperature field measurements; or serve both purposes. For these two examples, there are currently no diagnostics which meet the needs of engine developers and modelers, which motivated the current work. Investigations of misfires and partial burns can benefit from novel and improved fuel concentration and combustion progress diagnostics. A high-speed, planar, quantitative fuel concentration diagnostic technique based on laser-induced fluorescence (LIF) of biacetyl was utilized in unison with a spark plug absorption probe to aid in the understanding of both approaches. The LIF diagnostic was improved by using a dual laser approach which increased the signal to noise ratio. Also, its ability to track flame fronts and observe outgassing from engine crevices was demonstrated. The suitability of

the spark plug absorption probe for use in an SIDI SG engine was demonstrated. Next, a simplified combustion progress diagnostic using LIF of hydroxyl radicals was demonstrated, which avoids the cost and complexity associated with conventional approaches. Lastly, a novel, high speed, high resolution LIF diagnostic called two color toluene thermometry was developed to quantitatively measure boundary layer temperature fields. Calibration measurements were performed in a heated jet. The diagnostics were then adapted from a two camera design to a single camera design for simplicity and used to evaluate temperature gradients in an engine boundary layer. The results provided insight into the structure of the boundary layer during different parts of the engine cycle and for different engine operation conditions.

CHAPTER 1
INTRODUCTION

Many, if not all practical thermodynamic systems contain inhomogeneities which must be minimized, maximized, or controlled in some fashion. These inhomogeneities can be temperature (leading to head transfer), pressure, or fluid flow gradients; phase differences; small and large scale mixing; and species inhomogeneities, sometimes as a result of chemical reactions. Internal combustion engines are one such system that can benefit from a better understanding of these types of inhomogeneities.

Rising fuel costs, supply issues, the forecasted demand for fuel, and environmental concerns have cumulatively generated significant interest in developing more fuel efficient vehicles. While many innovative technologies are currently being developed for use in the long term, the improvement of existing technologies such as internal combustion engines (ICEs) is a logical and essential step in the near term. ICEs are low cost, and can run on a variety of fuels.

1.1 Motivation

ICEs can be made more fuel efficient with reduced emissions through the use of different combustion control and design strategies. Engine researchers are primarily

focused on direct-injection engine operation strategies: homogeneous charge compression ignition (HCCI), spark-ignition direct-injection (SIDI) stratified charge (SC), downsizing, partially premixed compression ignition (PPCI), and low temperature combustion (LTC).

The SIDI spray-guided (SG) stratified-charge (SC) gasoline engine has the potential to play a significant role in transportation modes in the future. Some of the work presented in this dissertation will be performed in an experimental engine of this kind. It can improve fuel economy; is capable of being utilized with a hybrid powertrain; has been shown to operate with alternative fuels such as E85, E100, and isobutanol (Smith & Sick, 2007); and can lower emissions. The concept is also well suited to use hydrogen as a fuel since the flammability limits are so broad. In fact, SIDI engines can be designed and coupled with other systems to operate on either hydrogen or hydrocarbon fuels (New York Times, 2008).

Most of the diagnostics described in this work were applied in an optical SIDI SG SC engine. However, the development and methodology of all the work can potentially be applied to other types of engines and environments. For example, the diagnostics may find application in gas-turbine engine research and development. They may also be used to study laboratory flames to facilitate the development of fundamental combustion models.

For SIDI SG SC engines, there is a complex interplay between intake air flows; spray characteristics and penetration of fuel; mixing of fuel, air, and residual combustion

products; compression; heat transfer; and ignition and combustion mechanisms. These processes occur on timescales ranging from microseconds to milliseconds, and with spatial scales ranging from diffusion length scales to several centimeters.

If an engine researcher encounters a problem when investigating ICE performance over various speeds and loads, there are two general approaches that can be taken to resolve the issue, which are summarized in Table 1. Alternatively, if the engine designer hypothesizes that the engine is behaving a particular way and can be engineered to improve performance, they would also utilize the approaches listed.

General Approach	Specific Approaches	Outcomes
Design trial-and-error	• Adjust/modulate intake port geometry • Adjust combustion chamber geometry • Different fuel injection and ignition systems and strategies • Adjust valve timing • Cooling techniques • Attempts to scale designs	• Potential to identify problems • Costly (hardware iterations; time and money)
Optical diagnostics	• Probe relevant quantities (fuel concentration, flow, and temperature fields)	• Potential to identify fundamental problems • Feed models • Guide design
Computational Fluid Dynamics	• Compute relevant quantities	• Potential to identify problems • Guide design

Table 1: Approaches an engine designer can take to resolve a performance issue or improve performance and potential outcomes of such action.

At this point, two problems will be discussed that motivated the research that is presented in this document. The first problem relates specifically to SIDI SG SC engines. The second problem relates broadly to gasoline engines, but the understanding of the

underlying physics may help develop an understanding of gasoline as well as Diesel engines. Both problems are a direct result of heterogeneities in the environment in which they occur. Indeed, all problems in complex thermodynamic system involve heterogeneities, which may include species, temperature, pressure, density, or phase gradients. Developing appropriate methods to measure these heterogeneities is therefore imperative.

The first problem is that the SIDI SG SC engine is susceptible to seemingly random misfires and partial burns. More specifically, sometimes the fuel and air mixture does not burn (misfire) or it only partially burns (partial burn) within an engine cycle. Misfires result in a poor driving experience and high unburned hydrocarbon (UBHC) emissions, which trigger the check engine light in modern cars. Their prevalence depends heavily on the operating conditions. For a relatively stable operating condition with a warm engine at high load with high EGR, misfires can occur less than once out of 100,000 cycles. Partial burns are less noticeable to drivers, but still result in unacceptably high UBHC emissions. For a less stable operating condition, such as idling (~600-800 rpm), these events occur much more frequently.

The problem of misfires and partial burns can be solved with trial-and-error approaches, but the full potential of the engine operation strategy is not realized. For instance, misfires and partial burns can be drastically reduced simply by increasing the spark dwell time and reducing EGR. However, this reduces the life of the spark plugs, and lower EGR means higher peak temperatures and accordingly NO_x production. Other

approaches such as adjusting the combustion chamber geometry may have a beneficial effect on combustion stability, but it is unlikely that a designer could achieve an optimal design without significant guidance from detailed models, which are not yet available. What is needed is the determination of the fundamental cause of these misfires instead of the conditions under which the problem seems to be alleviated. This information would then also help understand cycle-to-cycle variability in these engines, which can lead to further fuel economy improvements. Optical diagnostics are well suited for this since you can probe the quantities of interest.

As the name of the engine implies, the charge, or fuel/air mixture, is heterogeneous. The mixture cannot burn completely without a flammable mixture in the presence of the ignition source at the time of ignition, and subsequently a flammable mixture in front of the propagating flame. Thus, fuel concentration heterogeneities are a necessary quantity to investigate. High-speed, quantitative, planar laser-induced fluorescence (LIF) measurements were developed by Smith and Sick (Smith & Sick, 2005). They used a frequency tripled Nd:YAG laser emitting at 355 nm to excite the tracer biaceytl, which was doped in a non fluorescing base fuel, isooctane, that is often used to represent gasoline. The diagnostics had suitable spatial and temporal resolution to address the problem, but the signal to noise ratio was too low (~5:1). In order for a diagnostic to be routinely used in an industry lab setting, the signal to noise ratio must be 10:1 or higher (Fansler, unpublished). Also, the potential of the diagnostics to identify the flame front and outgassing has not yet been demonstrated.

While the spatial resolution of the LIF diagnostics is desirable so mixing can be visualized, they cannot be used in a production engine because of a lack of optical access. Spark plug absorption probes can be used in production engines. These probes integrate optical fibers and a spark plug into the same housing that fits into the existing spark plug installation hole. These probes can measure many different quantities, including gas phase fuel. An investigation into the suitability of these probes for measurements in SIDI SG SC engines has not yet been done.

Given the potential benefits of the LIF and spark plug absorption probe diagnostics and their current state of development, further development and application is necessary.

Hydroxyl (OH) radicals are often imaged for ignition, propagation, and extinction investigations, so temporally resolved measurements would also be of significant interest in misfire, partial burn, and cycle-to-cycle variability investigations. OH radical emission is either thermally excited (chemiluminescence; resulting from a reaction between H_2 and O_2) or by exciting relatively low temperature OH molecules by absorption of laser light (LIF). High-speed LIF measurements of OH have been utilized in the past but with relatively complex, bulky, and expensive laser systems, so developing a simplified approach is warranted.

The second problem that will be considered is the lack of a detailed understanding of temperature gradients near the cylinder walls and the resulting heat transfer in engines.

This inhibits engine design and performance in different ways. HCCI engine researchers are interested in this knowledge with the hopes that they can utilize bulk temperature heterogeneities to assist in controlling combustion. Engine designers could also utilize this knowledge to increase the compression ratio in gasoline engines while avoiding engine knock. Spatially and temporally resolved temperature information will also provide modelers with data that currently does not exist, and allow for higher fidelity modeling. Better temperature predictions can substantially improve the predictions of NO_x levels, as well as CO.

1.2 Internal Combustion Engines Background

Considerable advances have been made to ICEs over the past century even though the fundamental principles have not changed. ICEs are typically classified as either gasoline or Diesel engines, although modern concepts attempt to marry the most desirable principles of both.

Conventional gasoline engines generate a near-homogeneous fuel-air mixture by injecting fuel into the intake port or directly into the cylinder during the intake stroke and use a spark plug for ignition. To cover the full speed-load range, the intake air is throttled and the fuel is metered such that the desired mixture stoichiometry is achieved. These are the engines typically used in passenger vehicles in the US and are generally desirable because of low noise and pollution levels.

Diesel engines utilize the autoignition phenomenon for ignition. The intake air is often compressed prior to entering the combustion chamber via turbochargers. During the compression stroke, the air temperature rises to a level above the autoignition temperature of the fuel and the fuel is injected near top dead center (TDC). As the fuel evaporates and mixes with the air, combustion begins. The load is controlled solely by the amount of fuel injected. Diesel engines have a higher thermal efficiency than gasoline engines because of their larger compression ratios and lower pumping losses.

1.2.1 Spark-Ignition Direct-Injection Stratified Charge Engine Overview

SIDI SC engines are advanced gasoline engines which bring together Diesel engine fuel economy with the quiet, light weight operation of a conventional port fuel injected (PFI) gasoline engine. This concept is realized by removing the throttle plate in the intake manifold (in the best case scenario) or reducing the throttling, installing the fuel injector into the cylinder head in the combustion chamber, and controlling the load by varying the amount of fuel injected. A flammable mixture is maintained near the spark plug through charge stratification. Fuel efficiency is improved at low, mid, and high loads because pumping losses are minimal.

At high loads, the engine operates similar to a conventional PFI gasoline engine in that a homogeneous mixture is created by the time of ignition. The fuel is injected as a liquid directly into the cylinder, and gasoline evaporates. The mixture is cooler

compared to a PFI engine because of the energy absorbed by the fuel in the evaporation process. For this reason, higher compression ratios or boosting using a turbocharger or supercharger can then be used to improve fuel efficiency while staying below the knock-limit.

In the low to mid load regime, the fuel is injected milliseconds prior to ignition such that a flammable fuel-air charge is made in the region of the spark plug, while the global mixture is lean. Proper charge stratification has been achieved by directing the fuel at a surface (wall-guided systems), varying the levels of air swirl and tumble flow through the intake and cylinder geometry (air-guided systems), or by injecting the fuel at the spark plug (spray-guided (SG) systems) (Zhao, Lai, & Harrington, 1999). The combustion chamber geometry is designed according to the particular strategy. All systems are a combination of the three to some degree, with one strategy being predominant. The latter design is currently the focus of most work in SIDI engine research, including this work, since it offers the best potential for reducing fuel consumption and engine-out emissions.

Fröhlich and Borgmann have shown that this engine has the potential to increase fuel economy by up to 20% compared to a conventional PFI engine (Fröhlich & Borgmann, 2003). Overall, emissions can be reduced through a few measures. Over-fuelling during cold starts, which is a significant source of UBHCs, can be reduced or even eliminated (Arcoumanis & Kamimoto, 2009). Strategies have also been developed using direct injection stratified charges to reduce catalyst warm-up time, such as the

homogeneous-split injection strategy developed by Bosch researchers (Landenfeld, Kufferath, & Gerhardt, 2004). NO_x levels can be reduced since high levels of exhaust gas recirculation (EGR) can be used, lowering peak temperatures (Arcoumanis & Kamimoto, 2009). However, because of the excess air present during combustion, some NO_x is created and a lean NO_x trap is required which (currently) uses precious metals and is therefore expensive.

1.2.2 Misfires and Partial Burns

Until recently, imaging diagnostic techniques for reciprocating engines involved phased-averaging and therefore could only provide limited insight into events that occurred on a per cycle basis. Smith and Sick published the first high-speed fuel imaging technique using planar laser-induce fluorescence (PLIF) to diagnose misfires in 2005 (Smith & Sick, 2005). This work was done in the Quantitative Laser Diagnostics Laboratory (QLDL) at the University of Michigan. They utilized two low speed excimer lasers fired one crank angle degree (CAD) apart to excite the fuel tracer, toluene, and recorded fluorescence followed by hydroxyl (OH) chemiluminescence from the flame that developed using a complimentary metal-oxide semiconductor (CMOS) camera. Three misfires were described. One showed a normal fuel distribution, spark duration, and travel. However, OH signals were observed to travel between the spark plug electrodes to the cylinder head, where the flame extinguished. Another misfire seemed to be a result of an abnormal spark, as determined by a short duration in the images and a

current trace. No OH was observed. No clues were evident in the measurements of the third misfire.

This led Smith and Sick to develop PLIF diagnostics capable of measuring quantitative fuel concentration over several more CADs during each cycle. They utilized the fuel tracer, biacetyl, with frequency tripled Nd:YAG lasers as the excitation source. These diagnostics were used to evaluate misfires with a wider fuel plume multihole fuel injector, which made misfires more prevalent in most cases. One misfire showed a rich pocket of fuel followed by a void in fuel, suggesting that the spark needs to be exposed to the fuel for as long as possible for reliable ignition, or that the spark travelled out of plane and measurements incorporating the 3rd dimension are needed. Another misfire showed leaner than average fuel concentrations, which again suggested insufficient fuel or motion of the spark in the 3rd dimension. Another misfire with showed the fuel plume passing outside of the spark plug gap, on the other side of the ground strap. Increasing the ignition dwell time tended to alleviate misfires, but this in general is an undesirable approach because it would accelerate electrode wear. In the images of some misfiring cycles, the spark discharge appeared to be stagnant within the gap as opposed to stretching into an arc, where it has a better chance of encountering and transferring heat to a flammable mixture. This suggests a lower limit and direction of flow velocities which would push the spark discharge into regions that consistently have a flammable mixture. Three other misfires showed the spark travelling towards the fuel injector when there was a flammable mixture just downstream of the spark plug.

Smith and Sick setup the light sheet to enter the combustion chamber through the axial piston window and in a plane incorporating the spark plug gap and fuel injector (or slightly behind the gap such that the sheet was not blocked by the ground strap). Cundy and Sick later utilized the biacetyl LIF technique in the same engine with different light sheet alignments (Cundy, 2008). One was with a horizontal light sheet, where the sheet passed through the cylinder in the same plane as the spark gap. Fluorescence signals traveled through the axial piston window and were recorded. The salient observation in these measurements was that the cycle to cycle fluctuations were significant, and it was believed to be due to fluctuations in the fuel plume direction or divergence since the fuel plume passed through a large portion of the window on average. The misfire observed by Smith and Sick in which the fuel plume passed below the spark plug would show a high level of fluctuations in this particular data analysis window.

Cundy and Sick also performed volume illumination LIF experiments to measure spatially averaged fuel concentration in the third dimension. The spark discharge typically bows out beyond the spark plug gap in the same direction as the flow, which is known to some extent because of the intake port configuration, so the region just downstream of the spark gap was selected for analysis. This technique suffered from poor signal to noise ratio since the laser intensity was too low. The engine was run under non-optimal conditions to evaluate the diagnostics and verify some past observations made by Smith and Sick. Rich fuel pockets lead to spark abnormalities, possibly because the spark plasma was created in regions with liquid fuel and the energy primarily evaporated the fuel instead of raising the sensible temperature high enough to initiate

combustion. Increasing the ignition dwell time under these experimental conditions considerably reduced the occurrence of misfires. An advanced fuel injection time resulted in misfires that appeared to be due to the lack of fuel.

Smith and Sick's observation of a stationary spark during some misfires suggested a lower limit on flow velocities for successful combustion. Other imaging experiments showed the spark stretching too far, detaching from the electrodes, followed by restrikes, suggesting that there is an upper limit to flow velocities as well (Fansler T. , Drake, Duwel, & Zimmermann, 2006). This motivated the development of high-speed particle image velocimetry (PIV) diagnostics to measure air velocity in-cylinder using Mie scattering of laser light off of silicon oil droplets seeded into the intake air. Fajardo and Sick developed a single laser ultraviolet (UV) PIV system with sub-CAD resolution (Fajardo & Sick, 2007) and later developed a two laser system with the flexibility to measure a wide range of flows at CAD resolution (Fajardo & Sick, 2008). The use of UV light and short exposure times allowed for filtering combustion luminosity, so the flame front could be identified as seeding particles evaporated and burned. Strain rate calculations suggest that the flow is quasi-two dimensional in the plane of the fuel injector and spark plug. The strain rate was also found to increase near the spark plug gap as the piston moved closer to top-dead-center (TDC) in approximately 50% of the recorded cycles. This increase, along with fuel stratification and variations in the spark discharge travel, may hinder flame kernel development.

These PIV measurements were also performed at the General Motors (GM) Research and Development facility in Warren, Michigan, on a newer iteration of the engine by Peterson et al. under motored conditions. The effect of four different spark plug positions (rotated 90° each time) and two different ground strap geometries on the flows were investigated, and the results found similar average velocities and root-mean-square (RMS) values (Peterson, Drake, Fansler, & Sick, 2009).

Drake et al. also utilized the technique under cold-idle conditions in a fired engine. Conditional averages based on IMEP showed minor differences in flow fields between the best and worst burning cycles (Drake, Fansler, Cundy, & and Sick, 2009). Misfires were recorded, but the cause could not be attributed solely to the flow.

Peterson and Sick performed simultaneous fuel imaging with biacetyl and air velocity measurements (Peterson & Sick, 2009). A frequency-doubled Nd:YLF laser was used for Mie scattering off of silicon oil droplets. This work showed no relationship between fuel concentration (in the measured region), spark energy, or flow velocity (in the same region as the fuel was quantified) with misfires. Negative Mie scattering images showed that misfires often occurred when the flame did not travel well into the piston bowl, where most of the fuel resided.

Fansler et al. developed a spark emission spectroscopy technique to measure fuel concentration within the spark in a functional wall-guided SIDI optical engine (Fansler, Stojkovic, Drake, & Rosalik, 2002). The 388 nm CN emission, normalized by the spark

discharge energy at the beginning of the glow phase (early in the spark lifetime), was shown to vary linearly with the equivalence ratio with an uncertainty of less than 10%. The equivalence ratio is integrated over the volume of the spark discharge. These experiments showed appreciable cycle to cycle variations for early injection cases (14%), which are intended to produce homogeneous mixtures. It was found that a slightly rich average equivalence ratio ($\varphi = 1.5$) alleviated misfires and partial burns to some extent. Partial burns were prevalent when the spark timing was delayed by 10 CADs, which resulted in a leaner than optimal mixture at the time of the spark. This prevented robust ignition and rapid flame development since more time was available for fuel transport and mixing, and more regions of the cylinder had mixtures too lean to burn. More recent experiments were done applying this technique to an SIDI SG engine. CH and C_2 emission were used along with CN because of the presence of more liquid fuel. These results suggested that mixtures with an average equivalence ratio of $\varphi = 2.8$ during the observation window were necessary to reduce misfires. This is partially due to the time at which the measurement was taken (early in the spark lifetime, at the beginning of the glow phase), but also because of large cycle to cycle fluctuations (Fansler & Drake, 2006).

Fansler et al. also performed high-speed Mie scattering measurements. Negative Mie scattering images allowed the identification of a 2D flame front. An automated algorithm identified the flame front, and a conditional analysis based on engine indicated mean effective pressure (IMEP) was performed. They then presented probability distribution function contours of the flame front for each case. The primary conclusion

reached was that motion of the spark and early flame kernel towards the cylinder head, as opposed to downwards into the piston bowl where most of the fuel resides, is a significant source of partial burns and misfires (Fansler, Drake, & Böhm, 2008).

Another parameter of significance to this work is the temperature distribution within the cylinder. Along with the local equivalence ratio and flow field, the temperature determines the reactivity of the mixture and therefore plays a role in the direction of flame travel. The use of exhaust gas recirculation (EGR) is essential to reduce in-cylinder temperatures to prevent NO_x from forming, but this reduces combustion stability, so the effects must be well understood. Recent experiments have focused on a single laser source technique to reduce the complexity of the diagnostics. Luong et. al. utilized a low-speed KrF excimer laser to excite toluene in-cylinder and the fluorescence was measured by an intensified camera. The engine was operated under premixed conditions and the precision of the technique was evaluated (Luong, Zhang, Schulz, & Sick, 2008). This technique is extendable to fired engine operation and, to date, no high-speed measurements have been found in the literature.

1.2.3 Temperature and Heat Transfer in Engines

1.2.3.1 Overview

Heat transfer throughout a given engine cycle can vary in time from zero to 10 MW/m^2 and back down to zero in less than 10 ms. Regions 1 cm apart can have heat

fluxes that vary by as much as 5 MW/m^2 (Borman & Nishiwaki, 1987), although engines operating in the HCCI mode can have been shown to have relatively uniform heat flux on the cylinder head and piston crown (Chang, et al., 2004). As a general rule, approximately 30% of the fuel energy is transferred to the cooling system; about half of which is due to in-cylinder heat transfer (Oude Nijeweme, Kok, Stone, & Wyszynski, 2001). Heat flux through the surfaces of the combustion chamber increase with speed and load. However, heat *losses* on a per cycle basis are fractionally larger at lower loads because there is more time for heat transfer.

Heat transfer is governed by the temperature gradient between the combustion chamber gases and the coolant, as shown in Figure 1. For gasoline engines, the primary mode of heat transfer from the combustion chamber gases to the walls is convection. This occurs through the boundary layer, which contains a relatively large amount of mass (10-20%) given its size (Borman & Nishiwaki, 1987). Radiation heat transfer can be neglected, and is only important to consider for Diesel engines because of the relatively high amounts of hot soot (Heywood, 1988). The heat conducts through the cylinder head and engine block, where it reaches a coolant passage.

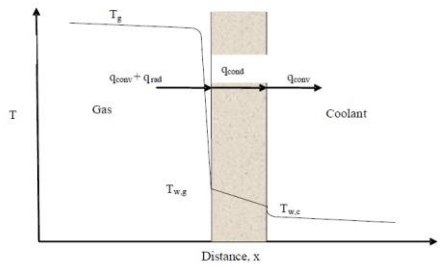

Figure 1: Schematic showing heat flows across the cylinder wall. T_g is the cylinder gas temperature, $T_{w,g}$ is the wall temperature on the combustion chamber side, $T_{w,c}$ is the wall temperature on the coolant side, q_{conv} is heat transfer by convection, q_{rad} is heat transfer by radiation, and q_{cond} is heat transfer by conduction. Image taken from (Alharbi, 2010).

The combustion chamber gas temperature is a function of numerous parameters. In a production vehicle, the intake air is warmed up as it flows through the hot engine compartment (assuming the car has been running). The intake air (or charge) draws heat away from the intake runners, valves, and cylinder head as it enters the combustion chamber. The compression ratio of the engine has a large effect on the core gas temperature and accordingly, temperature gradients. Compression of the gases in an internal combustion engine can be represented as a polytropic process and the core gas temperature throughout the cycle can be estimated using the following equation:

$$T_2 = T_1 \left(\frac{P_1}{P_2}\right)^{\frac{1-n}{n}} \qquad [1]$$

where T_2 and P_2 are the core gas temperature and pressure, respectively, at any time during compression or expansion stroke (without combustion), T_1 and P_1 are the core gas temperature and pressure, respectively, when the intake valve closes (IVC). The quantity n is determined from the slope of the pressure trace on a log-P log-V graph. Typical core

gas temperatures in gasoline engines range roughly span 100°C to 600°C, without combustion. Smith measured temperature fluctuations on the order of 5-10% in the core region (Smith J. R., 1980). These heterogeneities are thought to have a significant influence on the performance of HCCI engines. Later in the engine cycle, when the exhaust valve opens (EVO) or at sometime during the exhaust stroke, the heat flux reverses direction and heat is transferred from the engine to the contents of the combustion chamber. This is attributed to expansion of the boundary layer gases.

Large temperature gradients exist between the core gases and the cylinder walls. The cylinder wall temperature swings throughout an engine cycle are reported to be 30°C or less (Borman & Nishiwaki, 1987). Oude et al. showed temperature swings of 10°C and 1°C for fired and motored (non-fired) measurements, respectively, in their single cylinder 10:1 compression ratio engine (Oude Nijeweme, Kok, Stone, & Wyszynski, 2001). These cyclic swings are superimposed onto temperature gradients that are related to changing engine loads. If an engine has been idling for several minutes and is then accelerated, the temperature gradients and accordingly the heat flux will grow larger. Alternatively, if an engine has been running at full load for an extended period of time and is then idled, the temperature gradients will get smaller.

The heat transfer from the combustion chamber core gases to the wall is a function of the core gas temperature, wall surface temperature, and convection coefficient. While reasonable estimates of the temperatures are currently possible, the

heat transfer problem is complicated because the convection coefficient is a complex function of flow conditions.

Alharbi et al. demonstrated that large scale (relative to the cylinder bore) flow structures can affect the flow structures in the inner boundary layer (Alharbi et al., submitted for publication 2011). Additionally, Lucht et al. demonstrated that increasing swirl can change the boundary layer temperature profile, and accordingly change the heat flux throughout the cycle (Lucht, Walter, Dunn-Rankin, Dreier, & Bopp, 1991). Therefore, these structures must be considered in this context.

1.2.3.2 Heat Transfer Mechanisms Background

Conduction occurs when a temperature gradient exists in a stationary medium, whether it is solid, liquid, or gas phase. The conduction process occurs on the atomic and molecular scale. In non-electrically conducting solids, thermal energy is thought to be transferred via lattice vibrations, and in electrically conducting solids, transport is enhanced by translation of free electrons. In liquids and gases, conduction occurs via diffusion and collisional energy transfer. It can be mathematically described in one dimensional form by Fourier's Law [2]:

$$q_x'' = -k\frac{dT}{dx} \qquad [2]$$

where q''_x is the heat flux (W/m^2); k is the thermal conductivity of the solid, liquid, or gas (W/m*K); T is temperature (K), and x is a distance (m) (Incropera & Dewitt, 2006).

Convection heat transfer occurs at the interface between a fluid and a solid when a temperature difference exists. A velocity boundary layer will always exist in a fluid/surface system, regardless of heat transfer. Surface imperfections and the fluid viscosity cause the fluid velocity to be essentially zero at the surface (no slip condition), and the velocity increases until it reaches the free stream velocity. A thermal boundary layer exists when a temperature difference is present. A schematic showing the (laminar) velocity and thermal boundary layers for the case of a heated surface can be seen in Figure 2. Near the surface, the heat transfer mechanism is essentially diffusion and collisional energy transfer (conduction). Further away from the wall but still within the boundary layer, where velocities are larger, the bulk transport of fluid occurs. The hot (or cold) pockets of fluid can be convected downstream, and will likely mix with the free stream. This bulk motion can be caused by an external source (forced convection), or by buoyancy forces (natural convection). Convection heat transfer is mathematically described by Newton's law of cooling [3].

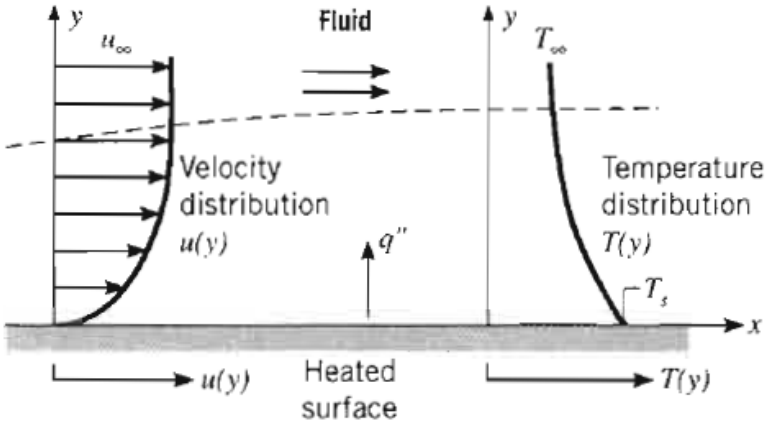

Figure 2: Schematic showing the interaction between a fluid and a surface where heat transfer is present. The velocity boundary layer profile and thermal boundary layer profiles are shown. Schematic courtesy of (Incropera & Dewitt, 2006).

$$q_x'' = h(T_w - T_g) \qquad [3]$$

where h is the convection coefficient (W/m^2*K), T_w is the surface or wall temperature (K), and T_g is the temperature of the fluid that is unaffected by the presence of the wall (K) (Incropera & Dewitt, 2006). It is noteworthy that the convection coefficient is an empirical quantity, and many heat transfer problems are concerned with finding this quantity.

All objects that are at a nonzero temperature emit thermal radiation. This not only includes solid surfaces, but volumetric emission by liquids and gases. Radiation heat transfer in engines is only important for Diesel engines where high levels of high

temperature soot is present (Heywood, 1988), so it is not considered in this work. Other sources can be consulted for detailed information on radiation heat transfer (Incropera & Dewitt, 2006).

1.2.3.3 Boundary Layer and Wall Temperature and Emissions

NO_x formation is exponentially related temperature, so a small change in the estimation of temperature can lead to wildly different NO_x predictions. NO_x has also been shown to increase significantly as surface temperatures increase (Myers & Alkidas, 1978). A further conclusion reached by Myers and Alkidas was that increasing surface temperatures has the effect of decreasing UBHCs, which is desirable, so a tradeoff exists. In HCCI engines, lower wall temperatures have been shown to induce thermal stratifications which decrease peak heat release rates significantly, which has been linked to knocking intensity (Sjoberg, Dec, Babajimopoulos, & Assanis, 2004). The latter is an impediment to extending HCCI operation to high loads. However, lowering the wall temperatures can increase the mechanical wear on the piston rings and cylinder surface, so a tradeoff may be necessary. A detailed understanding of the wall mechanism might allow design of a system where all benefits are realized, at least to some extent.

1.2.3.4 Engine Knock

Engine knock, or preignition, occurs in gasoline engines (with the exception of HCCI) when the fuel/air mixture autoignites as opposed to igniting by a propagating

flame. The reader is encouraged to reference other sources for a more detailed review (Heywood, 1988). Knock creates strong shock waves which can damage the engine. Knock is caused by high temperatures (and assisted by high pressures), so it limits the compression ratio in engines, which in turn limits the thermal efficiency. Unusually high levels of heat transfer (higher by a factor of ~2 compared to a normal cycle) in the local end gas region have been observed under knocking conditions (Borman & Nishiwaki, 1987). The pockets of high temperature result from the following processes (Sjoberg, Dec, Babajimopoulos, & Assanis, 2004):

1) Heat transfer from the fuel/air mixture to the combustion chamber walls
2) The presence of hot residual combustion products from the previous cycle which have not mixed completely
3) Dynamic flow effects during the induction stroke
4) Vaporization of the fuel, especially if injected directly into the cylinder.

These pockets of high temperature gas can be alleviated using a few different trial and error approaches, but gaining a fundamental understanding of processes that result in hot spots is more desirable.

1.2.4 Engine Flows

Bulk flows are engineered to produce three types of flows through design of the intake runner and ports in order to maximize turbulence intensity late in the compression

stroke, in an attempt to control combustion and pollutant formation. These flows are known as tumble, swirl, and squish. The former two patterns can be visualized in Figure 3, and the latter can be visualized in Figure 4. Typical Reynolds numbers encountered in ICEs are approximately 1000, based on the engine bore size.

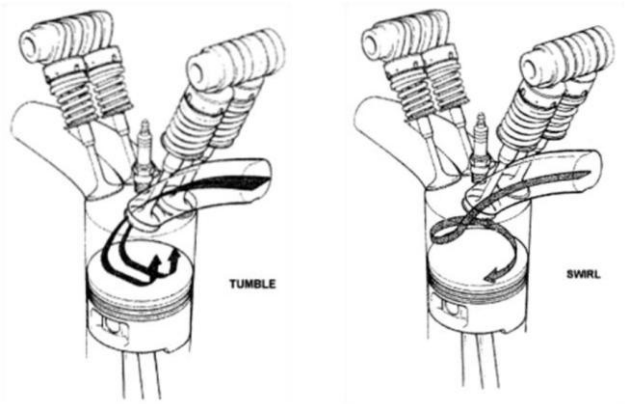

Figure 3: Schematic showing basic tumble and swirl flow patterns. Actual flow patterns will be some combination of the two, as well as squish. Figure courtesy of (Wilson, Watkins, & Dopson, 1993).

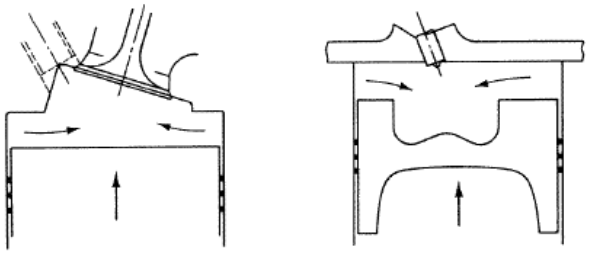

Figure 4: Schematic showing squish in two different geometry engines. In both cases, gas from the periphery of the cylinder is "squished" towards the center of the chamber, where it can enter either the clearance volume (left) or piston bowl (right), or some combination of the two. Image courtesy of (Heywood, 1988).

The turbulent boundary layer velocity profile is described in terms of three different regions. The viscous sublayer is closest to the wall, and the behavior is

dominated by viscous effects. Conduction is the dominant heat transfer mechanism in this region. The velocity increases linearly with distance from the wall. The outer region is the so-called log-law layer, and the two regions are connected by the buffer layer. Heat is transported by conduction and convection in the buffer layer.

Although recent developments in high-speed velocity measurements have greatly improved the understanding of in-cylinder flow fields and turbulence, there is a significant amount of work still to be done. The presence of heat transfer, primarily in the boundary layer regions, complicates attempts to understand and model the problem. In contrast to most engineering problems involving gas compressibility effects (i.e. systems with fluids traveling faster than Mach number of 0.3), boundary layers with heat transfer at substantially lower Mach numbers can have variable density (Liu & Pletcher, 2007). Heterogeneous pressure (and density) distributions might therefore exist in engines. These will affect the flow and should be considered in an analysis. Models have not attempted to include these physics until very recently (Park, 2009).

1.2.5 Heat Transfer Models

Heat transfer modeling began in the early 1920s (Nusselt, 1923). In 1987, it was stated that local, instantaneous heat flux correlations are required for a thorough understanding of the process (Borman & Nishiwaki, 1987), but in 2011 we have not yet made sufficient progress towards this goal (Caton, 2011). Accurately modeling the heat transfer in an engine is a prerequisite for a satisfactory engine performance and emissions

model. Two general approaches have been taken to model heat transfer in engines; phenomenological models, and computation fluid dynamics (CFD) models. Phenomenological models utilize surface thermocouple and heat flux probe measurements with theory to develop correlations. The measurements are assumed to be representative of surrounding regions, which is believed to be an inadequate assumption. CFD models approach the problem from a theoretical standpoint and can therefore allow for a more detailed description of the mechanisms. However, the more detailed the model, the more it costs in terms of computational equipment and time, so there is a firm push to simplify the models which will not subside in the near future. Therefore, direct numerical simulation (DNS), which is the most computationally intensive, will not be discussed.

1.2.3.1 Phenomenological Models

A number of phenomenological (or empirical) models that estimate an instantaneous heat transfer convection coefficient, *h*, have been developed (Eichelber, 1939; Annand, Heat Transfer in the Cylinders of Reciprocating Internal Combustion Engines, 1963; Woschni, 1967; Hohenberg, 1979; Annand & Ma, 1970-1971; Overbye, Bennethum, Uyehara, & Myers, 1961; Huber, Woschni, & Zeilinger, 1990). They are global, in the sense that they do not spatially resolve heat flux. This is done primarily as a simplification to allow for a general description of heat transfer, but the development of advanced engines require a more detailed approach (Caton, 2011). For instance, these

models cannot be used to investigate the cause of hot or cold spots that may develop in engines which influence combustion or thermal stresses.

If a control surface analysis is applied to Figure 1, the radiation and convection heat transfer into the wall is equal to the conduction heat transfer through the engine block (or cylinder head) for steady or quasi-steady conditions. This can be written, as follows:

$$q_{rad} + q_{conv} = q_{cond} \quad [4]$$

If the terms described earlier are substituted into equation 4 (still on a per area basis), the result is as follows:

$$\varepsilon\sigma\left(T_w^4 - T_g^4\right) + h\left(T_w - T_g\right) = -k\frac{dT}{dx} \quad [5]$$

Estimations of the gas core and wall temperatures are necessary for the analysis and are specific to the engine under study. The wall temperature may be estimated using experimental data or correlations. The gas core temperatures are typically calculated for two different regions; burned and unburned regions. The phenomenological models are primarily concerned with determining the convection coefficient. The underlying form of the correlations is as follows:

$$Nu \equiv \frac{hl}{k} = CRe^n \quad [6]$$

where *Nu* is the Nusselt number, *l* is a characteristic length, *k* is the thermal conductivity, *Re* is the Reynolds number, and *C* and *n* are model constants. There are a couple of issues with solving this equation. The constants are tuned to match the performance of a particular engine and therefore cannot be used with confidence to predict the behavior of an engine under development. More details about the selection of these constants can be found in (Heywood, 1988). Since sufficient details about the thermal boundary layer are not known, the temperature (or temperatures) at which gas properties are determined must be estimated. Typically, the average charge temperature is selected. The characteristic length must be selected by the user, which is often the cylinder bore. The velocities used in the calculation are calculated using phenomenological equations using several parameters and constants. For instance, in one popular model, the velocity is calculated using the displaced volume; instantaneous cylinder pressure with combustion; the corresponding cylinder pressure under motored conditions at that time; and the working fluid pressure, volume, and temperature at a reference state. Six different constants are used when the whole engine cycle is considered.

Perhaps the most significant drawback of the phenomenological approach is that it simply does not adequately take into account the physics in the system. For example, the boundary layer gases are thought to expand during the expansion stroke, resulting in heat transfer from the wall to the gases, which was observed experimentally by Oude et al. (Oude Nijeweme, Kok, Stone, & Wyszynski, 2001). A second example can be seen via CFD. Figure 5 shows boundary layer temperature profiles as calculated using a 1D

energy equation by Wendland (Borman & Nishiwaki, 1987). During both the compression (top graph) and expansion strokes (bottom graph), there are cases where heat is transferred from the boundary layer to both the wall and bulk gases, and where heat is transferred to the boundary layer from both the wall and bulk gases.

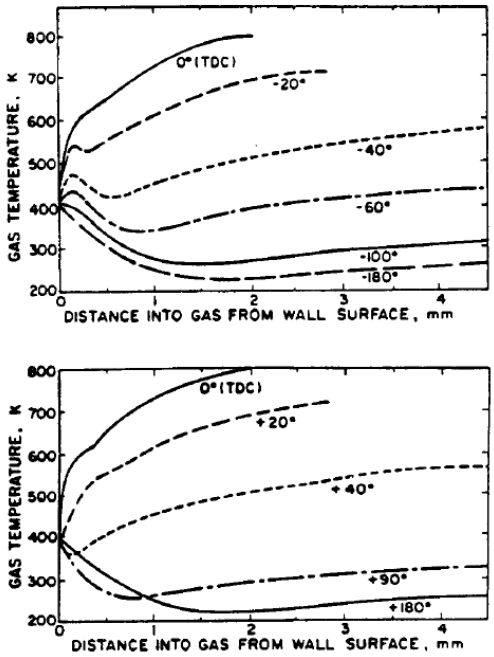

Figure 5: Boundary layer temperature profiles determined via calculation of a 1-D energy equation by Wendland (Wendland, 1968). The top graph shows the profiles during compression, while the bottom graph shows profiles during the expansion stroke. Note that during the expansion stroke, at +40°, the bulk gas temperature is higher than the wall temperature, but the lowest temperature is in the boundary layer and so heat is transferred from the wall to the gas.

Table 2 shows a summary of the global heat transfer correlations that have been developed through surveying specific engines at different operating conditions. The variables are defined as follows; h_i is the convection coefficient (with the subscript *i* used to differentiate between the correlations), C_i is a constant which varies with each model

and can be found in the specific literature, p is cylinder pressure, T is the combustion chamber gas temperature, u_p is the piston velocity, u_i is a specially defined velocity, L is the characteristic length, and V_{inst} is the instantaneous cylinder volume. Of these, the Hohenberg model, which is most often referred to as the modified Woschni equation, is the most popular. The Chang et al. model has been developed for HCCI engines.

Author(s)	Identifier, *i*	Date	Correlation
Nusselt	1	1923	$h_1 = C_1 p^{0.67} T^{0.33} (1 + 1.24 u_p)$
Eichelberg	2	1939	$h_2 = C_2 p^{0.5} T^{0.5} u_p^{0.33}$
Annand	3	1963	$h_3 = C_3 L^{-0.3} p^{0.7} T^{-1.0} u_p^{0.7}$
Woschni	4	1967	$h_4 = C_4 L^{-0.2} p^{0.8} T^{-0.55} u_4^{0.8}$
Hohenberg	5	1979	$h_5 = C_5 L^{-0.2} p^{0.8} T^{-0.4} (u_p + 1.4)^{0.8} V_{inst}^{-0.06}$
Chang et al.	6	2004	$h_6 = C_6 L^{-0.2} p^{0.8} T^{-0.73} u_6^{0.8}$

Table 2: Summary of global heat transfer correlations. More details on the correlations including constants and velocities can be found in the respective references (Nusselt, Der Warmeubergang in der Verbrennungskraftmaschine (the Heat Transfer in the Internal Combustion Engine), 1923) (Eichelber, 1939) (Annand, Heat Transfer in the Cylinders of Reciprocating Internal Combustion Engines, 1963) (Woschni, 1967) (Hohenberg, 1979) (Chang, et al., 2004).

Zonal models have also been developed which divide the combustion chamber up into multiple zones, each of which has their own temperature and convection coefficient history, for investigation. These zones can either be burnt and unburned gas regions, or core and boundary layer regions. The multi-zone approach can be especially useful in SI engines since heat transfer can change dramatically depending on whether the flame has

passed by the particular region under consideration (Heywood, 1988). This is a step in the right direction, but assumptions must be made about where the flame is located (e.g. assuming spherical propagation at some velocity).

1.2.3.2 Numerical Models

Modern numerical models solve the 3D energy, mass, momentum, and turbulence equations in the core region and model the boundary layer region. Species conservation, combustion kinetics, and compressibility effects may also be incorporated into the model, depending on the goal of the investigation. The equations are written in finite difference form and applied to a grid of the system under consideration. The boundary layer can be solved fully with governing equations, but because of the scales involved, too many grid points would have to be added making the model too computationally intensive, so modeling is done for all practical purposes. These are referred to as multi-dimensional models.

Rakopoulos et al. reviewed the four most popular commercial and research models with 1D heat transfer at the walls in a recent paper (Rakopoulos, Kosmadakis, & Pariotis, 2010). These models were developed using data from heat flux probes on various locations within different types of engines, running at different speeds and loads. The generalized one dimensional differential control-volume energy equation is as follows:

$$\underbrace{c_p \frac{\partial(\rho T)}{\partial t}}_{\substack{unsteady \\ term}} + \underbrace{c_p \frac{\partial(\rho v T)}{\partial y}}_{convection} = \underbrace{\frac{\partial}{\partial y}\left[(k + k_t)\frac{\partial T}{\partial y}\right]}_{conduction} + \underbrace{\frac{\partial P}{\partial t}}_{\substack{work \\ term}} + \underbrace{q_{comb}}_{\substack{combustion \\ term}} \quad [7]$$

where c_p is the specific heat of the gas, ρ is the gas density, T is temperature, y is distance from the cylinder wall, k is the laminar thermal conductivity, k_t is the turbulent thermal conductivity, P is the cylinder pressure, and q_{comb} is a volumetric heat addition due to combustion. Different models use various assumptions about the physical environment that allow terms to be neglected, which will be discussed next.

Launder and Spalding neglected the unsteady, convection, pressure work, and combustion terms in their analysis to simplify the problem (Launder & Spalding, 1974). The flow was assumed incompressible, which many researchers have shown to significantly under-predict heat transfer (Rakopoulos, Kosmadakis, & Pariotis, 2010). Angelberger et al. also neglected these terms, but included compressibility effects (Angelberger, Poinsot, & Delhaye, 1997). Han and Reitz developed a similar model but with more detailed expressions of the turbulent conductivity and viscosity (Han & Reitz, 1997). Han and Reitz also tested the unsteady assumptions (the unsteady term and work terms) and combustion source terms and determined that neglecting them did not introduce severe errors. Huh et al. was able to include the unsteady and convection terms, but assumed temporal and spatial temperature variations in the boundary layer were small and negligible (Huh, Chang, & Martin, 1990). Rakopoulos et al. noted that these quantities had non-trivial magnitudes, but tended to be approximately equal and opposite and could cancel out (Rakopoulos, Kosmadakis, & Pariotis, 2010). Their

justification was the result of data taken at multiple locations in two motored SI engines and two motored Diesel engines. While suggestive, this is not a robust conclusion. Oude et al. showed that the convection and work terms were important and must be considered (Oude Nijeweme, Kok, Stone, & Wyszynski, 2001). The convection term accounts for flow normal to the wall as a result of density variations, and it must be considered. The work term is able to account for the expansion of the boundary layer gases, and the associated heat flux reversal during the expansion stroke. Nishiwaki et al. also indicated that the pressure work term was necessary (Nishiwaki, 1998).

After assumptions have been applied to equation 7, the resulting equation is linearized, normalized, and then integrated from the wall up until the first node in the grid. It is quite clear from this development that there is a need for boundary layer temperature field imaging. Although assumptions will always have to be made to develop models, temperature imaging can provide evidence to guide assumptions. For instance, temperature field images can be used to evaluate spatial and temporal temperature variations and resolve the conflicting viewpoints from Huh et al. and Rakopoulos. Also, the interaction of the cold boundary layer with the core gases will shed light on the flow normal to the surface (convection term). For completeness, the final results of the models are shown in Table 3. The quantity y+ is a nondimensional distance (with y being distance from the wall):

$$y^+ = \frac{yu_T}{v} \qquad [8]$$

where u_T is the friction velocity, and v is the kinematic viscosity. The friction velocity is defined as follows:

$$u_T = \sqrt{\frac{\tau_w}{\rho}} \qquad [9]$$

where τ_w is the wall shear stress and ρ is density. Note that the velocity field enters into the heat transfer calculation in the friction velocity term.

Author(s)	Wall Heat Flux	Validity Range
Launder and Spalding	$q_w = \frac{\rho u_T c_p (T_w - T)}{Pry^+}$	$y^+ \leq 11.63$
	$q_w = \frac{\rho u_T c_p (T_w - T)}{Pr_t \left[\frac{1}{\kappa}\ln(Ey^+) + P\left(\frac{\sigma_e}{\sigma_{e,t}}\right)\right]}$	$y^+ > 11.63$
Angelberger et al.	$q_w = \frac{\rho u_T c_p T ln\left(\frac{T_w}{T}\right)}{Pry^+}$	$y^+ \leq 11.63$
	$q_w = \frac{\rho u_T c_p T ln\left(\frac{T_w}{T}\right)}{Pr_t \left[\frac{1}{\kappa}\ln(Ey^+) + P\left(\frac{\sigma_e}{\sigma_{e,t}}\right)\right]}$	$y^+ > 11.63$
Han and Reitz	$q_w = \frac{\rho u_T c_p T ln\left(\frac{T_w}{T}\right)}{2.1ln(y^+) + 2.5}$	$All\ y^+$
Huh et al.	$q_w = \frac{\rho u_T c_p (T_w - T) - 0.5 Pr \frac{dP}{dT}\frac{\nu}{u_T}(y^+)^2}{Pry^+}$	$y^+ \leq 13.2$
	$q_w = \frac{\rho u_T c_p (T_w - T) - \frac{dP}{dT}\frac{\nu}{u_T}(87.12Pr + 2.195y^+ - 28.98)}{13.2Pr + 2.195ln(y^+) - 5.66}$	$y^+ > 13.2$
Rakopoulos et al.	$q_w = \frac{\rho u_T c_p T ln\left(\frac{T_w}{T}\right) - \frac{dP}{dT}\frac{\nu}{u_T}\left(\frac{y^+ - 40}{0.4767 + \frac{1}{Pr}} + 117.31\right)}{\frac{1}{0.4767}\left[ln\left(y^+ + \frac{1}{Pr 0.4767}\right) - ln\left(40 + \frac{1}{Pr 0.4767}\right)\right] + 10.2384}$	$All\ y^+$

Table 3: Summary of the heat fluxes of five different models. The first four are the most widely used, while the latter was published recently. (Launder & Spalding, 1974) (Angelberger, Poinsot, & Delhaye, 1997) (Han & Reitz, 1997) (Huh, Chang, & Martin, 1990) (Rakopoulos, Kosmadakis, & Pariotis, 2010).

It should be noted that a heat transfer model is only as good as the flow field model. As with the thermal boundary layers, the velocity boundary layers are modeled as well because a grid that is capable of resolving the structures would be too small, and

therefore the model would be computationally intensive. The logarithmic law-of-the-wall has been used extensively to model the velocity boundary layer. This approximation was developed for flow with the following characteristics (Oude Nijeweme, Kok, Stone, & Wyszynski, 2001):

1) Steady
2) Incompressible flow
3) Smooth pipes
4) Moderate Reynolds numbers
5) Gradients normal to the wall are much larger than those parallel to the wall
6) Pressure gradient effects are small
7) Turbulence is in local equilibrium
8) Turbulent length scales increase linearly with distance from the wall

Alharbi et al. measured boundary layer velocity fields in-cylinder using a combined PIV and particle tracking velocimetry and compared the data with typical RANS submodels. One of their conclusions was that the logarithmic-law-of-the-wall treatment is not applicable to engine flows. A second conclusion that was reached was that the inner boundary layer is affected by large scale vortical structures. Thermal boundary layers may therefore have a non-trivial impact on combustion. Also, since temperature gradients can be large and result in density gradients, thermal boundary layer information would assist in developing better velocity boundary layer models.

1.2.3.2 Heat Flux and Boundary Layer Temperature Diagnostics

There have been a few studies done investigating thermal boundary layers in engines, and they will be summarized below. Temperature diagnostics and measurements done in bulk flows are not discussed. While they have all been enlightening, each approach has its limitations and more work must be done to extend the knowledge base. Some results of these studies have been presented earlier in the boundary layer overview section and limited portions will be repeated.

Lyford-Pike and Heywood measured density gradients in a square piston engine utilizing Schlieren photography (Lyford-Pike & Heywood, 1984). Sample images from these experiments can be seen in Figure 6, and boundary layer thickness measurements at three locations in the engine can be seen in Figure 7. The physical phenomenon exploited in the Schlieren photography technique is that light bends when it encounters an index of refraction gradient. Less dense media have lower indices of refraction, so gas density gradients will bend light. The flow field of interest is illuminated from the backside relative to the camera, and the light that reaches the camera chip is the first derivative of the density. The gradients are averaged across the depth, or volume, of the cylinder. Therefore, quantitative assessments beyond the thickness of the boundary layer, which would be somewhat arbitrarily chosen, cannot be made. Light that is bent in one direction on the far side of the cylinder can conceivably be bent back in the near side of the cylinder, resulting in no measured density gradient. The authors estimated boundary layer thicknesses by averaging the results over 10 cycles and developed thickness

correlations for different speeds and loads on different surfaces. They found that the boundary layer had a maximum thickness of 2 mm at the end of the expansion stroke on the cylinder wall. The standard deviation of the thicknesses in the individual images was 5%. On cylinder head and piston top, the boundary layers were found to be approximately 2-3 times thicker. Lower engine speeds showed thicker boundary layers, and changing load did not seem to effect the thickness. At EVO, the boundary layer structure became unstable at various positions within the chamber as it mixed with the bulk gas. The temporal resolution of these measurements was sufficient for detailed modeling (2 kHz).

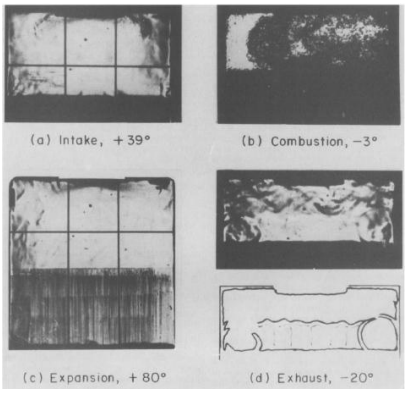

Figure 6: Sample Schlieren photographs taken by Lyford-Pike and Heywood in their square piston engine (Lyford-Pike & Heywood, 1984). The grid was used for spatial calibration purposes. The dark regions in a and b are a result of the piston, and the darker regions in c are a result of deposits from the piston ring.

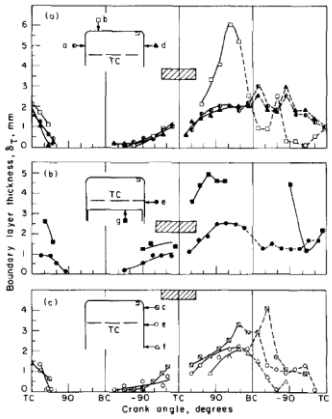

Figure 7: Thermal boundary layer thickness measurements on the cylinder head (top), piston crown (center), and cylinder wall (bottom) as a function of engine position (Lyford-Pike & Heywood, 1984).

Bechtel and Blint utilized laser Raman scattering to measure temperature and species concentration in an atmospheric pressure laminar flame at the interface of a cooled metal plate (Bechtel & Blint, 1980). They quantitatively measured temperatures as close as 150 μm from the wall. Data of this sort is useful for the validation and development of more fundamental models such as Chemkin, but is unable to adequately assist modelers of ICEs where flows are unsteady.

Lucht et al. measured gas temperatures inside of an operational single cylinder optical engine using coherent anti-Stokes Raman scattering (CARS) (Lucht, Walter, Dunn-Rankin, Dreier, & Bopp, 1991). Point-wise measurements (averaged over a cylinder with a diameter of 50μm and length of 2mm) were taken at a particular location within the boundary layer over at least 40 cycles and averaged, and the measurement volume was then translated to measure the temperature at a location closer to or further away from the cylinder head. Therefore, instantaneous spatial gradients were not

visualized, and the structures of the boundary layers of individual cycles were not observed. Also, the measurements were taken in an engine with a cylinder head that was specifically designed for optical measurements near the surface. A schematic cross section of the engine showing this torroidal shaped head can be seen in Figure 8.

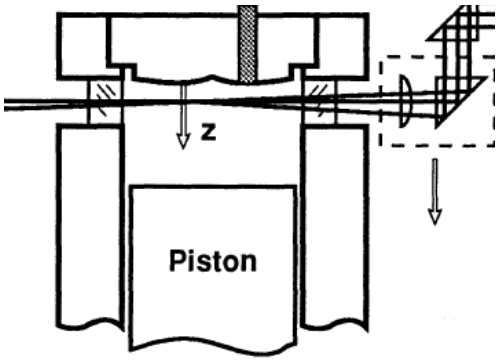

Figure 8: Schematic cross section of the engine used in Lucht et al.'s experiments showing the torroidal cylinder head (Lucht, Walter, Dunn-Rankin, Dreier, & Bopp, 1991).

The intake fuel/air mixture is introduced into the cylinder with a shrouded intake valve, which allowed experiments for high and low swirl cases. These cases resulted in swirl velocities at TDC of 6 m/s and 2 m/s, respectively, as measured at the half radius position. The engine was run at 600 rpm. Scatter in the core region was on the order of 10-20 K. The results of the motored measurements can be seen in Figure 9.

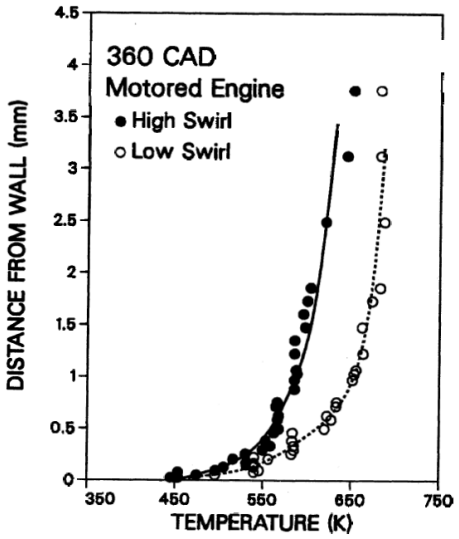

Figure 9: Averaged boundary layer profiles measured in a motored single cylinder optical engine with a torroidal shaped cylinder head using CARS (Lucht, Walter, Dunn-Rankin, Dreier, & Bopp, 1991). Mass flow rates into the engine for the different swirl levels (and intake valves) are different, which explains the ~50°C temperature difference in the core.

Note that there is a steady increase in the temperature even beyond 1 mm. The authors suggest that a potential cause of this is the turbulent transport of cold fluid from the boundary layer to the core region. However, the characteristics and prevalence of these effects and an analysis of the conditions under which they occur cannot be evaluated using this diagnostic technique. The temperature gradient measured in the gas can be extrapolated to the wall, and a heat flux can be estimated using Fourier's law.

The thermal boundary layer thickness was observed to thicken with increasing CAD in the expansion stroke. This is expected because an axial velocity is induced as the piston moves downward. High swirl produced thinner BLs in most combustion cases in the expansion stroke.

The effect of the velocity boundary layer on heat transfer was unclear in these experiments. Thermal boundary layers in high and low swirl cases show differences in motored cases, but in combustion cases the thermal boundary layers are similar. This suggests that conduction or convection in the radial or z directions might be primary drivers (Lucht, Walter, Dunn-Rankin, Dreier, & Bopp, 1991).

There have been many studies in which heat transfer probes have been outfitted into engines (Alkidas, 1980; Yang, Pierce, Martin, & Foster, 1988; Oude Nijeweme, Kok, Stone, & Wyszynski, 2001; Wang & Stone, 2008; Lawton, 1987; Dao, Uyehara, & Myers, 1973; Chang, et al., 2004). Of these, the study by Chang et al. will be discussed to illustrate the approach and some unique results. They outfitted a single-cylinder HCCI engine with several heat flux probes, calculated heat flux by solving the unsteady heat conduction equation assuming one dimensional heat transfer, and evaluated the current models for use in this type of engine (Chang, et al., 2004). The heat flux probes are essentially two thermocouples separated by a wire of known conductivity with surrounding insulation. Seven were installed on the piston crown, and two on the cylinder head. A sophisticated telemetry system was designed and constructed to route the piston probe signals to outside the crankcase. Calculated instantaneous local heat fluxes during the late compression and early expansion strokes and the location of the heat flux probes can be seen in Figure 10. For comparison, similar data for a SI engine is provided in Figure 11 (Cho, 2003). The authors note that the magnitude and shape of the measurements in the HCCI engine experiment are similar, and that a global heat flux correlation may be adequate to describe the phenomena. Indeed, the measurements in the

SI engine show much larger variations. The flame travels past the piston heat flux probes first, and much of the combustion process has taken place before it reaches the squish area of the chamber. However, the data in Figure 10 show variations on the order of 0.6 MW/m^{2}around 20°ATDC, which corresponds to a ~36% difference. In Figure 11, variations as high as 530% are seen around 15°ATDC. While surface heat flux probes certainly generate useful data and further work is warranted, the link between the data and thermo-chemical processes within the combustion chamber gases is missing.

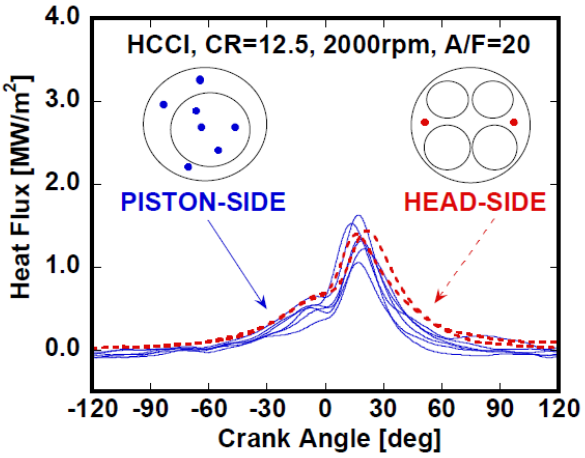

Figure 10: Heat flux in an HCCI engine with a compression ratio of 12.5:1; at 2000rpm; with a lean, homogenous mixture; and 40% exhaust gas recirculation (EGR) (Chang, et al., 2004).

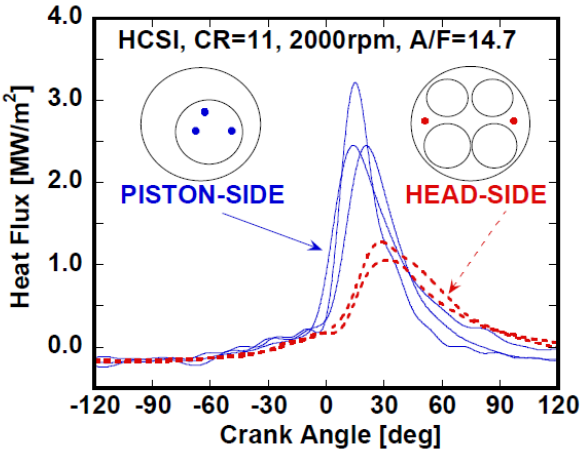

Figure 11: Heat flux in a regular SI engine with a compression ratio of 11:1, at 2000rpm, with a stoichiometric homogenous mixture and 14% exhaust gas recirculation (Cho, 2003).

Dec and Hwang utilized a single-line excitation single band detection planar LIF approach using toluene to measure large scale temperature stratifications in a single cylinder optical HCCI engine (Dec & Hwang). Toluene was premixed with the intake charge for the measurements and assumed to be uniformly distributed at the time the measurements are taken. This is a critical step since oxygen quenches toluene fluorescence, and any variation in the oxygen partial pressure could cause an error in the determination of temperature. Experiments were performed at 1200 rpm, which is believed to be because of a limitation of the laser source used; 1200 rpm is often a transient engine speed that is passed through between idle (600-800 rpm) and cruising speed (2000 rpm). The engine was also motored. Their experiments showed that the temperature was uniform in the bulk gas until about 55°BTDC in the compression stroke, suggesting that an adiabatic core assumption is adequate. Heterogeneities in the boundary layer penetrate into the bulk gas from 30°BTDC to TDC, growing more

substantial as the cycle progresses. Note that these measurements were made in a plane nearly parallel to the surface to avoid surface reflections and to also capture measurements as close to the wall as possible. The authors noted that this plane was 0.8 mm from the surface, but did not specify how this was determined. The images show pockets of hot and cold gas that vary approximately 100°C in magnitude at TDC. These pockets range in scale from 5-11 mm, which is comparable to the clearance volume height of 8 mm. The locations of these pockets show no consistent pattern, suggesting that they are related to turbulence instead of intake flows and chamber geometry. Colder gasses seemed to occur in narrow elongated regions, which could be related to so-called hairpin vorticies that have been observed with PIV and DNS results (Adrian, 2007). The presence of these heterogeneities allows the hottest regions to burn first and the colder regions to burn sequentially, which may reduce the pressure rise rate in HCCI engines. This is critical to extend the range of operation to higher loads.

Dronniou and Dec then utilized the same technique in a plane perpendicular to the cylinder head surface (Dronniou & Dec, 2011). They evaluated averaged, RMS, and individual images; and quantitatively identified structures by thresholding individual images. The averaged images showed no repeatable structures, which again suggested that the heterogeneities were due to random turbulence. RMS images were used to identify that the cylinder head region was the most active in exchanging gas with the core gases. Individual images showed that cold pockets were not isolated within the chamber, but were typically attached to the walls. The threshold images were used to quantify the number of pockets that existed by the cylinder head, in the bulk gas, and by the piston

crown. The number of pockets on the cylinder head and piston crown increased as the cycle progressed, with the number of pockets by the piston crown increasing at a faster rate. Cold pockets near the cylinder head were larger in size compared to the other locations. These measurements also found that the heterogeneities became more substantial as the cycle progressed.

Snyder et al. also utilized the single-line technique together with a two-line technique to evaluate thermal stratifications under fired conditions (Snyder, Dronniou, Dec, & Hanson, 2011). The two line technique provided temperature and air mole fraction measurements to evaluate mixing of residual combustion products of the previous cycle. They observed rapid mixing, and did not suspect that residuals influenced thermal stratifications late in the compression stroke. They utilized the single line technique late in the compression stroke under fired and motored conditions. The development of thermal stratifications during both motored and fired conditions was found to be similar. They observed that wall temperatures affected thermal stratifications.

1.3 Objective and Scope

Thermo-chemical processes are driven by heterogeneities in systems. Advanced ICEs require the development and application of novel diagnostic tools that are capable

of measuring these heterogeneities. The objective of this work is to develop multiple diagnostic tools and to utilize them in engine studies where possible.

Quantitative fuel concentration measurements at high-speeds are important for engine development. LIF of tracer molecules in engines with optical access provides a useful way to investigate fuel heterogeneities in a research environment. Many details of the high-speed biacetyl LIF approach, including biacetyl photophysics, have already been published and will be referenced in this document in lieu of a full description. However, the diagnostics did not have a sufficiently high signal to noise ratio for regular use in industrial laboratories, so improvements were necessary and will be described. Spark plug absorption probes offer a better opportunity for investigations in production, metal engines, although they are lacking in spatial resolution. A study on the suitability of using a spark plug absorption probe for development of SIDI engines has not yet been done and is presented in this work. The design and construction of the probe and electronics has been done by LaVision GmbH and is therefore not addressed in detail in this document.

Hydroxyl radical measurements at time scales relevant to SIDI engines are typically carried out with complex and expensive high-speed dye lasers. The use of a new, simplified excitation source is therefore needed. The suitability of using two solid state lasers (Nd:YAG and Nd:YLF) with internal frequency doubling and external frequency quadrupling was examined. The study was limited to the laser sources already available in the QLDL.

Lastly, a temperature diagnostic approach was selected and developed to produce local, instantaneous 2D temperature field measurements in engines which are independent of tracer number density and have suitable spatial resolution to investigate thermal boundary layers. A feasibility study is performed in the core of a heated jet, and a cooled surface was inserted to evaluate the feasibility of using the diagnostics near surfaces. Experiments are then performed in an optical SIDI gasoline engine. Temperature fields in-cylinder are measured and analyzed. Structures, cycle-to-cycle variability, and boundary layer thickness observations are made. A limited set of engine conditions are considered given constraints of the available equipment. The inclusion of the temperature data in heat transfer models is out of the scope of this work.

CHAPTER 2
OPTICAL DIAGNOSTICS

2.1 Diagnostic Needs, Approaches, and Selection

The reader is encouraged to reference other sources for a more thorough description of the diagnostics (Kohse-Hoinghaus & Jeffries, 2002) (Clemens, 2002) (Eckbreth, 1996) (Demtröder, 1998). What will be presented below are brief summaries of diagnostic approaches and how they relate to the diagnostic needs described in the previous chapter. Each approach generally has its advantages and disadvantages and so the selection of a particular technique can be difficult. The selection of the appropriate fuel diagnostics has largely been done by Smith and Sick, and measuring combustion progress using OH radicals is a well established technique, so these sections will be briefer. Temperature imaging the boundary layer has not been studied thoroughly, and a more detailed discussion will be given here.

2.1.1 Fuel

Instantaneous 2D fuel information can be achieved by a few different means. Raman scattering, Rayleigh scattering, Mie scattering, molecular absorption, and LIF are examples of techniques that can work for species measurements.

In principle, all major species can be determined using the Raman scattering method with a single laser light source. The signals are independent of quenching effects (collisions with other molecules), so the signals are relatively easily interpreted. However, Raman scattering signals are extremely weak, which makes high laser pulse energies a requirement. Currently, some researchers are developing pulse burst laser systems to enable these measurements at high speeds in wind tunnels. However, given the difficulties of operating an optical engine and performing measurements in engines, it is generally advisable to use commercially available laser sources.

Rayleigh scattering refers to light elastically scattered off of molecules, or, more generally, off of particles that mare much smaller than the wavelength of the incident light. Although Rayleigh scattering has been used successfully to measure concentrations of minor species, the analysis of the signal can be very difficult since it is proportional to the total cross section of the mixture, as opposed to the cross section of the species of interest. The signals are low, so high pulse energies are required; this limits the ability to measure signals over a larger field of view. Also, since the scattered light is in the same spectral region as the signal, conventional (unfiltered) measurements near surfaces are nearly impossible. This has been circumvented by filtering out the scattered laser light from the Rayleigh scattering signal based on the Doppler shift in the line shape of the latter. In other words, the spectrum of the light scattered off of molecules will be different from the spectrum of the light scattered off of the surface. This is called filtered Rayleigh scattering. Given the subtle distinction between the signals and the scatter,

stable, narrow band lasers must be used which are not available at high speeds (Yalin & Miles, 1999), so another approach is necessary.

Mie scattering refers to light elastically scattered off of liquid droplets or solid particles. Signal levels are strong, but the results merely indicate the presence of liquid fuel and are qualitative. Gas phase fuel is not measured, which is a significant limitation that prevents these measurements from being very useful for these investigations. Since Mie scattering signals are so strong, it would even be difficult to couple these liquid-phase measurements with another approach, such as LIF, because of dynamic range issues with the detection equipment.

Molecular absorption of light can be used to measure fuel concentration. Stable, narrow band laser sources can be used with knowledge of overlap integrals in the relevant environment, or broadband light sources can be used to determine an effective absorption coefficient. The most significant drawback of this approach is that it measures fuel (or another species of interest) in one dimension. A scanning broadband laser source has been used to measure inhomogeneities, without spatial resolution, which will be discussed later in this section.

The final approach to discuss is LIF. Signal levels are relatively strong, and are spectrally shifted from the laser light which allows for the use of filters to suppress scattered laser light. Recently, high speed solid state laser sources have become commercially available and allow imaging over hundreds of consecutive cycles. This is

the only method currently possible for the type of measurements required for misfire and partial burn investigations.

2.1.2 Combustion

Of the spectroscopic approaches, OH radicals are often used as a combustion progress tracer because it is an approximate marker of the flame front (Warnatz, Maas, & Dibble, 1999). Their high reactivity makes them important to many reactions in the atmosphere and in chain branching reactions in flames (Warnatz, Maas, & Dibble, 1999). Amongst a range of suitable techniques, LIF is the most commonly used to detect OH in flames (Smyth & Crosley, 2002).

OH radicals have been used to study flame wall interactions (Fuyuto, et al., Temperature and Species Measurement in a Quenching Boundary Layer on a Flat-Flame Burner, 2010) (Vlachos, Schmidt, & Aris, 1994). Traditionally, a high speed dye laser system would be used in an investigation of this sort. However, these lasers are complex, bulky, expensive, and sometimes use hazardous chemicals. They also can exhibit saturation effects when operating at high speeds, which can lead to variable and poor beam profiles with varying pulse energies.

Combustion progress is most easily tracked by imaging the natural flame luminosity. However, the results must be interpreted very carefully. Broadband soot emission is often the largest contributor to natural luminosity, and this depends on the

mixture composition. Natural emission from CH molecules is also seen as the blue part of a flame. The results are a qualitative 2D projection of a 3D signal.

Many different LIF strategies have been developed and tested over the years to probe different combustion intermediate molecules because of its high sensitivity. A limited list of probed molecules includes CH, OH, NO, NO_2, C_2, CN, NH, O_2, CO, C_2H_2, H_2CO, O, and H (Clemens, 2002).

2.1.3 Temperature

Schlieren photography can be used to quantitatively determine temperature fields. It is based on the principle that light bends when it encounters a change in index of refraction. In general, less dense gas has a lower index of refraction. If the system of interest is illuminated from the backside relative to a camera by a collimated light source, density gradients will bend the light. The light is focused, and a knife edge is placed at the focal point to block approximately half of the light. Light that is bent towards the knife edge (e.g. razor blade) will get blocked and leave a dark spot on the detector, while light that is bent away from the knife edge will pass and show up as a light spot on the detector. Thus, the orientation of the knife edge determines in which direction density gradients can be visualized. Gradients in the orthogonal direction will not be observed. The first derivative of density is measured. The system can be used near surfaces; can have suitable spatial and temporal resolution; can have a suitable field of view; and is relatively simple. Instantaneous measurements can be made with a pulsed light source.

Quantitative measurements are done by replacing the knife edge with a radial rainbow filter in the place of the knife edge. Bent light rays then result in different colors on the image plane, and the human eye can better distinguish between colors than shades of gray (Clemens, 2002). However, it is unsuitable for an engine environment because it is only suitable for 2D flows. In 3D flows, the density gradients are integrated over the volume of the system, so two density gradients opposite in direction and in the same line of sight could be misinterpreted as a uniform density field. Tomographic approaches have been used in 3-D axisymmetric flows, which is quite different from an ICE environment. The Focusing Schlieren technique allows visualizing density gradients over only a couple of millimeters line of sight, but only gradients in one direction can be observed (Davidhazy, 1998). It is worth mentioning that the principle behind these systems (that light is bent when it encounters density gradients) is a source of error for other diagnostics. This has been discussed in some detail in (Fuyuto, et al., Temperature and Species Measurement in a Quenching Boundary Layer on a Flat-Flame Burner, 2010).

Rayleigh scattering requires a constant pressure and a uniform index of refraction (i.e. local scattering cross sections are constant), such that the changes in the scattering signal can be attributed solely to temperature changes. These assumptions are often made in engine experiments (special fuels are used to ensure a more uniform index of refraction during mixing or combustion) in studies investigating large scale phenomenon, but cannot be made in boundary layers with heat transfer. According to Clemens, the main drawback of this approach is that it assumes equal diffusivities of heat and species (Clemens, 2002). Rayleigh scattering thermometry has been demonstrated at high speeds

(Bork, Bohm, Heeger, & Chakravarthy, 2010). For application to engine boundary layers, there are other, more practical drawbacks; in particular scattered light from the surface.

CARS is a non-linear diagnostic technique where three laser beams of specific wavelengths are overlapped to excite a specific species in the system of interest. The beams are called pump, probe, and Stokes. The species produces a coherent optical signal whose wavelength is equal to the pump beam plus the probe beam minus the Stokes beam wavelengths. This technique generates pointwise temperature measurements and therefore cannot measure gradients, so it is not suitable for this study.

In addition to measuring gas phase concentrations (such as fuel), molecular absorption of light can be used to determine temperature. Typically, two transitions are probed by sending a stable, narrow band laser light beam through an isotropic medium and measuring the transmitted light. With photophysical knowledge of the species of interest, the temperature and species concentration can be calculated. The major drawback of this approach is that it requires a uniform medium. Sanders et al. demonstrated an absorption-based approach in a cell using a laser capable of scanning a broad wavelength range (~30 cm-1) which could determine inhomogeneities . However, there are a few drawbacks. Spatial information is lost. The result is essentially a histogram of temperatures, where the number of bins is inversely related to the error of the approach. Also, an analysis of complex flows may result in substantial errors; a case

in which the authors suggested the technique be developed further into the tomographic realm (Sanders, Wang, Jeffries, & Hanson, 2001).

PLIF of diatomic and polyatomic species is a commonly used thermometry diagnostic. Signal levels are relatively strong, and are spectrally shifted from the laser light which allows for the use of filters to suppress scattered laser light. In engines, NO and OH are commonly used diatomic species. The former is added to the system, while the latter is a combustion intermediate that is present in the flame front and in post-flame gases. Organic molecules have also been used (Einecke, Schulz, & Sick, 2000) (Luong, Zhang, Schulz, & Sick, 2008) (Schulz & Sick, 2005). There are four different approaches to utilizing PLIF for temperature measurements. Generally, all of the PLIF approaches can have adequate spatial resolution, field of view, temporal resolution, can generate quantitative results, and can be applied in engines. However, what separates them is the cost, simplicity, assumptions that are necessary to make them work, and undesirable correction procedures.

The most commonly used PLIF approach uses two laser sources to excite a tracer (two-line excitation) (Grossmann, Monkhouse, Ridder, Sick, & Wolfrum, 1996; Koch & Hanson, 2003; Thurber, Grisch, & Hanson, 1997). The first laser source is fired, and the fluorescence is imaged on a camera, and the second laser source is then fired in close temporal proximity and the fluorescence is imaged on the same camera. The ratio of the signals can be related to temperature, assuming that the local collisional environment and therefore quenching characteristics are the same. One advantage of the technique is that,

if the same tracer molecule is excited by both of the laser sources, tracer concentration can be neglected and a heterogeneous mixture can be imaged. However, differences in beam intensity profiles and pulse energies will bias quantitative measurements and a correction is required which can be difficult and inaccurate. Also, the necessary high speed laser sources can be expensive, especially if the diagnostics require two of them. Specific transitions must be excited in order to extract them temperature information, so tunable dye laser sources are often used. Low speed systems are less expensive, but are still more complex than the solid state lasers used in other PLIF experiments.

PLIF with a single laser source (particularly a solid-state or gas laser) is a simpler and more cost effective compared to the two-line excitation approach. Three single-line excitation approaches are available; single band detection, two-tracer dual band detection, and dual band detection.

The single-band detection is based on absolute signal levels and requires a uniform mole fraction and in-situ calibration. Similar to the two-line PLIF approach described above, the signal must be corrected for laser pulse energy and sheet profile. Hwang and Dec utilized a low speed Nd:YAG laser emitting 266 nm light to excite the tracer toluene with this approach. They normalized the single shot images with an averaged light sheet image for this correction. Their results were presented in terms of relative temperature values (Dec & Hwang, 2009). The main drawback of this approach is that it requires uniform mole fraction. The experiments described in Chapter 3 indicate that it is likely that this is not the case (Cundy, Schucht, Thiele, & Sick, 2009). For

measurements in the boundary layer, large temperature gradients and the resulting density variations would further reduce the reliability of the measurements.

A single-line excitation dual tracer dual detection approach has been used to measure temperature in engines. Two tracers are chosen which have different temperature sensitivities and which fluoresce in different spectral regions upon excitation from a common light source. The signals are spectrally separated using filters and imaged onto two cameras, or a single camera outfitted with image splitter optics. A uniform mixture fraction is not technically required, but the tracers must have equal mole fractions and co-evaporate in the case of seeding the tracers into the fuel spray. Kakuho et al. demonstrated this approach in an HCCI engine using 3-pentanone and triethylamine. A significant assumption that must be investigated in more detail is that the quenching characteristics of triethylamine are multiplicative, and a correction factor can be determined by extrapolating data with various oxygen concentrations (Kakuho, Nagamine, Amenomori, Urushihara, & Itoh, 2006). In engine boundary layers, the diffusivities of the two tracer molecules would have to be considered and either investigated or neglected.

The dual-band detection approach requires only one laser source and an appropriate tracer. The photophysics of the tracer must be that the wavelength shifts to longer wavelengths as the temperature increases. This shift in spectrum is referred to as a red-shift. If the fluorescence is spectrally divided into a lower wavelength band (or channel) and a higher wavelength band, the ratio of the two can be related to temperature.

These diagnostics can be cost effective and relatively simple setups, especially if an image splitter is used to image both channels onto a single camera. This technique has several advantages for this particular study compared to the other PLIF approaches. A uniform mole fraction is not required. Thus, it can be used in engine boundary layers where density is variable. It is also ideal for large scale measurements with heterogeneous mixtures at critical times during the engine cycle such as in SIDI engines. Local laser energy is also divided out in the ratio calculation, so no pulse energy or sheet profile corrections need to be made. The only significant drawback of this approach is that, since the fluorescence signal is divided, it will likely be weak, and high-speed measurements in the boundary layer may be difficult. This particular approach was selected for this study and more details about the system will be discussed next.

2.2 Laser-Induced Fluorescence Background

When the tracer atoms or molecules are illuminated by the laser, a fraction of them absorb the photon energy, *hv*, changing the population of the electrons' rotational, vibrational and electronic energy levels. The excited species then release energy until they reach their ground state through different processes: fluorescence; phosphorescence; and non-radiative processes like collisional quenching, vibrational relaxation, and molecular deactivation. Figure 12 shows an energy level diagram and the various processes that may occur.

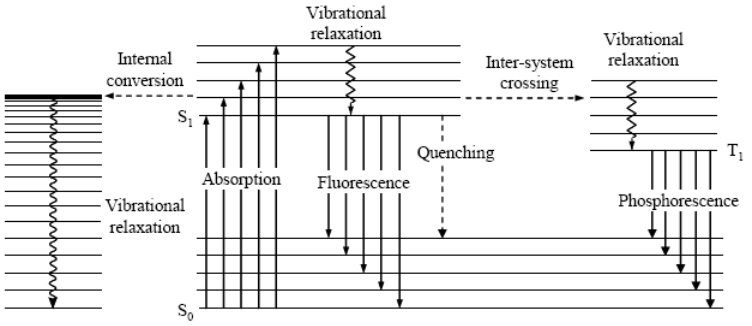

Figure 12: Energy level diagram showing the various processes that an excited molecule may go through to return to its ground state. Image courtesy of R. Zhang (Zhang, 2007).

When an atom or molecule absorbs a photon, it is excited to a higher energy level. The specific transition depends upon the photon energy.

Vibrational relaxation occurs when energy in a vibrational mode of a molecule is transferred into another mode of either the same molecule or a different one. This process occurs until the excited molecules in the system reach a Maxwell-Boltzmann distribution. It is a non-radiative process so the exact nature of the transitions do not need to be characterized, but the effects of these transitions are manifested in photophysical experiments which are discussed later.

Internal conversion is a non-radiative decay process in which energy is redistributed to different modes within the same molecule. Similar to vibrational relaxation transitions, these processes will manifest themselves in photo physical experiments.

Quenching is another non-radiative process which reduces the fluorescence yield. Collisions between an excited tracer atom or molecule and a third body will transfer energy to the latter. The extent to which de-excitation occurs depends on the third body species. Also, since it involves a physical collision, it can be heavily dependent upon temperature, pressure, and the nature of the collision partner.

The last non-radiative process is inter-system crossing. A collision may cause the spin of an electron to reverse, which is referred to as a molecules transition from its singlet to triplet state. At this point, vibrational relaxation may occur, followed by phosphorescence.

Phosphorescence is a radiative process which is very slow because the excited molecule in its triplet state is not able to return to a lower, singlet energy state (a forbidden transition). The integrated phosphorescence emission is much larger than the fluorescence emission, although the intensity at any point in time is generally lower.

Fluorescence is a very fast radiative process, occurring on the order of one to 100 nanoseconds after excitation. It is a spontaneous process. Hence the name of the diagnostic technique, LIF, it is the radiation of interest in this work.

When exciting tracer molecules at relatively weak laser energies, the fluorescence signal is given by the following equation (Einecke, Schulz, & Sick, 2000):

$$S_{LIF} = cI_{Laser}(\lambda)V\left(\frac{X_{tracer}p}{kT}\right)\sigma(\lambda, p, T, y)\varphi(\lambda, p, T, y) \quad [10]$$

where c is the overall efficiency of the collection optics; I_{Laser} is the laser energy density; V is the detection volume; the quantity $\left(\frac{X_{tracer}P}{kT}\right)$ represents the number density of the fluorescing species, which is the product of the mole fraction of the species of interest, X_{tracer}, and the pressure, P, divided by the product of the Boltzmann constant, k, multiplied by the temperature T ; φ is the fluorescence quantum yield (FQY); and y is the mixture composition.

High-speed lasers generally have lower pulse energies compared to low-speed lasers, and since the fluorescence signal is directly proportional to laser energy density the fluorescence signal is often weak. Image intensifiers are commercially available and can boost signal levels. Multi-stage intensifiers can boost signal levels by a factor of several hundred times. These are also utilized to detect light signals in wavelength ranges that are typically not accessible by commercially available detectors. For example, UV fluorescence cannot be detected by modern scientific cameras, but can be detected by intensifiers. The UV fluorescence photons strike the multi-channel plate in the intensifier, which releases electrons. The electrons are accelerated by an electric field, which strike a phosphor screen. The phosphor is excited and fluoresces, which is captured by a standard scientific camera. Note that the spectral information of the fluorescence is lost, and the camera records green or blue light. The performance

characteristics of the intensifiers, including quantum efficiency as a function of wavelength, and of the cameras can be used to estimate the total signal recorded by the camera.

2.3 Laser and Tracer Selection

Researchers have noted several criteria which the tracer must satisfy to be useful (Zhao & Ladommatos, 1998) (Han. & Steeper, 2002):

1. Absorption band accessible by lasers with suitable pulse energies, repetition rates, and beam quality
2. Sufficiently high fluorescence quantum yield
3. Fluorescence is red-shifted enough to effectively spectrally separate it from elastic scattering
4. Well Characterized photophysical properties
5. Non-toxic, stable, and soluble in the fluid it is tracing

2.4.1 Fuel Imaging and Biacetyl Photophysics

Table 4 lists five tracers that have been used in engines studies along with their absorption and emission bands and boiling temperatures. Of the five, Acetone and 3-Pentanone are used more commonly because of their relatively weak temperature and

pressure dependence on fluorescence intensity (Guibert, Modica, & Morin, 2006). These tracers absorb in the mid-UV. In the early 2000s, when Sick sought to develop high-speed fuel imaging diagnostics, commercially lasers that emitted in this band with suitable repetition rates and pulse energy were not available. However, high-speed frequency tripled Nd:YAG lasers were commercially available which could access the absorption band of biacetyl, so this laser and tracer combination was selected.

Tracer	Absorption (nm)	Emission (nm)	Boiling Point (°C)	Heat of Vaporization (kJ/g)
Acetone (CH_3COCH_3)	220-330	330-550	56	0.549
3-Pentanone ($C_2H_5COC_5H_5$)	220-330	330-600	102	0.447
Biacetyl ($CH_3COCOCH_3$)	350-460	440-520	88	0.4499
Toluene ($C_6H_5CH_3$)	230-280	260-330	110	0.4125
p-Xylene (C_8H_{10})	230-280	270-340	138	0.336
Gasoline (for reference)			~121	~0.3489

Table 4: Table listing commonly used fuel tracers and some relevant properties (Zhao & Ladommatos, 1998; Schulz & Sick, 2005; U.S. Department of Energy, 2011)**.**

The photophysics of biacetyl ($C_4H_6O_2$) have been studied for nearly a century and are fairly well known at lower temperatures and pressures. There was very little information on the photophysical properties at temperatures and pressures encountered in engines until a study by Wermuth and Sick (Wermuth & Sick, 2005). The goal of this study was to provide photophysical data for the diagnostics used in this work, so only the radiative transition processes were investigated.

Researchers at Stanford University determined that biacetyls long lasting phosphorescence, which is on the order of milliseconds assuming no collisional quenching or triplet annihilation, is strongly quenched by oxygen and lowers with elevated temperatures. They have shown that phosphorescence disappears at around 200˚C (Lozano, 1992). Smith and Sick spectrally separated the phosphorescence and fluorescence signals during experimentation and noted that phosphorescence was mostly insignificant except at the very early stage of fuel injection when the fuel is relatively cold and the oxygen concentration is low (Smith & Sick, 2005).

Wermuth and Sick studied biacetyl fluorescence when excited by 355 nm light using a small bore single cylinder air-cooled four stroke optical engine as a rapid compression machine. They generated different combinations of temperature and pressure conditions by varying the air intake temperature and pressure and LIF signals were recorded. The air and tracer were mixed in a chamber well before they were introduced into the engine, so the mixture was near uniform. The only variation in fluorescence signal during compression was due to changes in the photophysical properties and number density, the latter of which was corrected for. The LIF measurements account for both the change in FQY and absorption cross section as a result of temperature and pressure (Wermuth & Sick, 2005).

Smith and Sick performed LIF measurements for six different intake pressure and temperature conditions. Intake pressures of 350, 650 and 950 mbar produced peak pressures of 6, 11 and 16 bars, respectively, and intake temperatures of 318 and 368 K

produced peak temperatures of 600 and 700 K, respectively. Forty five images were collected each cycle for 100 consecutive cycles. The images were separated according to their respective CAD and then processed. Background images were also captured and subtracted. A 3x3 sliding average filter was applied and average and RMS images were generated. The images were then corrected for number density effects due to the reduction in volume using a simple geometric correction, and the mass blowby was estimated using the ideal gas law. The results of the experiments can be found in Figure 13. The signal intensity drops with increasing temperature and pressure, and so it will drop as the engine progresses in the compression stroke. The signal is a function of temperature and pressure (i.e. it is single valued), which enables its usage quantitatively (Smith & Sick, 2007).

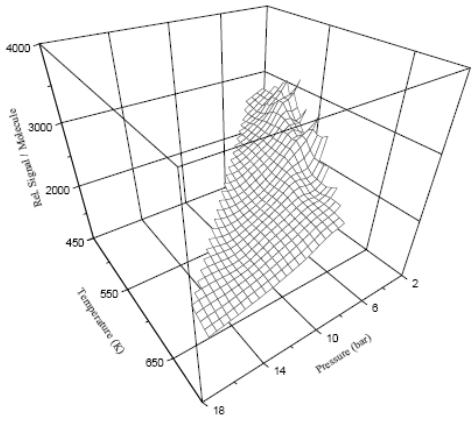

Figure 13: Biacetyl fluorescence intensity as a function of temperature and pressure. This data was measured using an optical engine as a rapid compression machine (Smith J. D., 2006).

2.4.2 Hydroxyl Radical (Combustion Progress) Laser Source

The diatomic OH radical has a pronounced well-resolved rotational–vibrational spectrum that has been characterized comprehensively (Dieke & Crosswhite, 1962) and allows quantum-state specific excitation. LIF detection requires excitation with a laser source that will excite OH to the electronic A state. Typical transitions that have been explored occur at wavelengths between 248 and 320 nm. Tunable dye laser excitation provides the widest flexibility to choose a specific excitation wavelength. Numerous studies have also been performed using tunable excimer lasers. Their simplicity and high pulse energy allowed applications with excitation using weaker transitions, such as the (3,0) band (KrF excimer at 248 nm) and the (0,0) band (XeCl excimer at 308 nm) (Ketterle, Schäfer, Arnold, & Wolfrum, 1992) (Rothe & Andresen, 1997). More recently, a frequency-quadrupled Nd:YAG laser with an intra-cavity etalon was used to excite OH in the (2,0) band (Sick & Wermuth, 2004). This study also showed that fuel LIF tracers, such as acetone or 3-pentanone, can be simultaneously detected with OH radicals. A similar approach was demonstrated with a Nd:YAG pumped dye laser system (Rothamer & Ghandhi, 2003) to study the equivalence ratio near the flame front. Such simultaneous OH/fuel measurements will be important to investigate ignition stability and local combustion progress as a function of mixture conditions in reciprocating engines. OH LIF imaging was demonstrated at a rate of 5 kHz using an Nd:YLF laser pumped dye laser to study turbulent flames (Kittler & Dreizler, 2007), and the same diagnostics were later used in combination with PIV (Böhm, Heeger, Boxx, Meier, & Dreizler, 2009). A burst-mode optical parametric oscillator was used to excite OH radicals at 313.5 nm at up to 50 kHz, but sequences of only up to 100 images can presently be obtained (Miller, Slipchenko, Meyer, Jiang, Lempert, & Gord, 2009). The 283 or 313.5 nm light used for

OH excitation could also be used simultaneously for fuel tracer LIF measurements as well. However, a simplification of instrumentation for simultaneous OH/fuel measurements is desirable.

An attempt was made to externally frequency quadruple an intra-cavity frequency doubled high speed Nd:YAG laser (Quantronix Hawk). Different crystals were evaluated, and it was decided to use a BBO crystal as opposed to a CLBO crystal because of price and durability concerns. The output would have then been tuned to the wavelength used by Wermuth and Sick, but both the frequency doubled light power and conversion efficiency were too low. An inspection of the OH A–X (2,0) band indicated that several absorption lines should fall within the bandwidth of a frequency-quadrupled Nd:YLF laser (263 nm). Externally quadrupling the intra-cavity doubled light proved (somewhat) successful, so this excitation strategy was utilized in experimentation.

2.4.3 Temperature Imaging and Toluene Photophysics

With the particular diagnostic approach for temperature imaging selected, the limited number of tracers that elicit suitable behavior must be considered and one must be chosen. Acetone and 3-pentanone were shown to have emission spectra that are independent of temperature (Großmann et al. 1996, Thurber et al. 1998). To the author's knowledge, no spectrally resolved measurements of biacetyl fluorescence have been made. Ossler et al. reported that naphthalene, fluorine, and pyrene were shown to have a

red shift with increasing temperature when excited at 266 nm (Ossler, Metz, & Alden, 2001). They also suggested that anthracene had a red shift with increasing temperature, but noted that the signal to noise ratio was too low and reliable spectra were not achieved. Kaiser and Long also showed a red shift effect of napthalenes when excited at 266 nm (Kaiser & Long, 2005). Koban et al. reported that a toluene red-shift has been observed when excited by 248 nm and 266 nm laser light (Koban W. , Koch, Sick, Wermuth, Hanson, & Schulz, 2004). Toluene is a major component of commercial gasoline, so it is a good candidate to be used to track the fuel in imaging experiments. Indeed, it is often used. Reboux et al. observed that the LIF signal was proportional to the fuel/air ratio under certain conditions (Reboux, Puechberty, & Dionnet, 1994), which prompted many studies. Later, Koch found that the relationship was more complicated at different conditions and more sophisticated experiments had to be done for the technique to produce accurate results (Koch J. , 2005). Toluene has also been used as a temperature tracer (Luong, Zhang, Schulz, & Sick, 2008; Dec & Hwang, 2009; Luong, Koban, & Schulz, 2006). Given the large potential that toluene has for ICE diagnostics and the potential for simultaneous fuel and temperature measurements, toluene was chosen for the development of the diagnostics in this work.

The photophysics of toluene have been studied since the early 1900s for low temperature or low pressure conditions. It was not until the 21st century that the photophysical behavior was studied for temperature and pressures commonly encountered in ICEs. As mentioned before, mathematically, the parameters that must be understood are the absorption cross section and fluorescence quantum yield in equation

10. These quantities can be used to estimate signal levels and aid in determining the feasibility of diagnostic systems.

Koch et al. measured absorption cross sections as a function of wavelength and temperature using an absorption spectrograph in a shock tube and using lasers in a cell, and the results are shown in Figure 14 (Koch J. , 2005). The reflected shock wave pressures were on the order of 1-2 bar. The wavelengths of two common laser sources, a frequency-quadrupled Nd:YAG (266 nm) and a KrF excimer (248 nm) are identified on the plot with vertical dashed lines.

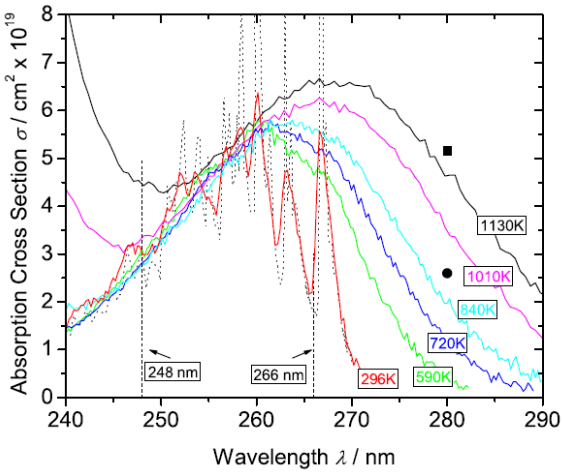

Figure 14: Absorption cross section of toluene as a function of wavelength and temperature. Solid lines and plot courtesy of Koch (Koch J. , 2005). The dotted line represents the absorption spectra at room temperature from (Burton & Noyes Jr., 1968), and the single points at 850 K and 1200 K are from (Hippler, Troe, & Wendelken, 1983). The wavelengths of two common laser sources (266 nm and 248 nm) are identified on the plot as vertical dashed lines).

Wermuth and Sick also reported the absorption cross section of toluene for 248 nm and 266 nm light (Wermuth & Sick, 2005). They used a small bore optical engine

with various intake temperatures and pressures to create different temperature and pressure conditions similar to ICEs. The results of the 266 nm experiments are shown in Figure 15. As of 2005, no investigation has been done to evaluate the pressure dependency of the absorption cross section (Wermuth & Sick, 2005).

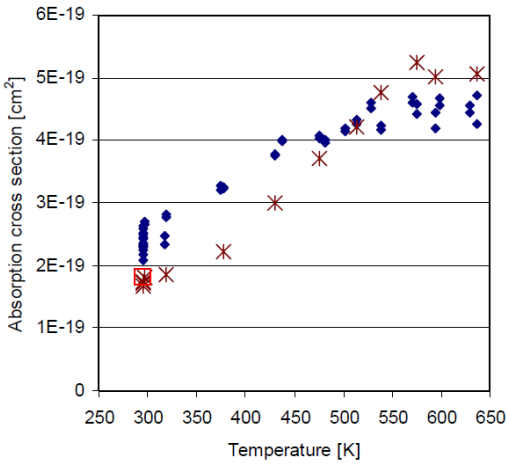

Figure 15: Absorption cross section measurements at 266 nm taken in a small bore optical engine (Wermuth & Sick, 2005). The ◆ show the cross sections determined by LIF measurements using a 266 nm laser, and the ✳ show measurements obtained using a deuterium lamp. The □ indicates measurements from (Koban W. , Koch, Hanson, & Schulz, 2004) taken by 2D LIF.

With this knowledge, the appropriate laser source can be selected. The two most common commercially available lasers emitting in this wavelength are excimer lasers (248 nm) and frequency quadrupled Nd:YAG lasers (266 nm). As mentioned earlier, high temporal resolution measurements are desired (on the order of several kHz). Excimer lasers are generally incapable of reaching such repetition rates while Nd:YAG lasers are, so the latter will be used.

The next parameter to evaluate is the FQY. Unlike absorption cross sections, the FQY will vary with pressure and must be considered when developing diagnostics for use in ICEs. Therefore, the FQY measurements by Koch, which were done at 1 bar (Koch J. , 2005), will not be considered. Wermuth and Sick performed FQY measurements in their optical engine at 266 nm excitation with both nitrogen (Figure 16) and air (Figure 17) as a bath gas. The results are given relative to the yield at room temperature and pressure (Wermuth & Sick, 2005).

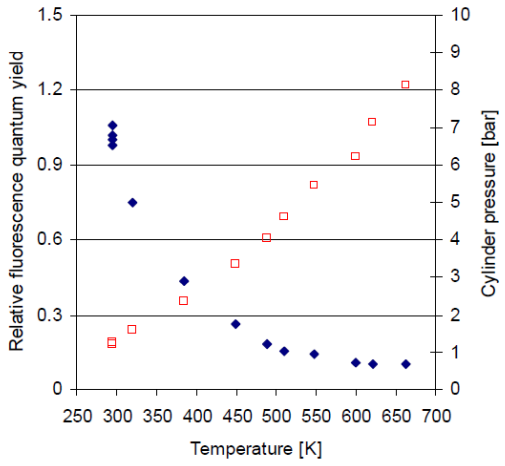

Figure 16: The fluorescence quantum yield for toluene in nitrogen when excited by 266 nm light (Wermuth & Sick, 2005). The ♦ show FQY and the □ indicates cylinder pressure.

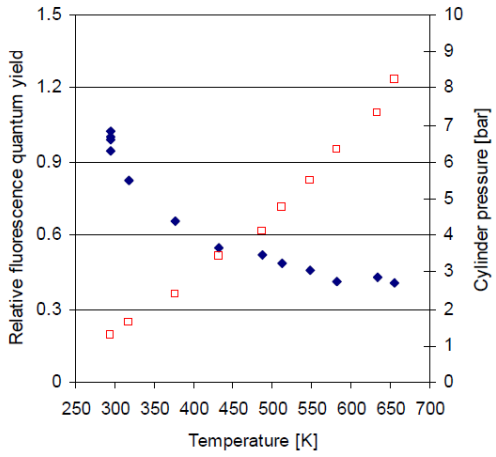

Figure 17: The fluorescence quantum yield for toluene in air when excited by 266 nm light (Wermuth & Sick, 2005). The ◆ show FQY and the □ indicates cylinder pressure.

The absorption cross section and FQY data can be used to estimate signal levels in the early stages of diagnostic development.

It should also be noted that toluene thermal decomposition has been studied in the range of 1500 K – 2200 K (Brouwer, Müller-Markgraf, & Troe, 1988). However, as will be discussed in the following section, the temperature measurement technique used in this work is independent of number density, and therefore thermal decomposition of toluene is not important.

2.4 Two color Laser-Induced Fluorescence Temperature Imaging Principle and System Design

The two color LIF temperature imaging has been demonstrated in the past (Luong, Zhang, Schulz, & Sick, 2008) (Kaiser & Long, 2005) (Zimmermann, Koban, &

Schulz, 2006) (Zimmermann, Koban, & Schulz, 2006). The fluorescence spectrum of certain molecules shifts to longer wavelengths with increasing temperature. A potential reason for this shift based on the structure of the molecule can be found elsewhere (Koch J. , 2005). The toluene fluorescence spectrum when excited at 266 nm can be seen in Figure 18 (Koch & Koban, unpublished). Note that the peak at 266 nm is due to scattered laser light. Also note that the spectrum at each temperature was normalized by its respective maximum signal. If optical filters are chosen such that the fluorescence photons are separated into high and low wavelength bands, then the ratio of the two signals can be correlated to temperature. The closer together the spectral bands are, or the more they overlap, the lower the sensitivity of the diagnostics will be. However, the further apart the bands are, the more fluorescence signal will be lost and the noise levels will be higher. Care must be taken with particular laser/tracer/environment combinations in the interpretation of the ratio. For instance, the fluorescence spectrum of toluene when excited by 248 nm light also red-shifts with increasing oxygen concentration up to 200 mbar, and this affect is additive with the temperature red shift (Koch J. , 2005). Indeed, this phenomenon has been used to measure oxygen concentration in an isothermal jet (Mohri, Luong, Vanhove, Dreier, & Schulz, 2011). When toluene is excited by 266 nm light, no red-shift due to oxygen quenching is observed (Koch J. , 2005).

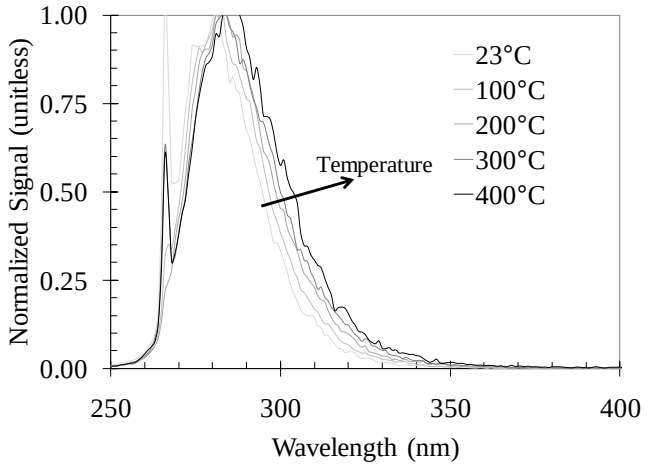

Figure 18: The toluene fluorescence spectrum when excited by 266 nm light has been shown to shift to longer wavelengths with increasing temperature (Koch & Koban, unpublished).

$$\frac{S_{fl}^{red}(x,y,T)}{S_{fl}^{blue}(x,y,T)} = \frac{c^{red} I_{Laser}(\lambda) n_{tot}(x,y) \sigma(\lambda,p,T,y) \varphi_{fl}^{red}(\lambda,p,T,y)}{c^{blue} I_{Laser}(\lambda) n_{tot}(x,y) \sigma(\lambda,p,T,y) \varphi_{fl}^{blue}(\lambda,p,T,y)}$$

$$= c \frac{\varphi_{fl}^{red}(T(x,y))}{\varphi_{fl}^{blue}(T(x,y))} = f(T(x,y)) \qquad [11]$$

The variables in this equation are the same as defined in the previous section, with the exception that the number density term has been replaced by $n_{tot}(x,y)$.

A two camera approach utilizes a 45° image/beam splitter, where one channel transmits and the other reflects. The single camera approach with image splitter taken by Luong et al. is shown schematically in Figure 19 (Luong, Zhang, Schulz, & Sick, 2008). The difference in path lengths of the channels, which will affect the ability to focus, is roughly equal to the distance between the BP 355 image splitter and the aluminum

mirror. In terms of image splitter performance (i.e. channel transmission), a direct comparison cannot be made since the fluorescence was induced by absorption of 248 nm laser light, which resulted in a different spectrum.

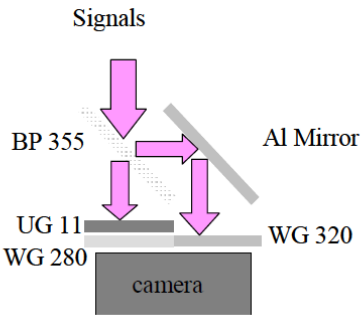

Figure 19: Image splitter approach taken by (Luong, Zhang, Schulz, & Sick, 2008). A bandpass filter centered at 335nm ± 45 nm was used to separate the signals. The blue channel transmitted, and a UG 11 filter and Schott WG 280 long pass filter were used to block scattered laser light. For the red channel, a WG 320 long pass filter was used to block scattered laser light. Note that the difference in path lengths of the signals is roughly equal to the difference between the BP 355 filter and the Al mirror.

CHAPTER 3
SIMULTANEOUS HIGH-SPEED MEASUREMENTS OF FUEL USING LASER-INDUCED FLUORESCENE AND A SPARK PLUG ABSORPTION PROBE

High-speed quantitative fuel distribution measurements have been developed in the past and utilized in SIDI stratified charge engines. The measurements had very good spatial resolution and field of view, but lacked suitable signal-to-noise ratios for regular use in an industrial laboratory. Additionally, the ability of the diagnostics to track the flame front had not been demonstrated, so more work should be done to address these drawbacks. One drawback of the LIF approach is that it requires an optical engine, which is expensive to develop and maintain and cannot easily be adapted to new engine designs. Spark plug absorption probes therefore also have a place in engine development. They can fit in production engines, with little or no modification. The system is suitable for use in an engine in a test stand, outside of a vehicle, or in a stationary vehicle with the hood open.

In SIDI stratified charge engines, the fuel concentration in the vicinity of the spark plug is often the most interesting quantity. Large fuel concentration gradients exist in the vicinity of the spark plug. LIF measurements can come close to measurements within the spark gap, but are limited because of interference of the light sheet with the spark plug and laser light reflections. The spark plug absorption probe also cannot provide measurements in this region. It is a line-of-sight measurement, which likely is

not made exactly where the standard spark plug gap would be. As will be discussed later, the measurement path is offset with respect to the spark plug axis, and the distance between the base of spark plug and the spark gap may not be the same between.

With these differences in mind, the LIF diagnostics were improved and was applied simultaneously with the absorption probe in an optical engine at CAD resolution (3.6 kHz). The suitability of using a spark plug probe in a SG SIDI engine was evaluated. The probe measures infrared absorption of hydrocarbons, carbon dioxide and water to derive fuel and combustion product gas concentrations.

3.1 Background

In contrast to tracer-based measurements via LIF, infrared absorption allows the direct measurement of fuel and an aggregate of combustion product gases (carbon dioxide and water). Molecular absorption of light is governed by the Beer-Lambert law. The absorbance is defined by Equation 12:

$$-\ln\left(\frac{I}{I_0}\right) = \sigma \cdot c \cdot L \qquad [12]$$

where σ is the absorption coefficient, L is the absorption path length, and c is the density of the absorbing species.

Spectrally highly resolved measurements, e.g., using diode lasers, usually require information on wavelength-dependent absorption cross sections that are functions of temperature and pressure. An alternative approach is based on broadband absorption, where the rotation structure of the absorption spectrum is not resolved. A broadband light source is used, and detection covers a large portion of the entire fundamental vibrational band. Integration over the entire rotational manifold is expected to minimize temperature sensitivity. However, vibrational population and line broadening effects due to pressure and temperature may still affect the absorption signal and eventually will need to be quantified. The broadband absorption strategy can make the measurement sensitive to cross talk with absorption by other molecules.

The ability of absorption-based measurements to measure gradients is governed by the theoretical and mechanical design of the diagnostics. Absorption bands in the mid-IR are much stronger than the overtone bands that are often used in tunable diode laser absorption spectroscopy, so path lengths on the order of only a few millimeters are necessary for measurements with a high-signal to noise ratio.

Figure 20 shows the absorption spectrum for CH_4 (representing hydrocarbon fuels), CO_2, and H_2O calculated from the HITRAN database (Rothman, et al., 2005). Note that the absorption bands of hydrocarbon fuels and water overlap slightly. Potential cross talk of water absorption with fuel measurements may occur in cases where large amounts of water are present, although the highest water absorption coefficient is

approximately two orders of magnitude lower in that spectral region. A HITRAN simulation for 600 K (the maximum temperature during our experiments) shows a cross talk of no more than 4%.

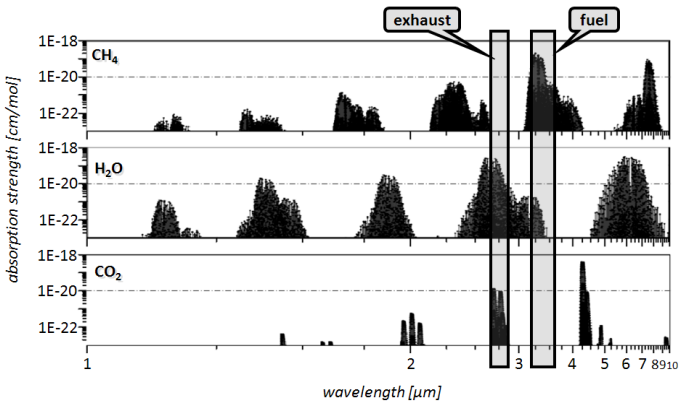

Figure 20: Absorption spectrum of CH_4, H_2O, and CO_2 at 298 K. The spectral simulations used the HITRAN database. Image courtesy of LaVision, GmbH.

A bandpass filter that coincides with the fundamental vibrational–rotational absorption band of hydrocarbons centered at 3.4 μm (0.297 μm width) isolates light that is absorbed by the fuel. Biacetyl also has C─H bonds and will absorb within this band, although the band may be slightly shifted because of the C═O bonds. The net effect of adding biacetyl to iso-octane is not characterized. In general, even if it may be a good assumption to take the absorption coefficient as constant, which is checked as part of this study, the absolute magnitude of the absorption coefficient will depend on the molecular structure and composition of the fuel. A calibration measurement with a known fuel concentration is thus necessary. A bandpass filter centered at 2.7 μm (0.231 μm width) is used to measure the combined absorption by CO_2 and H_2O. Note that at present, the

temperature and pressure dependence of the absorption in this bandpass are not as well quantified as that of the fuel.

The high intensity of the IR lamp combined with sensitive detection allows measurements with high signal-to-noise ratios with potentially significantly lower noise than single-shot LIF imaging. Absorption measurements can therefore be used here as a baseline to assess the precision of the high repetition rate PLIF measurements.

3.2 Engine

A 0.5 L single cylinder SIDI SG SC optical engine was used for experimentation. The lower half is based on a versatile research engine (FEV; Aachen, Germany), and the upper half is a single cylinder version of a four cylinder engine designed and manufactured by General Motors (GM; Detroit, MI). A picture of the research engine can be seen in Figure 21, and a table of engine design parameters can be found in Table 5.

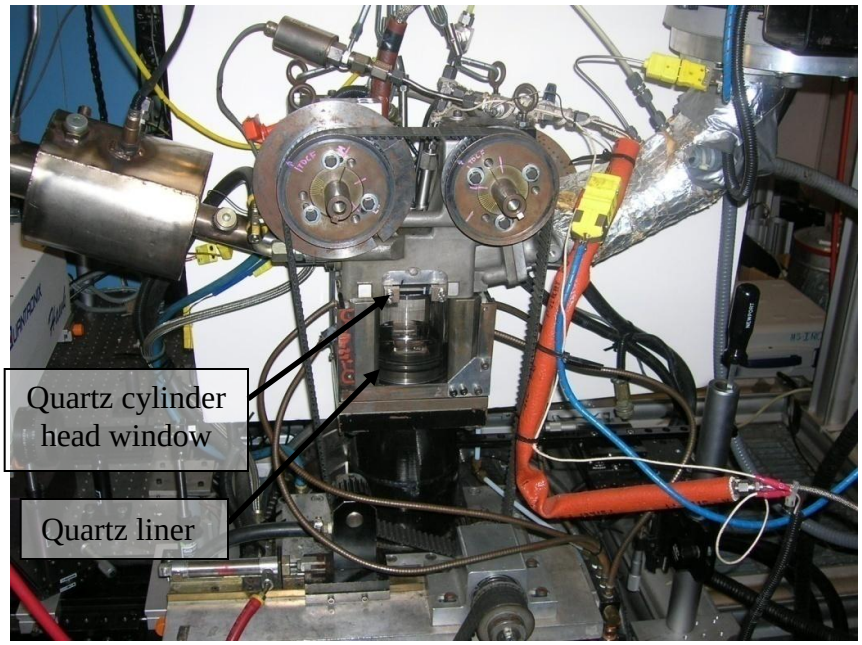

Figure 21: Picture of the optical engine.

Parameter	Value
Bore	8.6 cm
Stroke	8.6 cm
Connecting Rod	15.92 cm
Head Volume	62.24 cm^3
Displacement	499.92 cm^3
Compression Ratio	9:1
Intake Valve Open	362°BTDC
Intake Valve Close	126°BTDC
Exhaust Valve Open	139°ATDC
Exhaust Valve Close	373°ATDC
Valve Lift	10.3 mm

Table 5: Engine design parameters.

The pent roof cylinder head provides real estate for four valves, an 8 hole fuel injector, a spark plug, and a piezoelectric pressure transducer (Kistler; Winterthur, Switzerland). The camshaft phasing, valve lift and valve lift duration are fixed.

Optical access is achieved through a full quartz cylinder and cylinder head windows which expose the head clearance volume. The bowl shaped piston has a window along its axis, and two side windows on the piston which allow access to a bowl in the piston crown. The latter two windows and the cylinder head windows have parallel optical surfaces so light that transmits through them is not distorted. The quartz liner is cylindrical, which causes difficulties when imaging across the boundary of the two windows, particularly when viewing at an oblique angle.

An extended length Bowditch style piston is used in this work. A picture of the piston can be seen in Figure 22. The piston is equipped with carbon compression and rider rings which are soft enough such that the piston and cylinder can be operated unlubricated, reducing the potential for fouling of the optical surfaces. This comes at the expense of relatively high blowby losses (Koban W. , Koch, Sick, Wermuth, Hanson, & Schulz, Predicting LIF signal strength for toluene and 3-pentanone under engine-related temperature and pressure conditions, 2005), but levels are low enough that research on optical engines is justified.

Figure 22: Picture of the bowl shaped piston. Optical access is achieved through an axial window and two side windows which allow access into the bowl.

The crankshaft is linked to a hydraulic dynamometer which can motor the engine or provide resistance when the engine is fired. The hydraulic dynamometer is located in a separate room, enabling better control of the lab temperature and more space to utilize for the optical diagnostics.

The ignition system is comprised of a production ignition coil (Delphi; Troy, MI) and a selection of single-ground strap (ground electrode) spark plugs. Extended length spark plugs are used to reduce surface sparks, where the spark arcs from the hot electrode directly to the cylinder head (Fansler T. , Drake, Duwel, & Zimmermann, 2006), and also to initiate combustion near the center of the chamber. This results in the flame kernel initiating and developing away from the cold surfaces, promoting fast and complete combustion.

Multihole fuel injectors are commonly used in SG SIDI engine research at GM and are used in this work. They have shown to reduce emissions in a wall-guided engine

when compared with swirl-type injectors (Drake, Fansler, Solomon, & Szekely Jr., 2003). Piezoelectric fuel injectors have more repeatable injection characteristics when compared to multihole injectors, but are considerably more expensive and are thus not considered. The fuel injector used in the current work is an eight hole non-valve coverage orifice type (small sac volume) injector (Bosch GmBH; Gerlingen, Germany). It emits plumes with a nominal cone angle of 90˚ at 20˚C, 101 kPa back pressure, and 110 bar fuel pressure, with each plume estimated to diverge at approximately 12˚. The flow rate of the injector at a given fuel pressure was determined by measuring the mass of fuel discharged after a known number of pulses. Single shot injectors such as this one have minimal injection quantity variations from cycle to cycle (unpublished; Scott Parish, GM). The quantities of fuel and fluorescence tracer are measured, mixed, and poured into the fuel tank. Compressed nitrogen pushes the fuel into an accumulator, and a valve is turned to connect this reservoir to the fuel injector. Pressure regulated nitrogen is then introduced into the other end of the accumulator, where it pressurizes the fuel via a piston to 110 bar. A transducer connected near the fuel injector shows pressure fluctuations of ± 5 bar during experiments. A past study by Allocca et al. has suggested that the fuel pressure has a considerably smaller effect on spray plume penetration and evaporation compared with the pressure inside the receiving vessel (Allocca, Alfuso, De Vita, Montanaro, & Rosa, 2004), so these fluctuations were deemed negligible. The fuel injector and fuel are assumed to be at the same temperature as the cylinder head. The cylinder head has oil and coolant at controlled temperatures (typically 95°C, measured at the exit) constantly running through it to simulate a warm engine.

The air intake system is fed by the house air compressor. The air passes through a number of filters to remove oil, water and other suspended particles, and a pressure regulator which is used to control the intake plenum pressure during experiments. For Mie scattering or PIV experiments, part of the flow is diverted through an atomizer allowing tracers (typically silicon oil droplets) to be seeded into the air, and it meets with the bulk of the flow just prior to the intake plenum. For other experiments, including the work presented in this paper, this leg is closed. The air is heated by a screw plug immersion heater (Watlow; Rochester, MI). Following this heater, the air passes through a calibrated critical orifice which enables mass flow rate calculations (using pressure and temperature measurements). Since the flow is chocked in this orifice, pressure fluctuations in the air supply do not propagate downstream, which would affect engine performance. Nitrogen can also be injected through a critical orifice at this point in the system to simulate exhaust gas recirculation (EGR). The air then flows into the intake plenum and then the runner, both of which have a heater and insulation wrapped around them to maintain the desired temperature. The intake runner divides the flow into two ports; one of which is equipped with a butterfly valve that can adjust the level of swirl in the cylinder. In the preliminary work presented here, the engine was operated with the valve fully opened (minimal swirl).

The exhaust pressure, which is measured by a transducer about 1.5 m downstream of the exhaust valve and 1 m downstream of a muffler can to dampen fluctuations, records approximately 0.9 bar during experiments at 600 rpm. EGR can be simulated by introducing nitrogen into the intake system as a proxy. The exhaust is also equipped with

a heated lambda meter (Etas; Ann Arbor, MI) to determine mixture stoichiometry during fired experiments.

The engine is controlled with a personal computer (PC) based engine controller developed by GM. It allows for the adjustment of ignition timing and dwell (time-based), fuel injection timing and duration (time-based), and three auxiliary controls (time-based or CAD-based). This particular controller is only suitable for fixed speed experiments since the timings are controlled manually, but the engine must run correctly at fixed speeds and loads before transient phenomenon can be addressed. Engine encoder signals are sent to a high speed controller (HSC; Lavision GmBH; Gottingen, Germany), which communicates with PC software (DaVis; Lavision GmBH). This allows for the control of multiple cameras, lasers, image intensifiers and other equipment in one program. Features such as the imaging gate, where the cameras only record during desired portions of an engine cycle, make high speed measurements for hundreds of consecutive cycles possible. Currently, run time is limited either by onboard memory in the cameras or fouling of the windows, depending on the experiment.

Data acquisition is accomplished using a high-speed analog-to-digital data acquisition (DAQ) board (CompactDAQ; National Instruments; Austin, TX). Twenty four measurements of pertinent engine parameters (see Table 6) are made at each CAD. Although this time resolution is not necessary for a few of the measurements, it is done for convenience of data handling. A second DAQ is available for spark voltage and current measurements at MHz rates. The signals are transferred to a Labview based

engine data acquisition program (PTrac; Optimum Power Technologies; Pittsburg, PA). Some data processing is done by a complimentary program (PTran; Optimum Power Technologies), which applies calibration offsets and coefficients, generates statistical data using the various measurements and performs a heat release analysis using the Rassweiler-Withrow method.

Recorded Measurements

Cylinder pressure	Torque
Intake manifold pressure	Speed
Intake manifold temperature	Exhaust temperature
Ambient Pressure	Exhaust pressure
Quartz cylinder temperature	Lambda
Coolant inlet temperature	Oil inlet temperature
Ignition voltage	Critical orifice pressure
Ignition current	Critical orifice temperature
Oil pressure	

Table 6: List of engine parameters measured.

3.3 Experimental Setup

As the goal of this work is an in-depth comparison of high-speed PLIF and absorption-based in-cylinder measurements it is imperative that both measurements are conducted simultaneously. The presented measurements are a combination of high-speed CAD resolved planar PLIF measurements recorded with a high-speed intensified camera and absorption measurements using an IR light spark plug sensor. For the results presented below, the engine was run at 600 rpm with the air intake temperature fixed at

45°C. Moisture in the air intake is removed using filters. The air intake pressure was set at either 35 or 95 kPa. 10 mg of fuel were injected with an end of injection of 250°BTDC for the homogeneous experiments, and 40°BTDC for the stratified charge experiment. For the fired engine operation, the spark timing was 30°BTDC. More details on the engine can be found in Table 5 and (Fissenewert, Sick, & Pucher, 2005). A schematic of the PLIF diagnostics setup can be found in Figure 23.

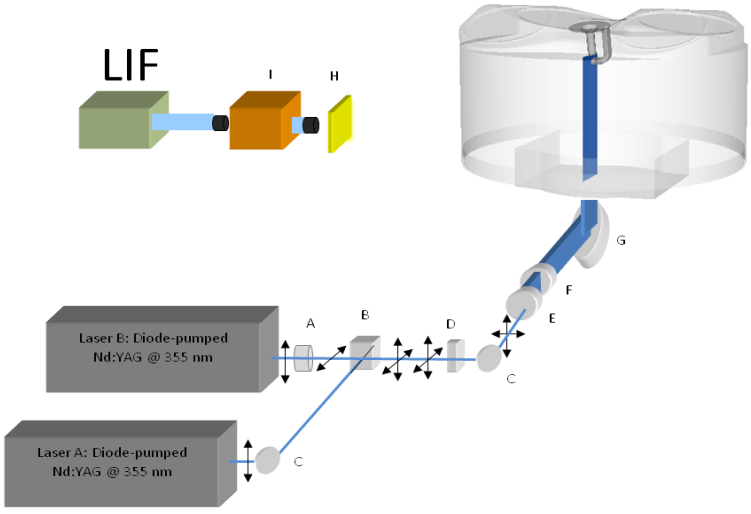

Figure 23: Schematic of the Experimental Setup. Optical elements are identified in the text.

The signal-to-noise ratio of the PLIF images is limited by the low pulse energy of high-repetition-rate lasers. For this experiment, the combined beams of two frequency-tripled Nd:YAG lasers (Quantronix Hawk II) emitting at 355 nm were used to excite the fuel tracer biacetyl (10% by vol.), which was added to the iso-octane base fuel. The beams were made to overlap using a waveplate (A) and a polarizing beam splitter cube

(B) and were fired simultaneously. High transmission at 532 nm/high reflectivity at 355nm mirrors (C) were used to both redirect the beams and remove remnants of frequency-doubled light. A cylindrical lens (+1000mm; D) was used to assist in thinning the light sheet. A second cylindrical lens (−100mm; E) was used to expand the beams in the vertical direction. A sheet-forming telescope (Rodenstock; F) was then used to focus the sheet. The sheet entered the engine between the crankcase and combustion chamber, where it reflected off of a 45° mirror (F) towards the cylinder head.

After traveling through the piston, the light sheet impinged on the cylinder head, extending from the fuel injector to slightly past the spark plug installation hole, bisecting the spark plug electrodes and absorption optical path. A schematic of the spark plug probe can be found in Figure 24, and a schematic of the cylinder head showing the light sheet position and features within the combustion chamber can be seen in Figure 25. Note that one of the eight fuel spray plumes is directed towards the spark plug. Also, note that the spark plug portion of the probe lies ~2 mm in front of the light sheet and the absorption sensor portion lies behind the sheet by about the same distance. The spark plug probe package includes spacers of various thicknesses but cannot in its current form extend far enough into this engine for stable stratified charge operation with the standard injector. The sensor plug is a few millimeters shorter than the standard spark plug for this engine, and thus the fuel plume misses the spark plug. This alleviated concern that liquid fuel would accumulate in the absorption optical path during late injected runs.

Figure 24: Illustration of the spark plug probe architecture (left) and optics (right).

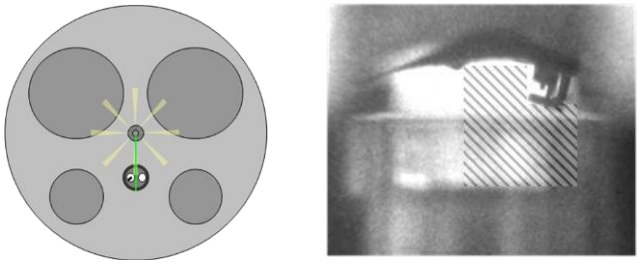

Figure 25: Long exposure image showing the fuel injector, spark plug, piston bowl, and light sheet location.

Images were captured with a high-speed CMOS camera (Vision Research, Phantom v7.3). Signals were digitized at 14 bits and recorded until the 16 GB of on-board memory are filled. The weak LIF signals are amplified with a lens-coupled image intensifier (LaVision, IRO-HS). Synchronization of lasers, camera, and intensifier timing with the engine crank angle position was accomplished with a software-controlled high speed timing unit [LaVision, High Speed Controller (HSC) and DaVis 7.2 software]. This also allowed adjustment of camera parameters and the setting of a gate on the camera and

intensifier triggers to capture images only during the portions of the engine cycle of interest, enabling recording of hundreds of consecutive cycles.

The spark plug sensor system uses an incandescent (tungsten) lamp that is modulated at 30 kHz using a chopper wheel. The modulation is required to record a background signal to account for background signal light that originates from the thermal radiation of the heated gases and stray light. The modulated light travels through a sapphire fiber to the spark plug, enters the cylinder through a sapphire window, is reflected by the mirror, and is transmitted back to the detection unit via a second fiber. The light is spectrally filtered and converted into an electrical signal using a two-stage TE-cooled IR photovoltaic detector (one for each channel). These analog signals were acquired with a 14 bit analog/digital converter (National Instruments) at a rate of 2.5 MHz. The chopper modulation reference signal and the crank angle encoder signals from the engine were recorded at the same rate. All these data were processed online in the sensor electronics to produce CAD resolved data and to split (demodulate) the traces into "light on" and "light off" signals. The data were transferred to a control computer where three additional processing steps were performed to get the desired relative density traces. First, the background (light off) signal was subtracted from the light on signal, resulting in an absorption trace. Then the light intensity I_0 was determined dynamically for each individual cycle as the maximum recorded signal intensity in a given range where the fuel and product gas concentrations are at their lowest levels. The measurement of the reference light intensity through the entire absorption path allows accounting for any fouling of the mirrors or coupling lenses during engine operation. It also compensates for

any potential intensity fluctuations of the incandescent lamp. In principle, I_0 should be measured in the absence of fuel (or exhaust for that channel). Splitting off a fraction of the incoming light and sending it through the same spectral filter bandpass as for the absorption detector would allow accounting for intensity fluctuations due to the lamp but not for window and mirror fouling. This would also require additional detectors. The impact on the accuracy of the absorption measurement when determining I_0 from the highest measured transmission could be assessed quantitatively. Approximately 11% of the gas volume will remain in the cylinder after the exhaust stroke. This amount is given by the compression ratio of the engine (9:1) and the exhaust backpressure. Thus, at any time during the cycle fuel absorption will be measured unless fuel injection is stopped for several cycles to purge the cylinder. Back-to-back measurements with and without fuel injection were conducted and I_0 was determined for both cases. The difference in measured absorbance, which is directly proportional to concentration, is less than 2%. The absorbance measurement with I_0 determined dynamically is lower by this fraction.

Conventional engine parameters were recorded via a high-speed data acquisition system (National Instruments Compact DAQ controlled by Optimum Power software, PTrac) that allows recording of 28 channels at CAD resolution, digitized at 16 bits. The engine crank shaft position signals were first sent to the engine controller, where they were distributed to the spark plug sensor control and acquisition electronics and the data acquisition system mentioned above. The spark plug sensor electronics then relayed the signals to the HSC, which controlled the timing of the laser pulses, camera, and intensifier. All three systems were synchronized to record the same engine cycles.

3.4 Results

Results are presented on the precision, accuracy, and response to large spatial gradients for both measurement techniques. Simultaneously acquired absorption and PLIF data are compared for this purpose for different mixing conditions. A discussion of absorption-based combustion product measurements that were carried out simultaneously with fuel measurements examines the use of broadband mid-IR absorption for aggregate CO_2 and H_2O measurements. Finally, the signal-to-noise ratio for the biacetyl fuel measurements is compared to previous measurements.

3.3.1 Homogeneous Charge Motored Experiments

The signal-to-noise ratio of the absorption measurements (Berg, Beushausen, Thiele, & Voges, 2006) is expected to be higher than that of the PLIF measurements (Smith & Sick, 2006), allowing the absorption data to be used as a benchmark for the precision of the PLIF data. For this purpose, measurements in the motored engine were conducted with early fuel injection (end of injection at 250°BTDC) to produce quasi-homogeneous mixtures around the typical time of ignition. Figure 26 shows the results of this experiment, which also serve as light sheet images to normalize late injection images. An 11 × 12 pixel data analysis window corresponding to approximately 1.2 × 1.3 mm was selected in each PLIF image, the spatial average within the window was calculated, and the resulting values were averaged at their respective CAD over 100 cycles. The location of the window is indicated in the inset picture on the plot. The

ensemble standard deviation was also calculated for both the PLIF and absorbance data and is indicated on the plot as variation bars. The images do not include any corrections (temperature, pressure, number density, etc.), and only a spatial 3 × 3 sliding filter has been applied. The spark plug probe measurements are presented in terms of absorbance [$-\ln(I/I_0)$], corrected for background light. The PLIF data axis was scaled arbitrarily to match the display of the absorbance data at 39°BTDC.

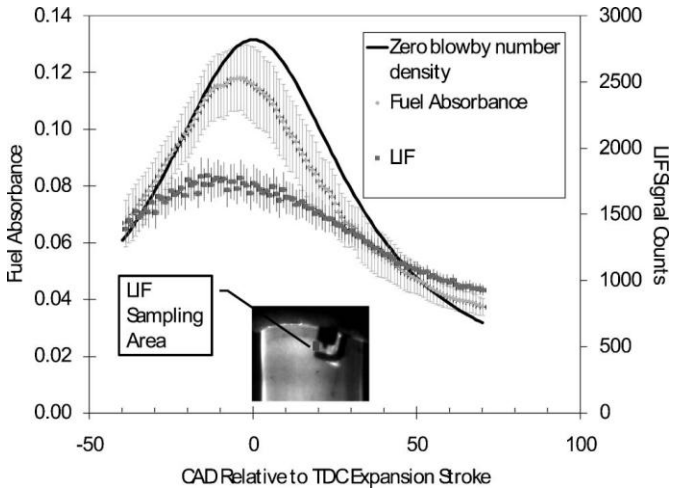

Figure 26: Comparison of the spark plug probe absorption measurements with the PLIF signals in the homogeneous charge motored experiment. The PLIF data are spatially averaged within the rectangle shown (132 pixels) and then averaged at each CAD over 100 cycles. The data contain one standard deviation variation bars. The data reflect the change in number density as the chamber volume changes over the course of the engine cycle. The number density in the absence of engine blowby losses is shown as a solid curve (arbitrary scale).

In the absence of any temperature and pressure effects on the PLIF and absorption signals the signals would vary inversely proportional to the in-cylinder volume once the intake valves are closed (126°BTDC). Thus, a comparison is presented in Figure 26 to a scaled ideal number density value that is pegged to the absorbance data at intake valve

closing. It is noticeable that the absorbance data closely follow the expected number density, but starting at approximately 20°BTDC the absorbance data fall below the expected values. The reason could either be a reduction of the absorption coefficient as pressure and temperature increase or mass loss by blowby across the unlubricated piston rings. The observed magnitude of the signal reduction is commensurate with known significant blowby mass loss (>10%) from the cylinder in unlubricated optical engines (Koban W. , Koch, Sick, Wermuth, Hanson, & Schulz, Predicting LIF signal strength for toluene and 3-pentanone under engine-related temperature and pressure conditions, 2005). The substantial mass loss is also the reason why peak signals for PLIF and absorption are observed before the piston reaches TDC.

The PLIF signal strength does not follow the increase in number density, pointing to a pronounced effect of temperature and pressure on the signal strength. The peak temperature during motored engine operation does not exceed ~600 K (Koban W. , Koch, Sick, Wermuth, Hanson, & Schulz, Predicting LIF signal strength for toluene and 3-pentanone under engine-related temperature and pressure conditions, 2005) at a peak pressure of 15 bars. As mentioned in Chapter 3, the PLIF signal strength for biacetyl after excitation at 355nm drops with increasing pressure and temperature (Smith & Sick, 2006), and for the conditions shown in Figure 26 the observed signal evolution is in good agreement with expectations. A full correction of the presented PLIF signals for temperature and pressure effects would require accurate temperature data. For the given experiments, the engine exhibited unusually high blowby due to a slightly malfunctioning valve; this will cause a higher uncertainty in temperature analysis based on measured in-

cylinder pressure traces. Therefore, only uncorrected PLIF data for the homogeneous engine runs are presented.

The correlation of PLIF and absorbance data are shown in Figure 27 where individual data points from 100 cycles from 39°BTDC to 70°ATDC are plotted. The nonlinearity of this correlation reflects a difference in the temperature and pressure dependence of the signals. Recall that the PLIF data have not been calibrated and have not been processed for temperature and pressure. A PLIF signal decrease with increasing temperature and pressure is expected and is observed, as the highest PLIF and absorption data were measured around TDC where temperature and pressure are highest. This, along with the better correlation of the absorbance data with the in-cylinder volume before 20°BTDC supports the assumption of reduced temperature and pressure dependence of the IR fuel absorption coefficient.

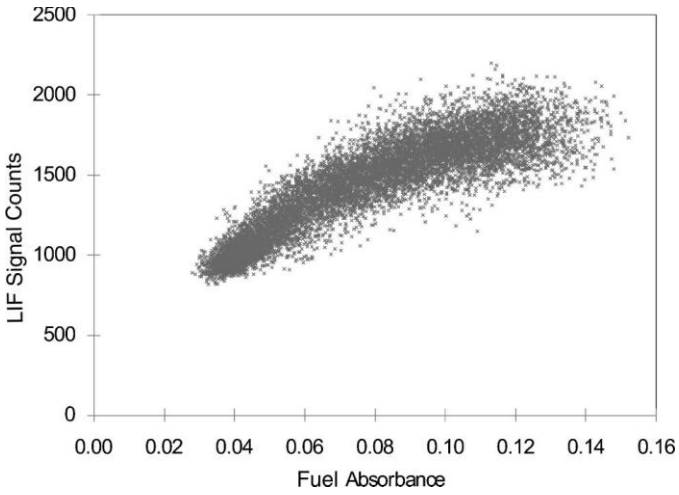

Figure 27: Individual data from simultaneous PLIF and absorption measurements for 100 cycles measured during the homogeneous charge motored experiment. The average and standard deviation of the same data are shown in Figure 26 as a function of CAD and illustrate the change in slope observed here as a pressure and temperature influence primarily on the PLIF signal strength.

An evaluation of the measurement precision is based on the standard deviation of the data from 100 consecutive engine cycles. To eliminate any influence of pressure and temperature on this analysis, the ensemble standard deviation values were normalized by the ensemble average at each CAD. For the PLIF data a spatially averaged signal across 132 pixels was used from within a specified data analysis window as shown in Figure 26. The results are shown in Figure 28. The signal fluctuations for the two measurement techniques are initially higher, and then at TDC for the PLIF signals and after TDC for absorbance data the variation decreases. The measured normalized standard deviation shows that homogeneity is increasing after TDC until fluctuations begin stabilizing at around 5%. The noise level for absorbance was determined to be at or below 1% from transmissivity data ($I=I_0$) from experiments without fuel injection. This marks the lower

noise limit for the entire setup at the engine. The data confirm that local fluctuations in mixture homogeneity remain indeed at a level of 5% for this engine operating condition.

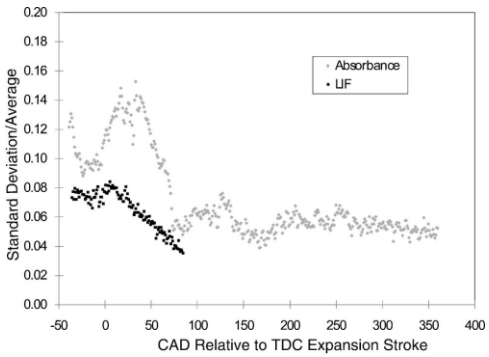

Figure 28: Information on precision for PLIF and absorption measurements from the homogeneous charge motored experiment is available from normalized standard deviation data. Ensemble standard deviation data from 100 consecutive engine cycles normalized by the average at their respective CAD are used to eliminate the influence of pressure and temperature dependence on the signals. Note that the noise limit of the absorption measurements was determined to be 1 % or less from runs without fuel injection. PLIF data are not available after 70°CAD.

3.3.2 Stratified Charge Motored Experiments

The ability to use the absorption measurement to deduce information about fuel concentration and its variation at the spark plug needs to be evaluated. This is important since the spark plug electrodes and absorption path are several millimeters apart from each other and spatial fuel gradients in SG SIDI engines can be very large. Correlations of simultaneously acquired PLIF and absorbance data can be used for this evaluation. It is important to restate, though, that the PLIF measurement volume is between the electrode gap and absorption optical path. Eliminating differences in PLIF and absorption data that stem from temperature and pressure effects is important for this evaluation. Biacetyl

PLIF images from late injection engine runs were normalized with averaged PLIF images from an early injection run. Similarly, absorbance data from late injection runs were normalized with averaged absorbance data from the same early injection run. The relative fuel concentrations that are reported from both measurements could be scaled to equivalence ratios or mole fractions after determining the amount of air present in the cylinder. Given the high blowby losses for the present experiment, the data were not scaled to avoid the introduction of a potential bias error that would depend on engine position. This would not prevent the evaluation and discussion of the fluctuations and the correlations between PLIF and absorbance that was observed but it would also not add any relevant information to the present study, i.e., an assessment of local fluctuations and how different they are at the two measurement locations.

Processed PLIF images (which have been corrected for temperature, pressure, number density, light sheet heterogeneities, etc., as described above) from a single cycle during a late injected motored experiment are presented in Figure 29. This particular image sequence was chosen to illustrate two points. First, it is evident that the fuel misses the spark plug probe on its first pass and is recirculated from the piston bowl back to the cylinder head. From there, the amount of fuel present in the images appears to decrease, suggesting significant fuel motion in the third dimension or outside of the light sheet area. A fuel cloud reaches the data analysis window, shown in the image at 39°BTDC just to the left of the spark gap, at approximately 19°BTDC. Second, a fuel droplet can be seen moving from the fuel injector to the spark plug in the earlier images. The in-cylinder flow in this engine is dominated by a strong tumble flow that is directed

from the fuel injector to the spark gap (Fajardo & Sick, 2007). Using the known temporal separation between images and the spatial scaling it was determined that this droplet is moving at approximately 2 m/s. The separation of the LIF data analysis window and the absorption path is ~6mm. This suggests that the fuel will show up in the LIF images approximately 9–10 CADs before it registers in the absorbance measurements. Figure 30 shows a fuel concentration profile that was extracted from images in the same cycle along with normalized absorbance data for the cycle. LIF data prior to 25°BTDC have been excluded from the plot since an initial offset error in the LIF acquisition rendered images taken prior to this CAD nonquantitative. A temporal shift in the rise of the fuel concentration at the absorbance measurement location is noticeable in the profiles, although to a lesser degree than estimated. Variations on the delay are expected from cycle to cycle since the in-cylinder flow is highly variable. This is especially true near obstructions such as the spark electrodes and the absorption mirror extrusion. The systematic delay in arrival of the fuel cloud at the spark plug sensor is longer in the average data shown in Figure 31. This delay corresponds more closely with the estimated velocity of the droplet. The significant discrepancies between the normalized LIF and absorbance probe signals is likely due to the different probe measurement locations. One of the fuel plumes was directed towards the axis of the spark plug installation hole. The light sheet was aligned between the spark electrodes, and the absorption path and therefore this fuel plume almost fully lies within the path of the fuel spray. Conversely, the absorption path is about 2 mm away from the light sheet, so the LIF data were expected to show different dynamics.

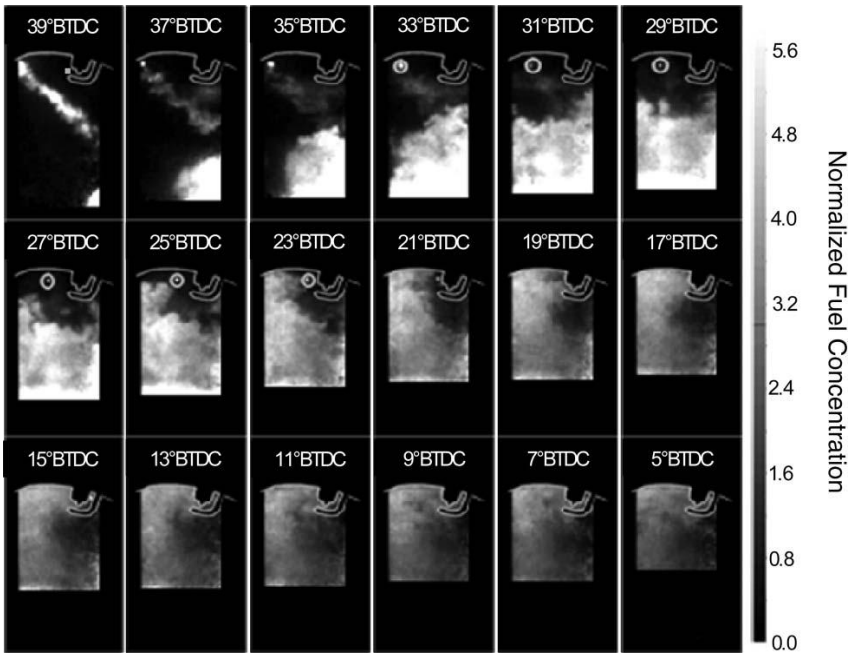

Figure 29: Fully processed fuel concentration images from the late injected motored experiment. These images are used to visualize fuel plume development. Statistical information is also extracted from the data analysis window to the left of the spark electrodes (shown only in the 39°BTDC image for illustrative purposes) and compared to the absorbance measurements. In images from 33 − 23°BTDC, circles are placed in the images to the left of the spark plug to identify a fuel droplet which moves from left to right with the flow field (see text for more details.)

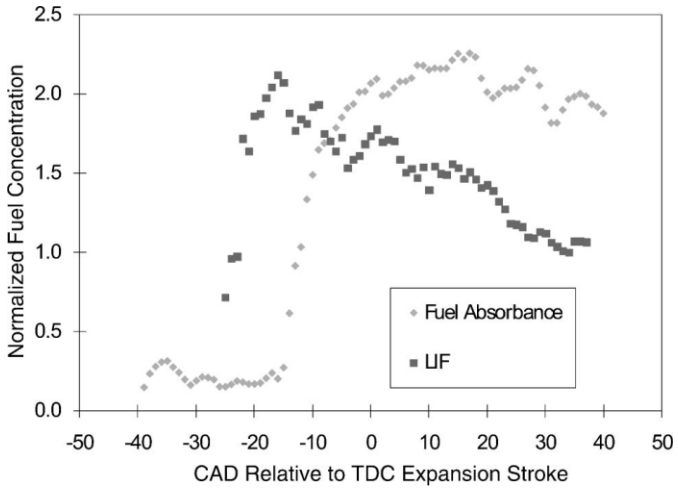

Figure 30: PLIF and absorbance probe fuel concentrations from the cycle shown in Figure 29 from the late injected motored experiment. The PLIF measurement shows the presence of fuel approximately 8 CADs before fuel registers in the absorbance data. This delay is expected from the spatial separation of the PLIF measurement window and spark plug sensor based on the known tumble flow that carried the droplet from left to right in the images in Figure 29.

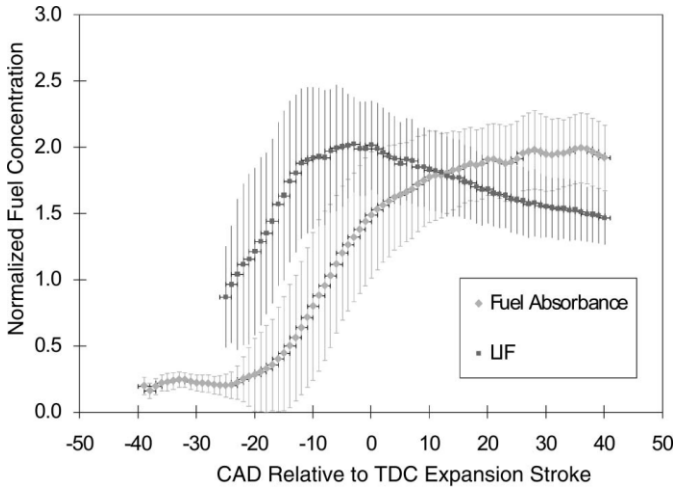

Figure 31: 100 cycle average of quantitative PLIF and absorbance data from the late injected motored experiment normalized by data from the homogeneous charge motored experiment to calibrate the signals (see text for details on calibration). The systematic delay in the arrival of fuel at the spark plug probe is consistent with the estimated droplet velocity that was extracted from Figure 30.

An additional observation can be made in the absorbance data set shown in Figure 30 and Figure 31. Before fuel from the current injection arrives at the measurement location, greater than zero concentrations were measured. There is an expected residual amount of fuel in the cylinder from the previous cycle since the engine is just motored. Figure 32 shows the results of this late injected experiment in scatter plot form. Data from 25°BTDC to 70°ATDC are included in this plot. There are striking differences noticed in comparison to the same assessment of the data from the homogeneous mixture experiment. The large fuel gradients, shown in the images in Figure 29, suggest that there are similar gradients between the location of the LIF measurement volume and the absorption path. The result is that a low correlation is expected, and this is clearly confirmed. It is noteworthy to point out that the LIF data are not expected to drop down

to zero values; the images in Figure 29 representatively show that at this time we already observe fuel at the LIF detection volume, while it is plausible that the absorption path does not yet have significant levels of fuel in it. The interpretation of either the LIF or absorption signal under highly stratified conditions must take into consideration that neither measurement location may coincide with the location of the spark plasma channel. However, overall timing and fluctuation information can be obtained from both types of signals.

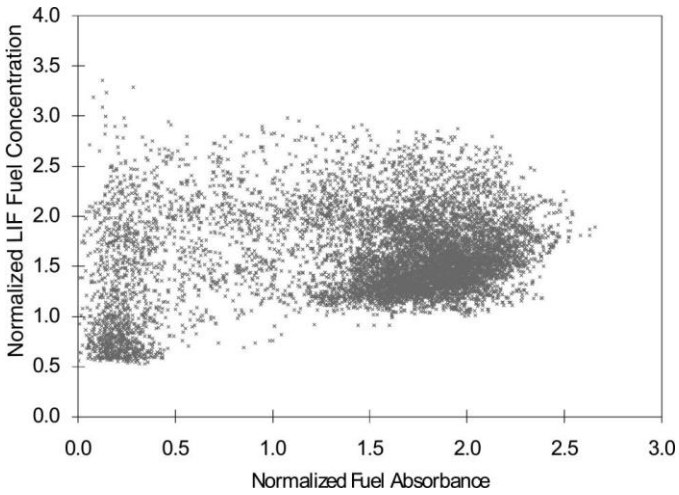

Figure 32: Simultaneously acquired PLIF and absorption data points that were used to generate the average values and standard deviation bars in Figure 31 are presented. The correlation is much weaker for stratified engine operation than for homogeneous mixing conditions (see Figure 26 for comparison). The large spatial and temporal fuel gradients in fuel concentrations are manifested in this plot.

3.3.3 Homogeneous Charge Fired Experiments

While the LIF measurement delivers information on the fuel concentration only, the spark plug sensor measures fuel and combustion product gas concentration (aggregate

of H_2O and CO_2) simultaneously. This capability was demonstrated for an early injected engine run with the intake air throttled down to ~35 kPa at 45°C and a lean fuel/air mixture (ϕ ~ 0:8). The intake air was throttled to achieve near stoichiometric conditions since the quartz cylinder is unable to withstand running at full load (atmospheric intake conditions and ϕ ~ 1). The spark was triggered at 30°BTDC. This spark timing is somewhat early for optimized combustion conditions of the engine when running at 600 rpm and thus higher than usual levels of unburned fuel were expected. The plasma luminosity is clearly visible from 29 − 22°BTDC in the LIF images shown in Figure 33. The flame kernel likely begins in between the light sheet and the camera (see Figure 25 for an illustration of the light sheet location) and eventually burns fuel within the light sheet beginning at 22° BTDC.

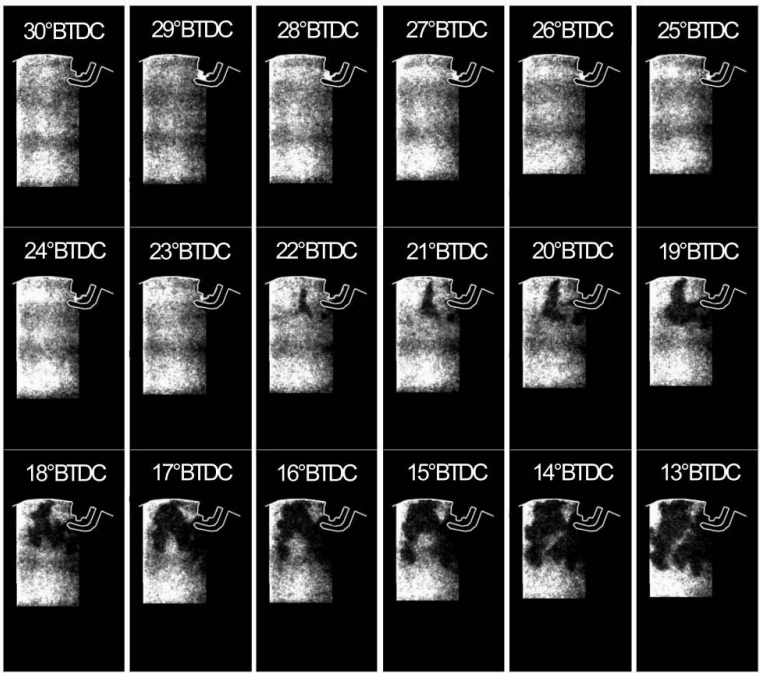

Figure 33: Single-cycle PLIF image sequence from a homogeneous charge part load combustion experiment. Note that the luminosity of the spark plasma is visible from 29 − 22°BTDC. The biacetyl is consumed in the flame showing the corrugated growth of the flame front starting at 22°BTDC.

Figure 34 shows the evolution of the LIF and absorbance signals that were recorded for the single cycle shown in Figure 33. The fuel absorbance rises from 60 − 15°BTDC due to compression, as was observed in the motored measurements shown in Figure 26. The LIF data for this randomly selected cycle show considerable scatter at the measurement location to the left of the spark plug. Fuel is not consumed at the measurement locations until ~17° BTDC, where each signal begins to drop and combustion product gas absorbance rises. The delay between the onset of the spark and the appearance of the flame in the measurement locations is likely due to the time required for energy transfer to the fuel and for the time for the flame kernel to develop. The LIF signal drops off more quickly than the fuel absorbance signal because the LIF measurement location is closer to the spark gap where the flame must have started. Note that the combustion product absorbance data clearly indicate the presence of residual gas in the cylinder from the previous cycle. Although no correction has been applied to determine the magnitude of these data, it is above the noise floor of the measurements and can be concluded to be residual gas. The absorbance signal of the (residual) product gasses also increases during compression along with the fuel signal because of increasing number density. Once combustion starts the signal actually first drops due to expansion of the (hot) combustion gas, and then signals increase again due to continued compression and combustion.

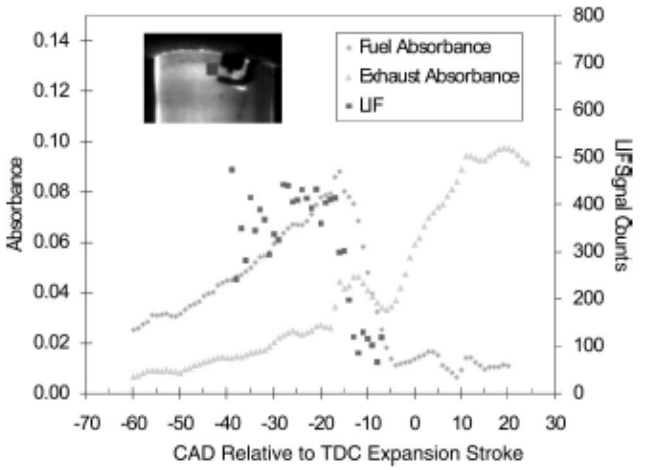

Figure 34: Single-cycle PLIF, fuel, and combustion product absorbance measurements from the homogeneous charge part load fired experiment. The PLIF data were extracted from the images shown in Figure 33. Note that the location of the PLIF data analysis window has been moved to avoid capturing spark luminosity.

Figure 35 shows full cycle profiles of the results of fuel and product gas absorbance measurements averaged over 200 cycles. Both traces start out at residual gas levels and then drop considerably as they are diluted with fresh, dry intake air. Fuel was injected at 250°BTDC and began to arrive at the spark plug sensor around 200°BTDC. As mentioned before, the spark was triggered at 30° BTDC. Similarly to what was observed in the single cycle shown in Figure 34, on average the flame does not reach the measurement area until several CADs after the spark is triggered. The product gas absorbance trace shows a small hump near 15°BTDC. This reflects the expansion of the gases due to combustion as discussed for the individual cycle above. The fuel trace also shows evidence of outgassing as fuel forced into crevices during compression is released during the expansion stroke without immediately oxidizing completely. This fuel eventually reached the probe around 30°ATDC. After the exhaust valves open at

139°ATDC fuel and exhaust signals began to rise and peak approximately 28CADs later. The cylinder pressure when the exhaust valves opened was ~65 kPa, while the pressure in the exhaust manifold during the exhaust stroke was ~96 kPa, so this peak is attributed to residual fuel and exhaust gases from the previous cycle flowing back into the cylinder. The background (light off) signal from the spark plug probe was flat in this region, indicating actual gas dynamics and not some spurious input.

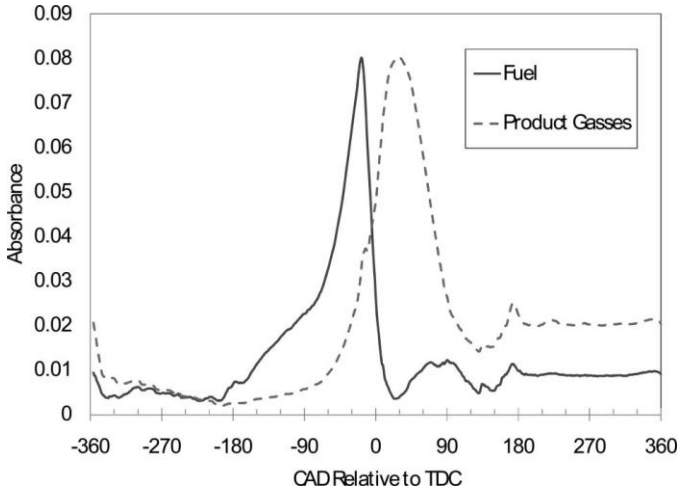

Figure 35: Fuel and combustion product gas absorbance signals averaged over 200 consecutive engine cycles. The traces show important engine operation characteristics such as ignition, outgassing, gas dynamics, and residual gas levels.

3.3.4 Signal to Noise Ratio

Smith et al. reported a signal-to-noise (S:N) ratio of 5:1 for his high-speed biacetyl fuel LIF diagnostics (Smith J. D., 2006). This was done by analyzing early injection, quasi-homogenous charge images. Any variation in signal from cycle to cycle

was considered to be noise. Variations in the amount of fuel injected, mixture heterogeneities, and variations in pulse energy are inclusive in this metric. The average of 100 images was calculated, and the average within a data analysis window was taken to be the signal. For the noise estimate, the spatial RMS within the window was calculated for each of the images, and the average of each realization was calculated.

In the current work, the same approach was used to determine the S:N ratio. These results, along with those of Smith and Sick's are shown in Figure 36. It is clear that the addition of a second laser to increase pulse energy is beneficial. The pulse energy was increased by approximately a factor of 2 (compared to Smiths measurements), which increases the fluorescence signal by the same amount (see equation 10). The S:N ratio can therefore be expected to rise by a factor of the square root of 2 (1.41) due to a reduction in shot noise. Multiplying Smiths S:N ratio by this factor results in an expected S:N ratio of approximately 7:1. Other factors that could potentially account for the additional 13.3% difference between this expected S:N ratio and the measured increase include different levels of mixture homogeneity (injection timing, intake pressure), better pulse-to-pulse stability of the (cumulative) laser pulse energy, or a reduction in read noise from the use of an updated camera.

The diagnostics may now be considered for use in an industrial laboratory. These results must be interpreted in the context of the measurements in section 3.3.1. Absorption measurements have shown that the RMS is approximately 7% of the average over the CAD range displayed in Figure 36. The measurement precision of this

diagnostic is within 1%, so the actual S:N ratio of the diagnostics is even higher than 8:1. Analysis of the early injected quasi-homogeneous charge images did appear to show mixing. This prompted a study to investigate mixing for different early injection timings with the spark plug absorption probe, but problems with the experimental setup and the limited time frame for experimentation prevented the achievement of results.

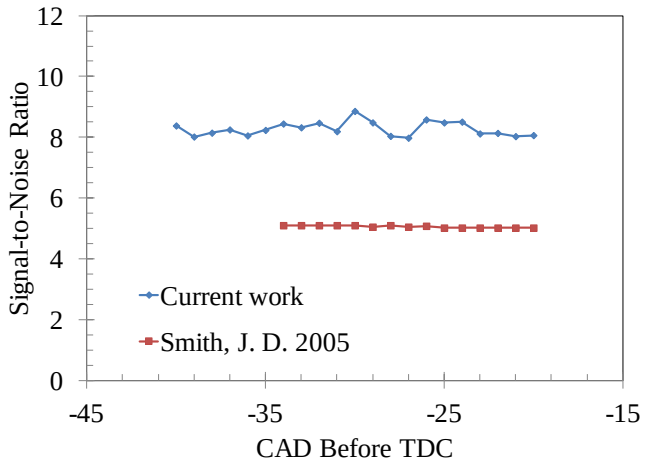

Figure 36: Signal-to-noise ratio comparisons of the current work and Smith and Sick's work.

3.5 Conclusions

This work describes simultaneous high-speed in-cylinder measurements of fuel concentration distributions using PLIF and fuel and exhaust gas concentrations using a mid-IR absorption probe that was integrated into a spark plug. PLIF measurements were based on biacetyl fluorescence that was induced by two simultaneously fired diode-pumped frequency-tripled Nd:YAG lasers. The broadband but spectrally filtered mid-IR

measurements used the fundamental C─H stretch absorption band of hydrocarbons to detect fuel near 3:4 μm, and combined absorption by water and carbon dioxide near 2:7 μm was used as a measure for combustion product gases. Each has desirable measurement characteristics, and when used together they can engender confidence in measurements when they are used alone in different settings.

The combination of both techniques allowed a mutual assessment of the precision and accuracy of the measurements and the applicability of a path integrating absorption measurement at a location slightly offset to the spark plug when information about mixing at the spark plug is desired under highly stratified conditions.

The precision of the PLIF measurements has been improved over previous work due to spatial averaging over 132 pixels and the use of higher laser pulse energies. Precision values as low as 4% are shown for a measurement with highest homogeneity during the exhaust stroke. However, the absorption measurements with a precision of better than 1% also show 4–6% fluctuations in the fuel signal, indicating that this is a true fluctuation for the given operating conditions.

The analysis of the correlation of fuel absorbance and PLIF signal intensity revealed that the assumption of a temperature and pressure independence of the mid-IR fuel absorption coefficient was reasonable around TDC for the iso-octane/biacetyl mixture. A systematic time delay between PLIF data taken from a ~1 mm^2 area near the spark plug and the fuel absorbance measurement for highly stratified engine operation

was linked quantitatively to the fuel motion across the cylinder. No correlation between the PLIF and absorbance values was present in this experiment due to this time delay and large spatial gradients in the fuel concentration. However, it is evident that the absorption probe can be used by itself to identify the arrival of a fuel cloud in the measurement path. Magnitudes of measured normalized fuel concentrations are matched for PLIF and absorption, thus the temporally resolved absorption data can be used for parametric studies of near-spark plug events.

The simultaneous recording of fuel PLIF and fuel and combustion products (aggregate of CO_2 and H_2O) absorption during homogeneous combustion provided information about combustion onset and propagation as well as in-cylinder residual gases. Absorbance profiles reflect important engine operation events, such as valve opening and closing, mixing, combustion, and outgassing from crevices.

While the spark plug sensor measurements presented here indicate that the absorption coefficient for fuel (iso-octane/biacetyl) is less sensitive to pressure and temperature than biacetyl LIF, an absolute calibration strategy for absorption measurements requires quantitatively measured absorption coefficients.

An additional detector should be added as a reference channel in a spectral region without absorption by fuel and exhaust gases (around 3 μm). This channel allows for a true I_0 measurement without assuming that at some time during the engine cycle absorption is negligibly small. This will especially be required to measure absolute

exhaust gas recirculation rates. Exhaust gas measurements could also be based on CO_2 absorption (4.3 μm) to facilitate absolute calibration independent of the ratio of CO_2 and H_2O.

Finally, the S:N ratio of the biacetyl measurements was shown to be improved considerably compared to past measurements, largely because of a decrease in shot noise. The technique may now be considered for use in an industrial laboratory. Mixing in quasi-homogeneous environments may be possible.

CHAPTER 4
HIGH-SPEED HYDROXYL RADICAL MEASUREMENTS

This chapter presents a feasibility study on the applicability of a frequency-quadrupled Nd:YLF laser operating without an intra-cavity tuning element to produce LIF signals of OH radicals. A demonstration of the technique is given with images obtained in a propane torch flame (Cundy & Sick, 2009).

4.1 Experimental Setup

The experimental setup, shown in Figure 37, includes a dual cavity, frequency-doubled, diode-pumped Nd:YLF laser (Quantronix Darwin Duo; A). The two beams exiting the laser head are circularly polarized in opposing directions. A zero order achromatic quarter waveplate (Newport; E) was used to produce linearly polarized light, where the polarizations of the two beams are orthogonal to each other. Therefore, only one of the lasers was used for frequency-doubling from green to UV and the second laser was not triggered during the experiments. The green beam, at a power of 24 W was passed through an aperture (B) and focused with a Galilean telescope [plano-convex lens (C), f =+75 mm; plano-concave lens (D), f =−25 mm] to a beam diameter of ~3 mm. It

was then sent through a KD*P crystal (Quanta-Ray HG-2; F) taken from a pulsed Nd:YAG laser system (Spectra Physics DCR-11). Green and UV beams were separated with a Pellin–Broca prism (G), and the UV beam is passed through a cylindrical lens (*f* =+75 mm; H) and plano-convex focusing lens (*f* =+500 mm; I) to produce a light sheet ~7 mm tall and 0.5 mm wide at the flame location (J).

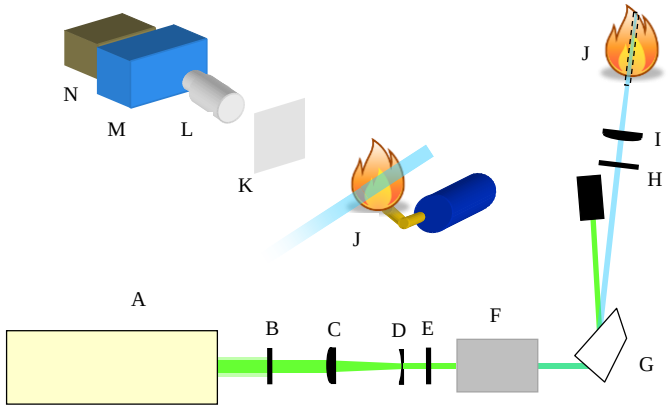

Figure 37: Schematic of the experimental setup. The camera/filter/flame setup is shown as an enlarged insert. Explanations of the symbols can be found in the text.

A propane soldering torch was used as a simple and convenient source of OH radicals in a flame.

The laser was operated at 1 kHz in this work to demonstrate that OH can be excited at 263 nm. Green pulse energies of 24 mJ generated UV pulse energies of 50 μJ. Laser-induced fluorescence emission after excitation within the A–X (2,0) band is expected from 260 to 330 nm with the strongest emissions occurring between 280 and

330 nm (Sick & Wermuth, 2004). OH LIF signals are by far the dominating signals in this wavelength range in a gas flame and simple broadband filtering can be used for detection. A spectral range for the LIF signals was identified by sequentially using color glass filters (Schott WG 280 and WG 365; K) in front of the imaging lens (Coastal Optics; L) on the intensifier (HS-IRO, LaVision; M), which was lens-coupled to a high-speed CMOS camera (Vision Research Phantom 7.3; N). Filtering with a WG 365 filter will block any OH fluorescence and therefore will allow to positively identify OH LIF signal. Furthermore, due to the low pulse energy, high intensifier gains have to be used and the contamination of the LIF images with chemiluminescence is likely. The difference of images taken sequentially with a WG 280 and WG 365 filter placed in front of the intensifier leaves net images of OH LIF signals.

4.2 Results and Discussion

The image sequence shown in Figure 38 demonstrates that selective LIF detection of OH was achieved with a frequency-quadrupled Nd:YLF laser. The left image in Figure 38 shows signals filtered with a Schott WG 280 color glass filter. The image shows two oval areas on the periphery of the jet flame at the location where the light sheet intersects the flame horizontally. Due to the low pulse energy that was available the image intensifier was set to a high gain of 9,000. Thus, despite the short gate time of 400 ns the image contains some chemiluminescence signals at longer wavelengths, such as from CH* and maybe to a lesser extent C_2^* in the core of the flame where the inner premixed flame is located. With the same intensifier settings, a 200-image average of signals was

measured with a Schott WG 365 color glass filter installed. This image is shown in the center of Figure 38. The OH LIF signals are absent but the longer wavelength chemiluminescence signals are still present. The difference of the left and center images in Figure 38 is displayed on the right. It clearly shows the successful isolated detection of OH LIF signals at the expected location in the flame.

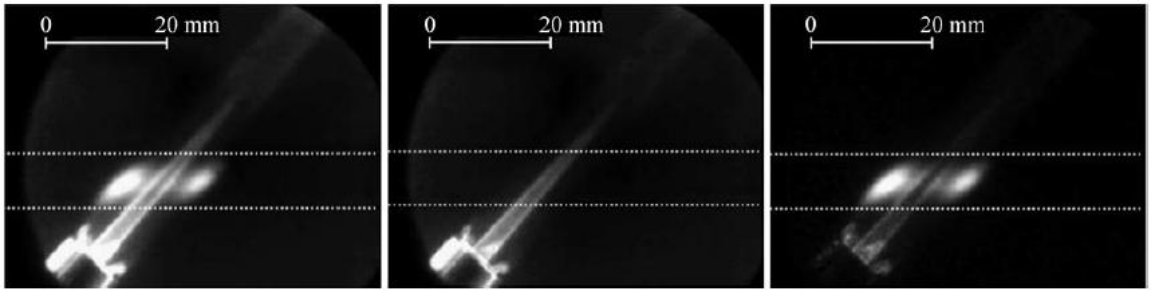

Figure 38: Average of 200 images taken with the WG 280 filter (left) and WG 365 filter (center). The difference of the two images (right) shows largely OH LIF signals to the left and right of the inner core of the flame along with some residual chemiluminescence signal. Note that the intensifier settings were 400 ns gate time and a gain of 9,000 to obtain OH LIF signals with only 50 μJ of broadband light at 263 nm. The extent of the light sheet is marked with the dotted white lines.

The averaged images shown in Figure 38 were obtained using excitation energies of 50 μJ per pulse. This is the same pulse energy that Kittler and Dreizler (Kittler & Dreizler, 2007) reported for their OH LIF work using a high repetition rate dye laser system operating at 283 nm. Based on the Einstein B coefficients for absorption the expected signal ratio between excitation in the (1,0) band at 283 nm and the (2,0) band at 263 nm is about a factor of 6 in favor of the (1,0) excitation (Luque & Crosley, 1999). Increasing the pulse energy of the quadrupled Nd:YLF to just a mere 300 μJ will enable measurements of similar quality as reported with the dye laser system. The pulse energy of the system that was used in this work depends on the repetition rate and is shown in

Figure 39. The pulse energy and the conversion efficiency from 527 to 263 nm decrease with increasing repetition rate. Overall, the conversion efficiency is low for the present system. However, this is not unexpected given that the Nd:YLF emission is spectrally quite broad (∼20 cm−1 at 527 nm) and the pulse duration of the 527 nm light increases from 100 to 400 ns at 1 and 10 kHz, respectively. The intensity of the frequency-doubled light for low conversion rates is given as (Demtröder, 1998):

$$I(2\omega, L) = I^2(\omega)\frac{2\omega^2\left|\chi_{eff}^{(2)}\right|^2 L^2}{n^3 c^3 \in_0}\frac{\sin^2(\Delta kL)}{(\Delta kL)^2} \quad [13]$$

where I is the intensity, ω is the frequency of the fundamental wave, L is the shorter of the coherence length or length of crystal, $\chi_{eff}^{(2)}$ is the effective second-order nonlinear susceptibility tensor, n is the index of refraction of the crystal material, c is the speed of light, ε_0 is the permittivity of free space, and Δk is the difference between the sum of the two ordinary wave vectors and the extraordinary wave vector which is related to the phase difference. The conversion efficiency is therefore expected to increase if the focus and second-order nonlinear susceptibility tensor are increased and if pulse duration and bandwidth are reduced. The former two can be accomplished using different lenses and a BBO or CLBO crystal, and it is estimated that 300 μJ pulses at 1 kHz can be achieved. Clearly, if all options are pursued, much higher pulse energies can be expected and single-shot imaging at high frame rates and high signal-to-noise ratio will be enabled.

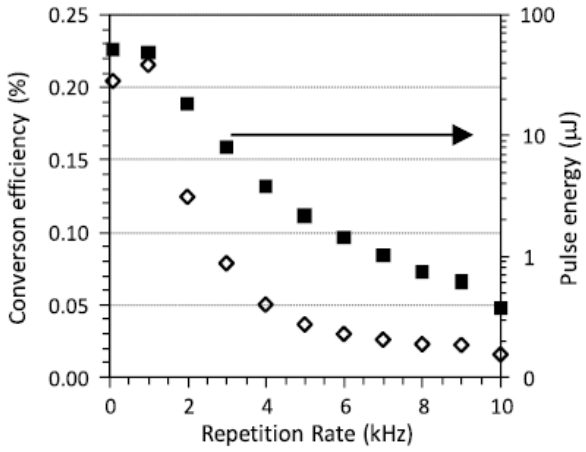

Figure 39: Conversion efficiency (◊) and pulse energy (■) at 263 nm rapidly decrease with increasing repetition rate (and accordingly pulse width).

The origin of the OH LIF signals is due to excitation of several rotational transitions within the A–X (2,0) band. The fundamental spectral bandwidth of a Nd:YLF is around 360 GHz (Malcolm, Curley, & Ferguson, 1990) and thus at the fourth harmonic laser emission can be expected from around 263.1 to 263.4 nm. A LIFBASE (Luque & Crosley, 1999) simulation of an excitation LIF spectrum in this range is shown in Figure 40 for atmospheric pressure conditions at 2,000 K. A clear rotational structure is visible, including transitions from rotational levels ranging from $N'' = 3$ to 20. A more in-depth analysis will have to be performed in the future to determine the exact overlap of the frequency-quadrupled emission of the Nd:YLF laser and the OH spectrum. To this extent, the use of an intra-cavity etalon in the Nd:YLF laser can be useful to tune the laser across the absorption lines. This will help to increase signal and will enable temperature imaging measurements as described below. This analysis will also be needed to determine

temperature dependence of the LIF signals. Details of this and a discussion of collisional effects on OH LIF from v' = 2 can be found in (Sick & Wermuth, 2004).

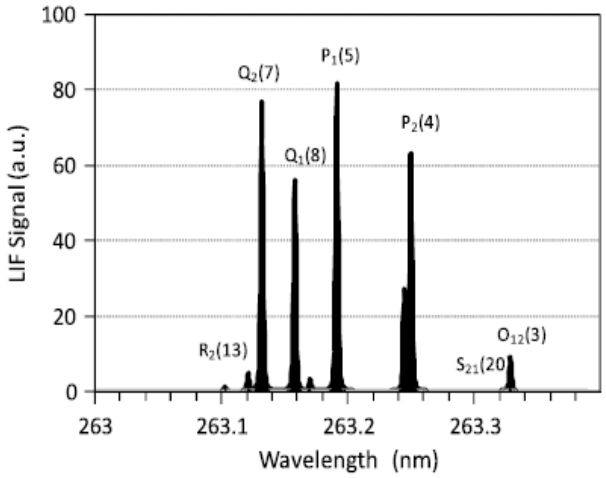

Figure 40: Simulated OH LIF spectrum that lies within the range of the fourth harmonic of the 1,053 nm Nd:YLF emission. The simulation was carried out with LIFBASE v2. For clarity, only selected rotational lines are labeled. The bandwidth of the fourth harmonic is expected to approximately cover the displayed wavelength range.

The overlap of the frequency-quadrupled Nd:YLF laser output with a number of OH rotational lines opens opportunities to devise a convenient tool to measure temperature distributions using LIF of OH radicals. Two-line single-shot OH LIF measurements have been described in the literature (Seitzman & Hanson, 1993) (Meier, Wolff-Gaßmann, & Stricker, 2000) (Arnold, et al., 1992), but all measurements were conducted at a repetition rate of a few Hz. On the other hand, high repetition rate OH LIF measurements were demonstrated but not for temperature measurements (Kittler & Dreizler, 2007). For instantaneous temperature imaging two Nd:YLF/dye laser systems would be required. An alternative approach could be taken using intra-cavity line

narrowing of an Nd:YLF laser, e.g., using an etalon, to enable tunability and specific excitation from a selected rotational level. In a dual-cavity laser system, such as the one used in this study, both resonators could be equipped with etalons allowing independent tuning of each laser. The overlapped frequency-doubled beams are cross-polarized and therefore each can be individually frequency-doubled to 263 nm. The combination of low and high rotational quantum number excitation results in good temperature sensitivity and thus accuracy of the temperature measurement (Seitzman & Hanson, 1993). It has to be pointed out, however, that high-speed CMOS cameras need to be carefully calibrated to ensure that the ratio of two images taken with two separate cameras is not biased by offsets, different nonlinearities, and sensitivities for each pixel. Progress in camera technology can be expected to facilitate this task.

4.3 Conclusions and Outlook

High-speed imaging techniques are becoming increasingly important for investigations of combustion and fluid mechanics mechanics problems. Resolving relevant temporal and spatial scales requires imaging at kHz rates. Camera technology is available to achieve these rates but there are still limitations in laser-based excitation sources, especially when tunability is required for specific excitation of select molecules. High repetition rate dye lasers are available and have been used for example to demonstrate LIF detection of hydroxyl (OH) radicals (Kittler & Dreizler, 2007). In the present work, the use of a frequency-quadrupled Nd:YLF laser, operating at 263 nm, for

selective excitation of OH radicals at kHz rates was demonstrated. OH LIF images were acquired from a flame of a propane torch at 1 kHz frame rate with 50 μJ per pulse. It was shown that a group of rotational OH lines can be excited with an unmodified frequency-quadrupled Nd:YLF laser. The implementation of an intracavity tuning element into the Nd:YLF laser seems advantageous to add tunability and to potentially increase the pulse energy of the frequency-quadrupled light. It is also expected that shorter pulse duration would help to increase the conversion efficiency of fourth-harmonic generation. The prospect of increased selectivity for excitation of individual rotational transitions was discussed and the potential for single-shot high-speed temperature imaging using a dual-cavity laser was presented.

CHAPTER 5
TWO COLOR TOLUENE TEMPERATURE PROOF OF PRINCIPLE AND CALIBRATION MEASUREMENTS

This chapter presents a feasibility study on the use of the two color toluene temperature measurements with excitation at 266 nm near surfaces.

5.1 Optical System Design and Modeling

Since the ratio between the red channel and blue channel is the desired quantity, absolute fluorescence signal values are not necessary and the normalized data in Figure 18 can be used to model the diagnostics. A thorough search was done to identify suitable filters and spectral data was obtained from the manufacturers, where available. The transmission curves of different filter combinations were applied to the normalized fluorescence data and the sensitivity was calculated to compare against one another, and the optimal configuration was selected. Designs were sought for both single camera and two camera approaches.

A two camera approach was utilized for the experiments described in this chapter. Since absolute signal levels could only be estimated, the use of two cameras with two

different intensifiers was desirable because the intensifier gains could be independently adjusted if necessary. A schematic of the approach can be seen in Figure 41.

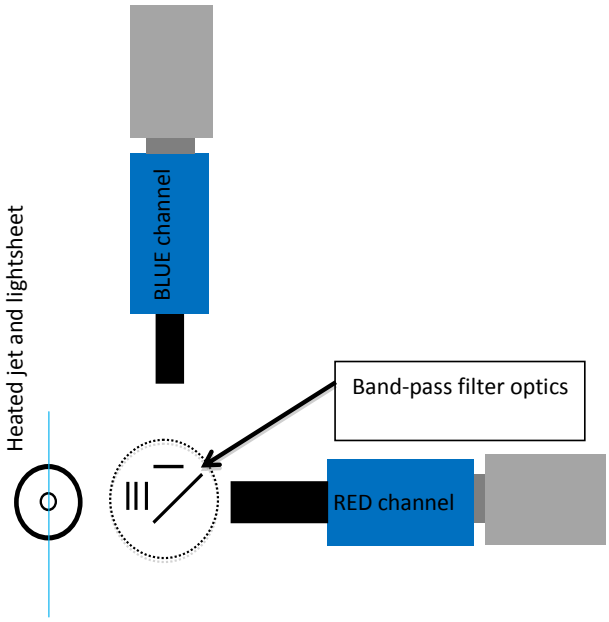

Figure 41: Schematic top view of the experimental setup. Two independent CMOS cameras and image intensifiers were used to record toluene LIF signals from a heated jet in two wavelength regions.

Scattered laser light and spurious light from other sources must be suppressed in each channel. As mentioned before, this thermometry approach has been demonstrated before using 248 nm excitation (Luong, Zhang, Schulz, & Sick, 2008). The benefit of using 248 nm is that the fluorescence is further away from the excitation wavelength and more options are available to suppress scattered laser light without compromising signal level. Fortunately, 275 nm long pass (edge pass; Asahi Spectra ZUL0275) filters were located to suppress scattered laser light in the current work without sacrificing a

significant amount of signal. Since laser light scatter can be orders of magnitude more intense than fluorescence, two of these were selected, allowing approximately 0.003% of scattered laser light (and Rayleigh scattering) to transmit. The performance of these filters is critical to the feasibility of the diagnostics given that they will be used near surfaces. In order to suppress spurious light at longer wavelengths, a 350 nm short pass filter was utilized (edge pass; Asahi Spectra ZUS0300). These three filters were used prior to the image splitter, at which point both channels are filtered. Ambient light is also suppressed by using short gate times, on the order of 400 ns.

A Semrock 310 nm BrightLine dichroic beamsplitter was found to be an excellent image splitter for the two camera approach. The longer wavelengths (red channel) transmitted through the beamsplitter, and the shorter wavelengths (blue channel) reflected the signal. The overall channel transmission for this setup can be seen in Figure 42. The blue channel transmission estimated from manufacturer's data and measured in the QLDL were nearly the same. The red channel reflection is based on manufacturer's data. The shape of the transmission spectrum closely matched measurements in the QLDL, but the magnitude of the transmission was not reliable when measuring after a 90 degree bend due to incident light angle on the beamsplitter and at the collimater entrance.

Lastly, a 300 nm short pass filter (edge pass; Asahi Spectra) was added to the blue channel to reduce the overlap of the channels, which increases the sensitivity.

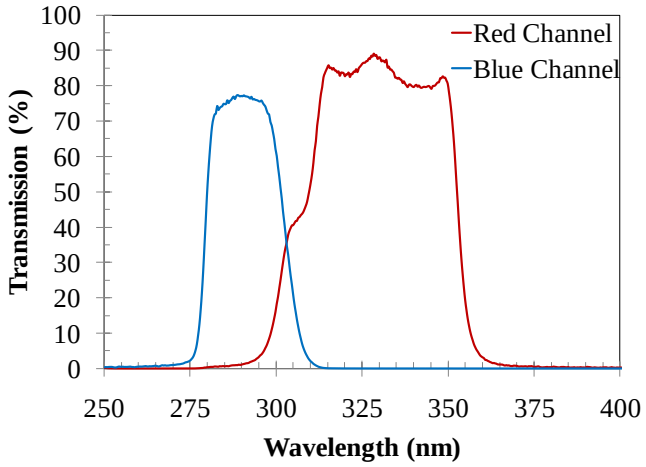

Figure 42: Overall channel transmission in the chosen two camera setup, including two 275 nm long pass filters, one 350 nm short pass filter, a dichroic beamsplitter, and one 300 nm short pass filter to increase the sensitivity of the diagnostics.

A sample of the fluorescence spectrum at two different temperatures and the filtered signals can be found in Figure 43. A visual inspection shows that the red channel grows larger, relative to the blue channel. The red/blue channel ratio as a function of temperature can be found in Figure 44. It is evident that the function is single valued (i.e. any ratio corresponds to only one temperature in the temperature region analyzed) for the temperature range investigated.

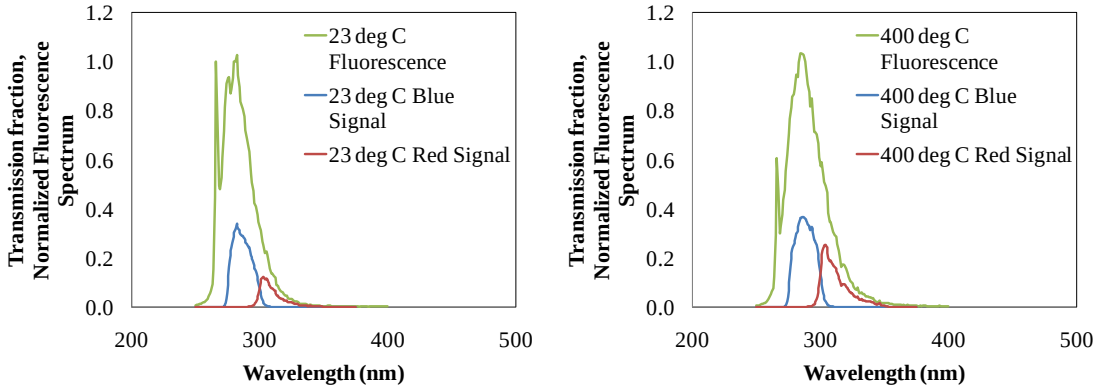

Figure 43: Normalized fluorescence spectrums at 23°C (left) and 400°C (right) from Koban are shown along with the fraction of the signal that is transmitted through the blue and red channels. The transmitted light was integrated and the ratio was calculated to determine the sensitivity of the diagnostics.

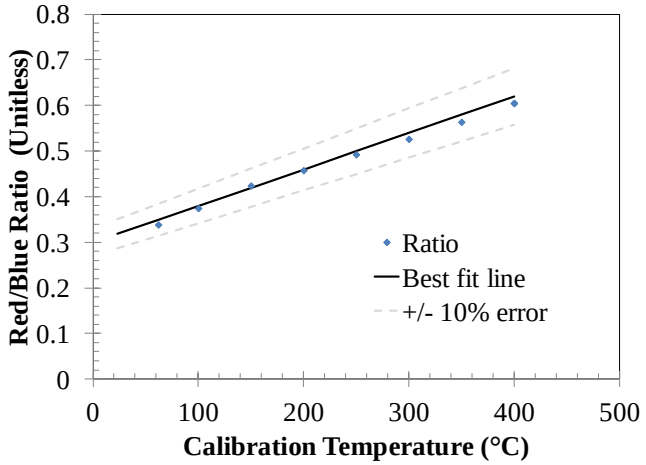

Figure 44: A plot showing the sensitivity of the diagnostics with a best fit line, and lines showing ±10% error.

It is evident that the sensitivity of the diagnostics is low. Estimating 10% noise level, which is conservative, the error is on the order of 50-75°C. Proposed filter arrangements from Koch with 266 nm excitation show much higher sensitivities, with almost a factor of 3.5 difference between the 23°C and 400°C data points (Koch J. ,

2005). However, these filters are not practical to use in cases where signal level is an issue. Such cases involve high speed measurements, where pulse energies are low, high spatial resolution measurements, and cases where the last sheet impinges on a surface and may cause ablation.

5.2 Experimental Setup

Experiments were set up to perform calibration experiments at the base of a shrouded jet of heated nitrogen that was seeded with toluene, and then high-speed temperature imaging was demonstrated for the jet impinging on a cooled curved metal plate.

Experiments were performed in a jet (Re ≈ 2,400) of nitrogen seeded with 2.75% toluene by volume. The toluene was added by bubbling dry, high-purity nitrogen through liquid toluene that was kept in a temperature-stabilized reservoir (T= 23°C). The mixture was introduced via a hose (length = 2 m) into a straight pipe (length = 37.5 cm, 18.8 mm inside dia.) where an electric in-line heater (Osram Sylvania 3500) was placed to heat the gases to up to 600°C. The temperature was measured with a K-type thermocouple (1 mm sheath diameter) in the center of the jet, 3 mm above the nozzle exit. A tapered nozzle reduced flow disturbances between the emerging jet and the surrounding unseeded nitrogen coflow (28 cm dia.). Positive pressure was used to drive the nitrogen and toluene flow at 6000 L/hour through the tubing, heater, and jet, so leaks would result in nitrogen

and toluene leaving the system as opposed to oxygen (and nitrogen) entering the system. After manually adjusting the heater setting and waiting until the jet temperature stabilized at the desired set point, ±1°C, the thermocouple was removed, 5,000 images were captured, and the thermocouple was reinserted to verify that the temperature had not changed. Since the thermocouple diameter is sufficiently small (0.18 mm), conduction errors are small and negligible. Between 30-60 seconds passed between thermocouple measurements.

The schematic of the experimental setup was shown in the previous section (Figure 41). A frequency quadrupled, diode-pumped Nd:YAG laser (Edgewave CX16II-E 80 W) was operated at 10 kHz, producing approximately 0.3 mJ/pulse. Four turning mirrors were used to remove frequency-doubled light from the beam and to direct the frequency-quadrupled light towards the gas jet. A Galilean telescope (f = -50 mm and f = +400 mm) was used to form a light sheet, and an additional f = +1000 mm cylindrical lens was used to compress the sheet thickness to ~0.5 mm. The sheet was passed vertically through the center of the seeded nitrogen jet.

The overall fluorescence signal passed through the filters described in the previous section to create red and blue channels. The red channel signal was imaged with a UV lens (Halle, f = 150 mm, $f_{\#}$ = 2.5), and a high-speed two-stage intensifier (LaVision IRO-HS) lens coupled to a CMOS camera (LaVision HSS 6). The blue channel was imaged with a slightly different UV lens (Halle, f = 100 mm; $f_{\#}$ = 2.0), and the same make and model intensifier and camera as with the red channel.

The fluorescence images were processed with DaVis 7.2 (LaVision). Four processing steps were required before the ratio of the fluorescence images could be calculated and calibrated to temperatures. First, average dark images (from 200 images) were acquired prior to each measurement sequence by capping the lenses in front of the image intensifiers. These were subtracted from each fluorescence image after the recording. Second, average (from 200 images) white sheet correction images were acquired when illuminating each lens directly with a light panel (Kaiser Slimlite). Those images were used to normalize the fluorescence images to account for spatial inhomogeneity across the field of view. Third, spatial calibration images were taken using an UV lamp (Osram), to illuminate a target grid of holes from the backside relative to the cameras. The DaVis software calculated and applied a 3^{rd} order polynomial correction function for both images to match the scaling (pixel resolution = 45.8 μm/pixel) and a common location in the two fluorescence images. This is a critical step to ensure best overlap of the two fluorescence images. Fourth, a 3x3 linear smoothing filter was applied to reduce the influence of noise. The final operation was division of the red channel images by the blue channel images. For each jet temperature setting 2,000 ratio images were computed. From those, values of the measured signal ratio were extracted from the core region of the jet to eliminate any contamination of the results from interactions with the colder nitrogen co-flow. The average of these data were then used along with the thermocouple temperatures to determine a calibration curve for the LIF signal ratio-temperature relationship, according to Equation 11.

To demonstrate the feasibility of this LIF temperature imaging approach for measurements in the gas-phase near surfaces, the hot gas jet was impinged onto a slightly curved metal plate (convex shape with a curve radius of 300 mm) that was water-cooled to approximately 30°C. The plate was placed into the jet slightly offset from its center approximately 15 mm above the nozzle exit with the laser sheet touching the surface of the plate. The plane of the laser sheet contained the center of the nozzle and circular plate.

5.3 Results

The fluorescence intensity ratio was determined for jet temperatures ranging from 100°C to 600°C. After processing the fluorescence images according to the procedure described above, data was extracted from a 10x10 pixel window near the nozzle exit; this is the location where the thermocouple measurements were performed before and after LIF measurement runs. This window size was chosen such that the measurement volume is approximately a cube (10 pixels are approximately equal to the laser sheet thickness of 0.5 mm). The spatial average was computed in each of the 2,000 images; the ensemble average and standard deviation of these data are reported in Figure 45. After excitation at 266 nm the toluene LIF signal strength decreases rapidly with increasing temperature, as seen Figure 45. Therefore, the recorded signal levels were maximized at 100°C, the lowest temperature investigated here, by adjusting the intensifier gain settings. This maximized the dynamic range of the diagnostics. At 100°C the signal level for both

channels was approximately 3500 counts (12 bit cameras). The data at 600°C were included only to guide the calibration curve in the 500°C range. At 600°C the signal levels were too low for meaningful single-shot analysis; division by zero occurred in less than 1% of the background corrected, processed images. The signal levels in the processed, weaker (blue) channel were ~32 on average with a standard deviation of ~6 counts at 500°C. These values still provide valuable single-shot imaging data and thus were included in the following discussion.

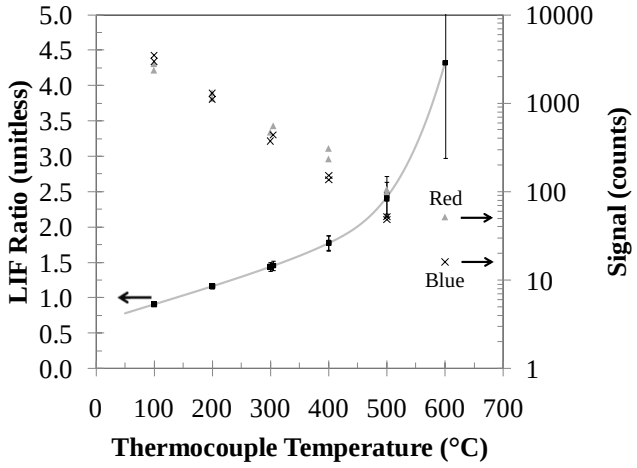

Figure 45: Calibration data obtained from the core of a heated nitrogen jet seeded with 2.75% toluene by volume. Also shown are the average signal counts for the blue and red measurement channel.

Figure 45 shows two data series that were acquired back-to-back during a four hour time period. The duration of the experiment was largely determined by the time needed to change and stabilize the jet temperature. The results indicate the excellent temporal stability of the calibration conditions and the repeatability of the diagnostics. However, as described in the next section, excellent stability of the calibration settings

does not guarantee transferability of a calibration curve to different settings. Two aspects of using high-speed intensifiers should be mentioned in this context (Weber et al. 2011). First, the very high impedance of the multi-channel plate in image intensifiers imposes limits on the rate of recharging the plate after exposure. As a result, the signal obtained from constant light levels might drop over time until an equilibrium value is reached. To avoid bias errors, 5,000 images were recorded for each measurement run to ensure that steady signal levels were reached. The two intensifiers in use had somewhat different depletion time responses and as a precaution to prevent bias errors, only the last 2,000 images of each recording sequence were used in the analysis. The signal intensities were constant within their variance for the duration of recording the last 2,000 images of each recording sequence. Second, the response (output) of image intensifiers may be a complex function of repetition rate, exposure time, incident light intensity, intensifier gain, illuminated area, and the tolerances allowed during the manufacturing process. Therefore, the data and in turn the calibration curve that are obtained with a particular set of intensifiers and their associated settings cannot directly be transferred to other measurement conditions – emphasizing the importance of performing in-situ calibrations with the exact optical setup and settings that will be used in an experiment. A final consideration of the intensifier and CMOS camera combination is the pixel-to-pixel linearity. Weber et al. found that spatial variations, as measured by standard deviations, can be on the order of 4.5-5% of the average value across the pixels considered (Weber et al. 2011). While intensity-based calibration images can be used to correct for these non-linearities, this was not done for the present study.

The calibration relationship that was obtained from the average fluorescence ratios shown in Figure 45 were then used to determine single-shot temperature values for all 2,000 individual ratios per calibration point. From these results, two quantities can be derived. First, the accuracy of the measurements was determined from the thermocouple accuracy (±1°C) and the quality of a fit function through all calibration points, which was better than ±2°C. Second, the measurement precision was derived from the standard deviation of the measured individual temperatures as shown in Figure 46.

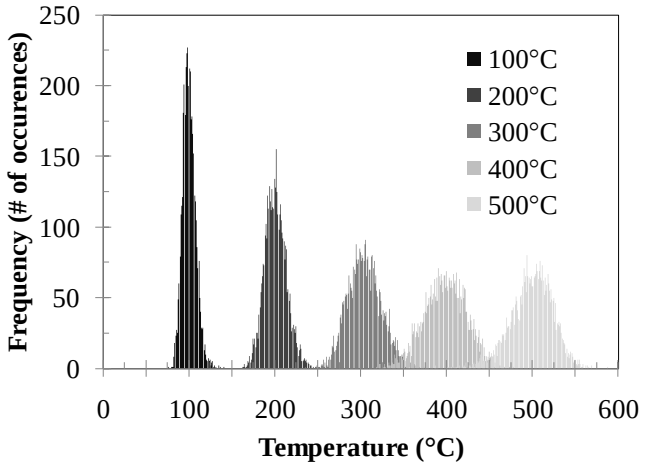

Figure 46: Temperature histograms (4000 data points each; 1°C bin size) show the increase in precision error with increasing temperature. This is the result of an overall reduction in signal strength with increasing temperature and the associated increase in noise.

From the averaged data presented in Figure 45 it would be expected that the sensitivity of the diagnostics increases with increasing temperature and thus the precision error should decrease. However, the results shown in Figure 46 illustrate the opposite in that the precision errors increase strongly with increasing temperature. At 100°C the absolute single shot precision is ±8°C based on one standard deviation, increasing to

±25°C at 500°C. This is a direct result of increased noise in the fluorescence images due to a strong signal decrease in both channels with increasing temperature. One might expect higher noise levels due to the use of the image intensifiers. However, as mentioned before, the 10 x 10 pixel binning reduces error, and the high signal levels allowed lower gain settings (8:1 and 5:1 counts/photo-electron for the blue and red channels, respectively), which reduced the presence of shot noise. Added emphasis should therefore be put on noise-filtering strategies in future work. In this work, filtering was intentionally kept to a minimum to evaluate measurement precision and to preserve gradient information in the boundary layer images.

The red wing of the absorption band of toluene (see Figure 14) extends into the blue fluorescence channel and therefore could give rise to bias errors if the toluene concentration is too high or signal path is too long. The resulting measured temperature would be biased towards higher values since the red/blue ratio would increase. For the conditions studied in this work, the most significant signal attenuation would occur at the highest temperature, because the absorption increases with temperature, and in the center of the circular jet. The absorption is estimated to be less than 2% at 500°C, which translates into a temperature increase of 5°C.

A significant advantage of the single-laser excitation LIF temperature imaging technique is the self-calibration with respect to local laser intensity and toluene concentration. This greatly facilitates the application of this technique to measurements at or near reflecting surfaces and therefore enables time-resolved temperature imaging

measurements in boundary layers. An example of such temperature measurements is shown in Figure 47 where a sequence of seven temperature images, recorded at 10 kHz frame rate, illustrate how a flare of colder gas emerges away from the colder near-surface region of the boundary layer into the hot gas jet. These flares occur with a frequency of approximately 400 Hz, so they would be difficult to observe with low-speed systems. Similar structures have been observed in other boundary layer flow visualization studies and contribute substantially to mass and energy transfer in boundary layers (Pope 2006). The radial asymmetry is believed to be a result of the angle of incidence (AOI) dependence of the image splitter performance. As the AOI of the fluorescence moves away from 45°, the transmission (and reflection) edge shifts to different wavelengths. This causes one band to increase, and the other to decrease. More work should be done to confirm this hypothesis and efforts should be developed to mitigate this issue.

It is also visible how steep the temperature gradients are around the perimeter of the jet as it approaches the plate. The signal-to-noise ratio of the images acquired in this feasibility study is lower than that reported for the temperature calibration curve (Figure 45) because spatial binning was not used here. While the image quality suffers from that, the point to be made here is that the temperature differences between the hot bulk jet flow gas and the cold flares that emerge from the surfaces are large enough to be uniquely identified even with comparably difficult imaging conditions, i. e. CMOS cameras with image intensifiers and low UV-pulse energy of high-speed lasers. The eighth image in Figure 47 is the ensemble average of 200 individual images. It illustrates the steep temperature gradient towards the surface but also shows the loss of the dynamic of the

temperature distribution and spatial details that will be important to understand microscopic heat transfer behavior.

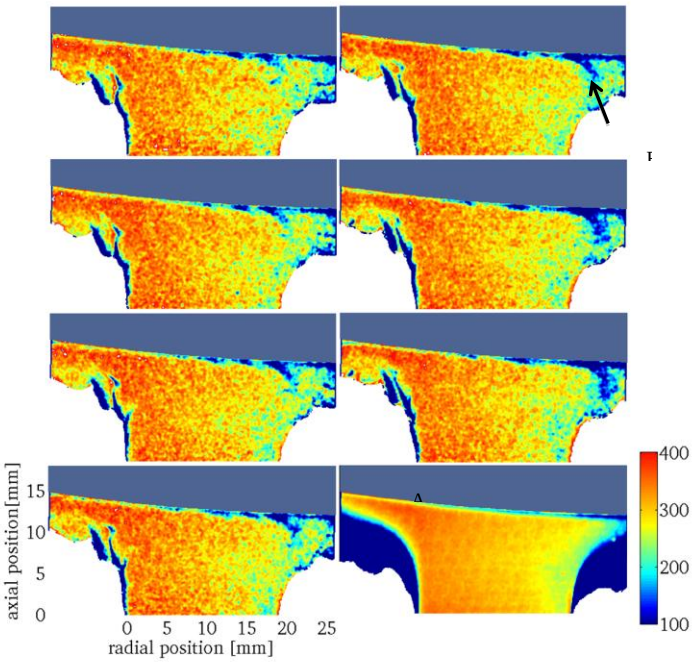

Figure 47: Temporal sequence of the temperature field in a heated jet (300 °C) that impinges on a cooled curved metal plate (30 °C) at 10 kHz frame rate. The motion of flares of colder gas detaching from the boundary layer into the surrounding flow is clearly visible. These spatial details are lost in ensemble averages as shown in the lower right image.

Axisymmetric jets impinging on flat plates with heat and mass transfer have been studied in detail for their applicability to industrial processes. The jet Reynolds number and the ratio of the distance from the nozzle exit to the plate (z) and the diameter (D) are important parameters to consider when characterizing the system. Unfortunately, little work has been done characterizing these systems for the low z/D ratio encountered in this work (~0.70) (Lytle & Webb, 1994). This is probably because undesirable transfer

effects occur between z/D spacings of $0.25 \leq z/D \leq 1.00$ (Behina, Parneix, Shabany, & Durbin, 1999). Also, a study on the effects of turbulence in these systems published in 1965 determined that velocity- and position-dependent boundary layer thicknesses could not be used alone to evaluation heat transfer (Gardon & Akfirat, 1965), which may have contributed to the lack of evaluations of the boundary layer thickness in the literature. Only one theoretical analysis of a laminar slot jet impinging on a flat plate was found providing a 2D hydrodynamic boundary layer thickness analysis (Garg & Jayaraj, 1988), and the results can be seen in Figure 48. The quantity $Re^{0.5} * \delta / L$ (where δ is the hydrodynamic boundary layer thickness, defined as 99% of the free stream value, and L is the slot width) is plotted against a non-dimensional distance from the stagnation point ($X = x/L$, where x is distance from the center of the slot jet). If L is taken to be the jet diameter in the current work, then the velocity boundary layer is expected to grow from nearly zero at the stagnation point (the theoretical analysis was invalid near this singularity) to about 1.92 mm thick at the location directly below the perimeter of the nozzle. Evaluating the averaged image in Figure 47, no stagnation point can be identified, and the thermal boundary layer thickness at $x \approx 19$ mm and $y \approx 12$ mm is estimated to be 0.77 mm. This is based on the difference between the smallest and largest measured temperature in the region. Because of different types of boundary layers compared (velocity vs. thermal) and the significantly different system configurations, it is probably better to compare the current measurements with a simulation of a system that more closely resembles the current one.

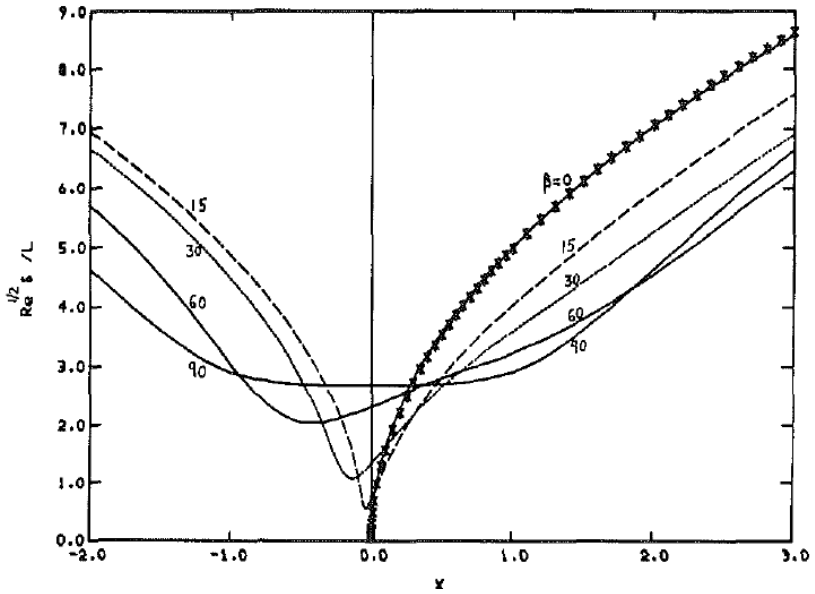

Figure 48: Theoretical boundary layer thickness calculations for a rectangular slot jet impinging on a flat plate from (Garg & Jayaraj, 1988).

5.4 Summary and Conclusions

Single-line excitation of toluene that was seeded into a nitrogen jet was used to demonstrate the feasibility of high-speed gas-phase temperature imaging diagnostics that are suitable for use near surfaces. The temperature-dependent spectral shift of the fluorescence emission allows the detection of fluorescence in two separate spectral regions with different temperature responses simultaneously; the ratio of which is a function of temperature. This function has to be determined experimentally.

A heated nitrogen jet seeded with 2.75% toluene by volume was operated at well-controlled and stable temperature conditions between 100°C and 600°C. Data obtained from these measurements were used to derive a calibration curve for single-shot

temperature imaging measurements and to characterize measurement errors. A frequency-quadrupled diode-pumped Nd:YAG laser was operated at 10 kHz, delivering 0.3 mJ/pulse, to excite toluene at 266 nm. The low pulse energy was the reason for conducting the measurements in nitrogen instead of in an air jet because fluorescence quenching by oxygen reduces the signal levels substantially (see Figure 17). Fluorescence signals were spectrally filtered and separated into two channels that were simultaneously recorded with two high-speed CMOS cameras, each equipped with image intensified relay optics. Even though the sensitivity of the diagnostics indicate that the precision should increase with increasing temperature, overall strong signal decrease and the associated higher noise levels with increasing temperature offsets this and the precision error actually increases. One standard deviation precisions were determined to be ±8°C and ±25°C at 100°C and 500°C, respectively. This assumes the noise is Gaussian.

The calibration data were used to produce single-shot high-speed movies of the temperature field in the heated jet as it impinged near-normal on the surface of a curved, cooled metal plate. This demonstrates the feasibility of using single-line excitation temperature imaging near a solid, reflecting surface and it revealed the unsteady nature of the thermal boundary layer in this flow configuration. In combination with high-speed PIV and particle tracking velocimetry (PTV) in boundary layers (Alharbi and Sick 2010), the temperature imaging diagnostics described here can help to investigate boundary layers and heat transfer properties under unsteady conditions, such as found in IC engines.

CHAPTER 6
APPLICATION OF TEMPERATURE MEASUREMENTS TO AN ENGINE

The two-color toluene thermometry diagnostics outlined in Chapter 2 and discussed in Chapter 5 were applied in a modified form in an optical SIDI engine in the QLDL at the University of Michigan. A single-camera approach was utilized with an image splitter as a necessity, since only one high speed image intensifier was available, but also for two other purposes; less expensive systems make the diagnostics more accessible, and it saves space and potentially allows for an additional camera to be used for simultaneous PIV.

6.1 Engine

The same engine described in section 3.2 is used in these experiments with minor differences. The flat top piston shown in Figure 49 was installed. This changed the clearance volume to 58.77 cm^3, resulting in a compression ratio of 9.5:1. A Phoenix high-speed data acquisition system was installed to allow for online monitoring of engine performance (A&D Technologies; Ann Arbor, MI). In addition to the measurements taken in section 3.2, the intensifier trigger and a photodiode signal are recorded to synchronize images with engine cycles and pulse energies.

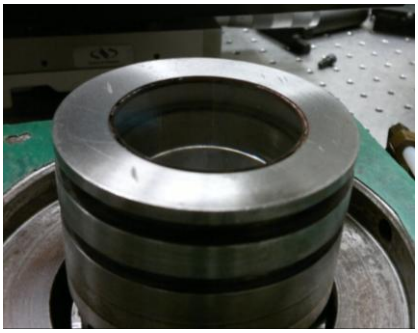

Figure 49: Picture of the flat top piston.

For the experiments presented in this chapter, nitrogen is used in the intake stream to avoid oxygen quenching since this lowers the toluene fluorescence signal substantially. Thus, the engine was run under motored (non-fired) conditions only.

6.2 Optical Diagnostics and Experimental Setup

An overhead schematic of the experimental setup can be seen in Figure 50. A frequency-quadrupled Nd:YAG laser operating at 20 Hz (LaVision, GmbH), producing 266 nm light is used. The light passes through a quartz glass plate with an angle of incidence of 45°, which reflects a small fraction of the light towards a photodiode. The main beam then passes through a Pellin-Broca prism, which separates out residual frequency-doubled light and turns the beam 90°. The beam then passes through an aperture and a +1 m plano-convex cylindrical lens to form a light sheet. The beam then

reflects off of a 266 nm mirror, which directs it to the apex of the pent roof cylinder head near the cylinders axis. For measurements with a larger FOV, the cylindrical lens was replaced by a +0.5 m plano-convex cylindrical lens and two spherical lenses (– 200 mm and +500 mm) to produce a wider and thicker light sheet.

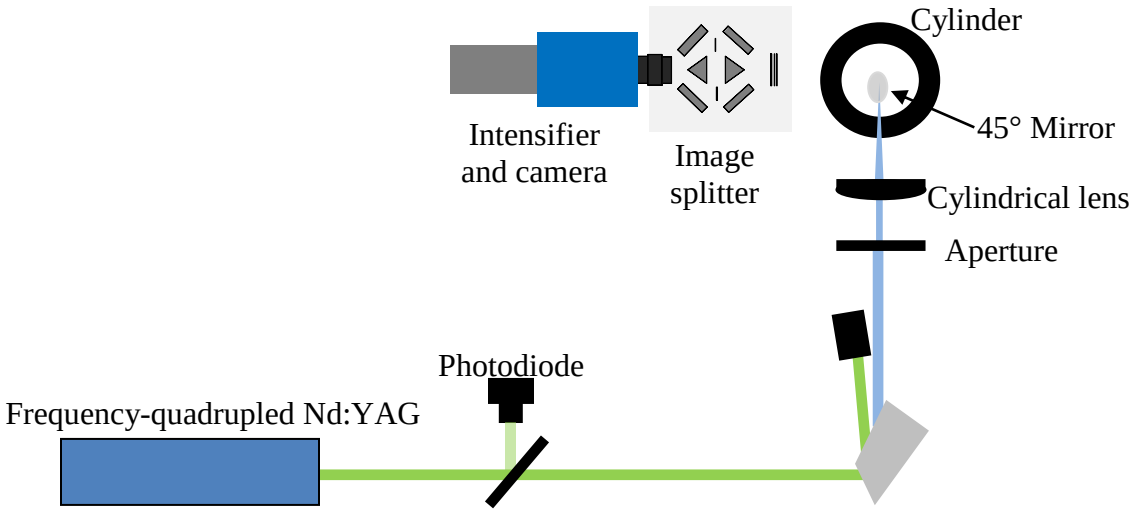

Figure 50: Overhead schematic of the experimental setup.

A schematic of the single camera with image splitter approach can be seen in Figure 51, and a picture can be seen in Figure 52. The design is based on the diffuse nature of the fluorescence. Light emanating from the same region in space will pass through both channels and reach their respective sides of the camera chip. One advantage of this approach compared to other single camera designs is that it enables both channels to have the same path lengths. Translation stages can be utilized under the turning mirror mounts. The depth of fields of each channel must be matched to produce

the best quality images. An iterative approach is taken. Each channel is made to focus on a target. The target can then be moved until one of the channels becomes out of focus, at which point it is refocused. The process is repeated until both channels become out of focus at the same time.

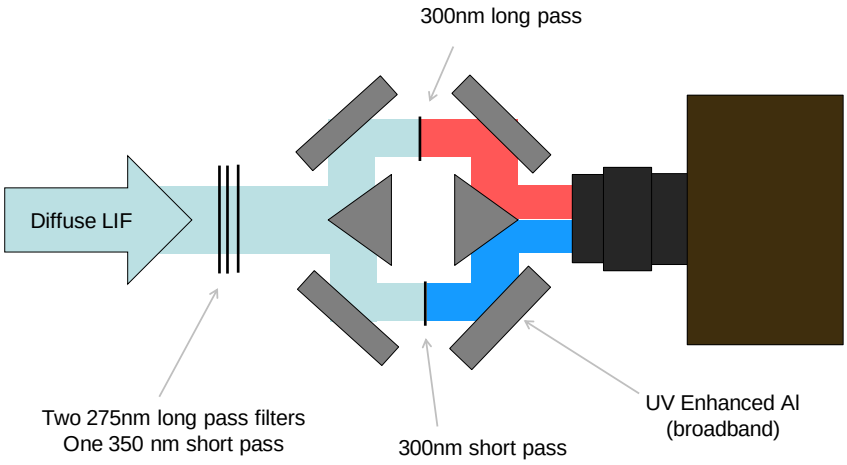

Figure 51: Schematic showing the single camera approach that is utilized in the current work. The path lengths of each leg can be adjusted using translation stages that support the turning mirrors.

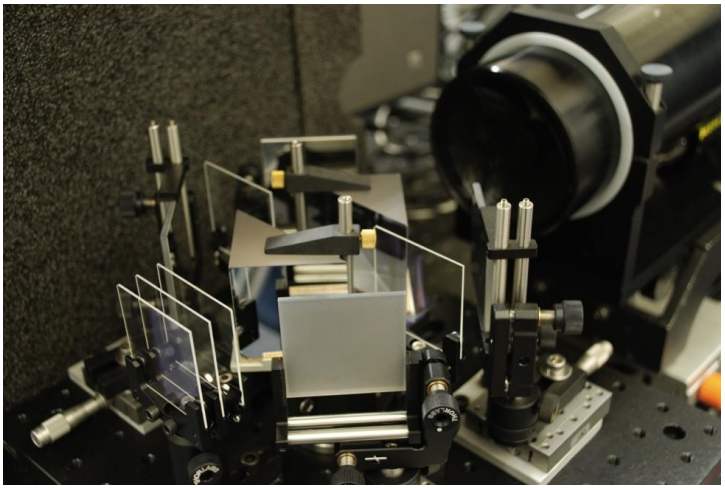

Figure 52: Image of image splitter and long distance microscope.

Similar to the work described in Chapter 5, two 275 nm long pass filters are used in both channels to remove scattered laser light, and one 350 nm short pass filter is used to remove spurious light with longer wavelengths. In the single camera approach taken in the current work, the signal reflects off of four different surfaces before it reaches the camera, so it is imperative that these have high reflectivity. Broadband UV enhanced aluminum coatings with reflection on the order of 88% were applied to the legs of the two prisms. The turning mirrors on the outside (2^{nd} and 3^{rd} reflecting surfaces in each channel) were stock items with a MgF_2 aluminum coating, which reflects approximately 93% of the fluorescence. In one of the channels, a 300 nm short pass filter was inserted to create the blue channel, and in the other channel a 300 nm long pass filter was inserted to create the red channel. The total transmission of the image splitter, including losses due to mirrors, can be seen in Figure 53 along with the toluene LIF spectrum at 300°C.

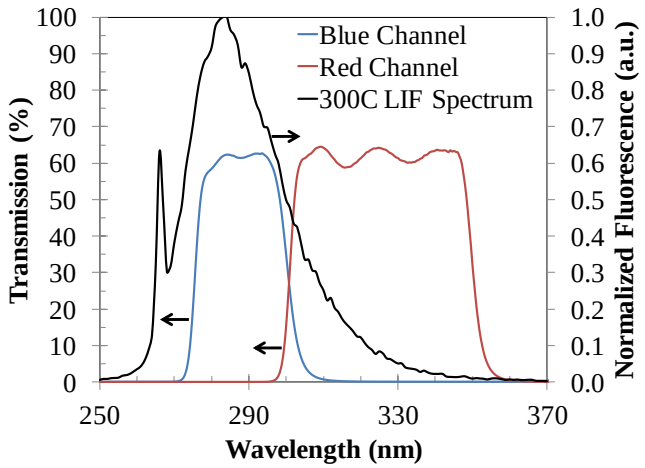

Figure 53: Overall channel transmission in the chosen single camera setup, including two 275 nm long pass filters, one 350 nm short pass filter, one 300 nm short pass filter (blue), one 300 nm long pass filter (red), and reflection losses off of four turning mirrors.

Initial experiments were performed with a long distance (LD) microscope (Questar QM-1) with a Maksutov-Cassegrain Catadioptric configuration with UV optics. The natural divergence of the low speed Nd:YAG combined with a +1 m cylindrical lens resulted in a sheet thickness of approximately 140 µm FWHM at the waist. This was found to ablate material from a spare cylinder head with pulse energies of ~10 mJ (see Figure 54), so the cylindrical lens was pushed closer to the engine to produce a thicker light sheet (~400 µm FWHM) to avoid damaging the engine and piston window. The light sheet fell within a depth of field of approximately 2-3 mm. Additional measurements were taken with an f = 100 mm UV lens and wider and thicker light sheet (~7 mm width and ~1 mm thick) to image a larger FOV.

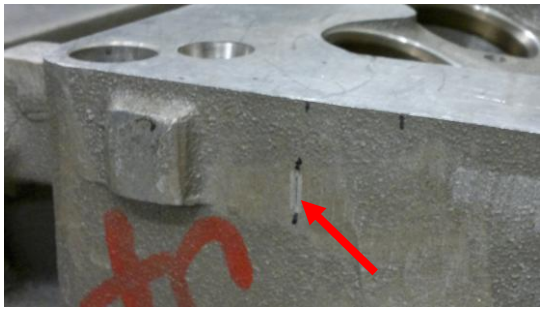

Figure 54: A light sheet of approximately 140 µm FWHM thickness, 6 mm width, at 10 mJ had sufficient energy density to ablate material off of a spare cylinder head.

A stereoscopic effect exists between the channels due to the design. Each channel is viewing the light sheet (or target) from a different angle, so moving the light sheet (or target) towards or away from the image splitter results in the photons impinging on different parts of the camera chip. This is illustrated in the two images Figure 55. The top image was taken with the target at a location 220 µm in front of the bottom image. This distance is on the order of the laser sheet thickness, so the calculation of the lateral spatial resolution would require an accurate determination of the sheet thickness. Profiles of these images were used to determine that the magnification of each channel remained the same. The stereo effect also affects the calibration procedure. A target of dots (60 µm in diameter and spaced 300 µm center to center; manufactured by the Lurie Nanofabrication Facility at the University of Michigan) is imaged and used to dewarp, scale each channel, and identify a common location in each image. However, because the target is placed at a discrete distance within the depth of field, the overlap must be fine tuned. This was done by taking advantage of non-uniformities in the laser sheet profile. One of the images was shifted laterally pixel by pixel until the peaks and depressions of the laser sheet cancelled out in the ratio image. A very small stereo effect

was observed in the vertical direction, and a manual shift of one or two pixels was generally done to better overlap laser reflections off of the cylinder head.

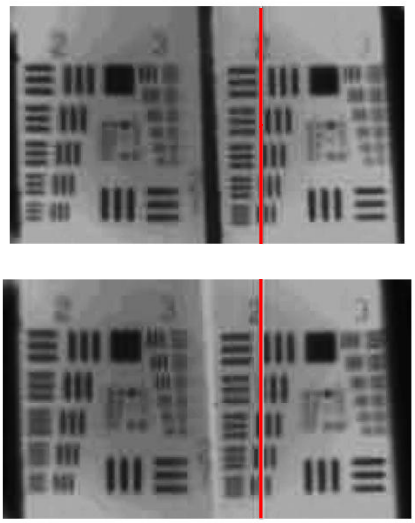

Figure 55: The top image of the Air Force target plate was taken 220 µm closer to the camera lens than the bottom image. As the target is moved further from the camera lens (top image → bottom image), the channels move closer to one another. Red lines indicate the same column of pixels on the camera to help observe the effect.

A white sheet correction was performed as a first processing step using a photography thin panel light box (Gagne; Johnson City, NY). Background images (laser on, no fuel/tracer injection) were captured at each CAD, averaged, and subtracted from the fluorescence images at their respective CADs. A 3rd order polynomial dewarping routine was then applied. The overlap of the images was fine tuned as described above. A 3x3 pixel smoothing filter was used to suppress noise; larger size smoothing and sliding average filters were found to interact with the regions influenced by laser reflections and so they could not be used. Following the smoothing process, the images

were divided, and a calibration was applied to calculate temperature. The center portion of the light sheet where signal levels were highest was used for analysis.

Vignetting can often be a problem when imaging near surfaces. In the present measurements, an attempt was made to acquire images near the apex of the combustion chamber where the curvature of the cylinder head is nearly zero and the light sheet impinges on the cylinder head where a small protrusion exists. Vignetting is therefore thought to be negligible in this work.

6.3 Results and Discussion

The experimental matrix can be seen in Table 7. High spatial resolution measurements are discussed first, followed by lower spatial resolution measurements.

CADs measured	Intake N_2 Temperature (°C)	Lens
44°BTDC, 26°BTDC, and TDC	45	LD Microscope w/ UV optics; f/#=8.7
44°BTDC, 26°BTDC, and TDC	90	LD Microscope w/ UV optics; f/#=8.7
44°BTDC, 26°BTDC	45	f = 100 mm UV; f/#=2.8

Table 7: Overview of the experimental conditions. The oil and coolant temperatures were maintained at 45°C throughout the experiments.

6.3.1 High Spatial Resolution Measurements

Sample averaged high spatial resolution images showing the selection of an appropriate overlap of the images in the case of a uniform temperature field (static engine at room temperature) are shown in Figure 56. Two observations are evident from these images; the center image is the best overlap, and there is an artificial gradient in the image.

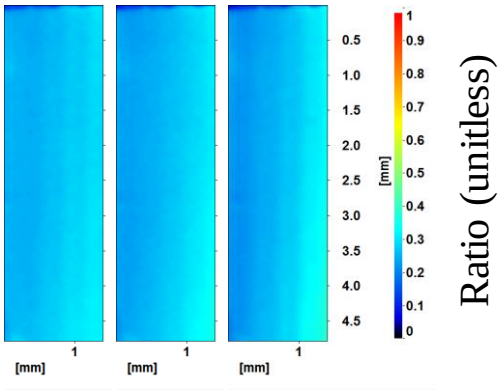

Figure 56: 200 ratio image averages of a static temperature field showing the use of laser sheet peaks and depressions to determine proper overlap. The third image from the left is the best overlap of the four. The images also show an artificial gradient.

There are a number of possible explanations. Evidence of spherical aberrations has been observed during experimentation. Images of a target with dots showed well defined dots in the middle of the image and comet-like shapes towards the circumference of the image. The temporal RMS/temporal AVG of a white image showed values approximately 20% lower towards the edge, which also indicates blurring or smearing. However, there is little evidence that these distortions are present, based on the images in

Figure 56. There could be a problem due to the wavelength dependent focal length of the lens. A test without the 300 nm short pass and 300 nm long pass filter (creating two equal channels) revealed significant differences in the ratio images. Another possible explanation is related to focusing. Neither channel is viewing the light sheet orthogonally, so it is conceivable that one side or edge of the light sheet will be in better focus than the other. The region that is in better focus will result in higher intensities than the region that is not focused as well. The last and most likely explanation could be that the transmission of the dielectric short and long pass filters used to create the red and blue channels is dependent upon the angle of incident light. Transmission measurements were captured as a function of angle of incidence, and the cutoff wavelength was seen to shift by up to 2 nm at angles 5° from the orthogonal direction. This is significant given the width of the channels (e.g. the blue band is expected to be ~25 nm wide). More work should be done to understand this effect. Given the design of the image splitter, it makes sense that this effect would primarily be present in the lateral direction.

Although an artificial gradient is present, it exists only in the lateral direction in the center of the FOV and profiles may still be used quantitatively. The calibration curve, developed in-situ, can be found in Figure 57. The average ratio in the ten pixels furthest away from the wall in the averaged profiles with a 45°C intake stream were assumed to represent the core combustion chamber gas temperature, which was calculated using a polytropic analysis. Since each pixel represented 0.23 µm x 0.23 µm in space, the ten pixels corresponded to the space along a line ~4.25 mm to ~4.50 mm away from the wall. It was found in low spatial resolution images (discussed in section

6.3.2) that this assumption was valid at 26°BTDC, but may have given a value 10% low in the 44°BTDC data. No data was available for comparison at TDC. The polytropic exponent was taken as the slope of the line of the compression stroke on the log-p log-V graph. It is clear that the sensitivity of the calibration curve, particularly at lower temperatures, is lower compared to the measurements presented in Chapter 5. This is a result of the single camera technique; since only one intensifier images both channels, only one gain can be used. In the two-camera approach, the gains can be adjusted separately to improve sensitivity.

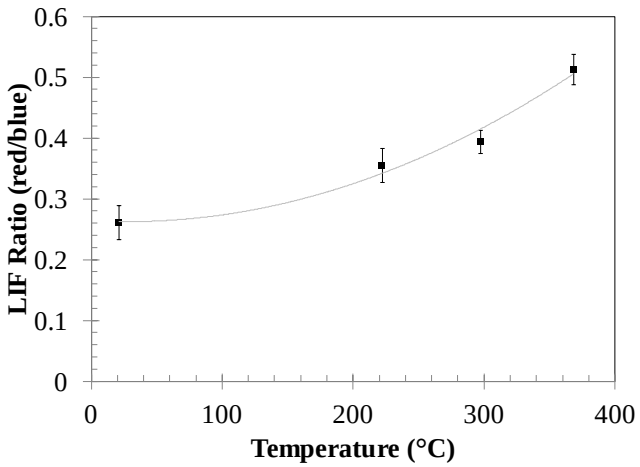

Figure 57: Calibration curve developed in-situ.

An error analysis similar to that presented in Chapter 5 was performed and is shown in Table 8. The imperfect fitment of the calibration curve to the data points introduces an accuracy error, and the ± one standard deviation variation in single shot temperatures was considered to be the precision error. Note that this overestimates the error since the engine temperature is expected to be non-uniform. The total error is then

the root-sum-square of these errors. The use of more data points, made possible with high speed measurements, would allow for an improved curve fit and reduced accuracy errors.

CAD	Accuracy Error (°C)	Precision Error (°C)	Total Error (°C)
44°BTDC	18	20	27
26°BTDC	10	14	17
TDC	13	12	18

Table 8: Error analysis for the high spatial resolution measurements.

As mentioned in Chapter 5, the red wing of the absorption band of toluene (see Figure 14) extends into the blue fluorescence channel and therefore could give rise to bias errors if the toluene concentration is too high or signal path is too long. The most significant signal attenuation would occur at the highest temperature and number density (~675 K at TDC). The absorption is estimated to be 1.5% in this environment. Using the calibration curve shown above, the result is a temperature increase of 2°C.

The boundary layer profiles averaged over 200 cycles at three different CADs and two intake temperatures in each case can be found in Figure 58. Thermal boundary layer thicknesses in textbooks are traditionally defined as 99% of the free stream temperature, although this is an impractical metric for measurements with noise. If the boundary layer thickness is taken to be 90% of the core combustion chamber temperature, the largest measured boundary layer in the current experiments is 0.710 ± 0.046 mm at 26°BTDC with 45°C intake temperature. The next largest is 0.370 ± 0.046 mm at 44°BTDC with

90°C intake temperature. The smallest is within the region that is substantially affected by background reflections and subtraction (less than 0.1 mm; 44°BTDC with 45°C intake temperature). There does not appear to be a trend in boundary layer thickness as the engine cycle progresses in the current measurements.

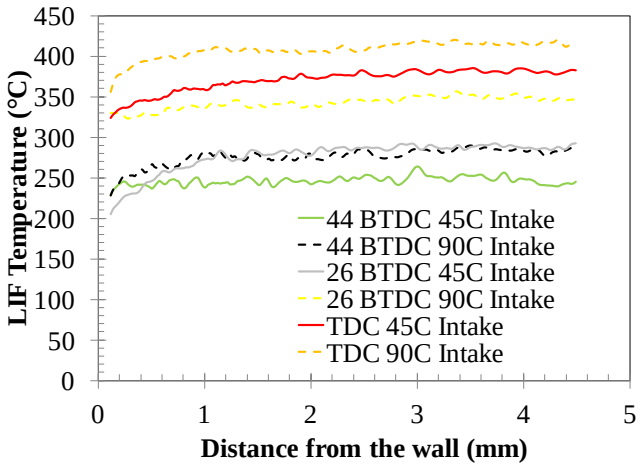

Figure 58: Boundary layer profiles averaged over 200 cycles for six different experimental conditions.

Lyford-Pike & Heywood published thickness measurements on one particular location on the cylinder head of their square cross section engine in Figure 7. The boundary layer edge was considered to be the point in the Schlieren images in which the light completely extinguished (which occurred when the quantity $(1/T^2)*(dT/dy)$ equaled zero). The measurements indicated a thickness of ~0.5 mm at 45°BTDC, growing linearly to ~1.0 mm around TDC (Lyford-Pike & Heywood, 1984). Since the Schlieren technique is sensitive to density gradients, regions beyond the boundary layer thickness

have essentially uniform density. Figure 59 shows boundary layer profiles from Lucht et al.'s CARS measurements (described in more detail in Chapter 1). In order to extract the thicknesses from these plots for comparison with the current work, vertical lines have been superimposed on the plot to identify the core temperature, and the horizontal lines with the same color show the thickness at 90% of the core temperature value. This suggests thicknesses on the order of 0.5 mm to 1.0 mm at TDC depending on the swirl level in the engine.

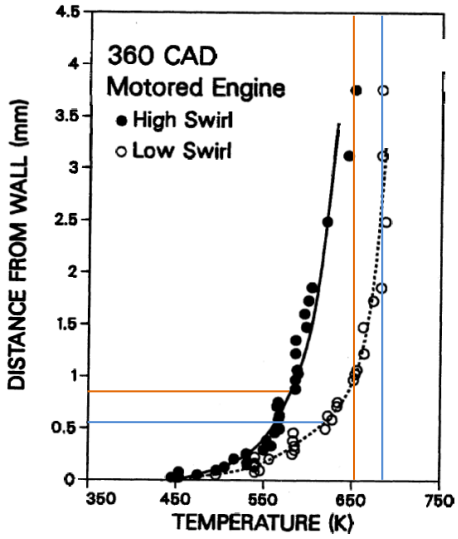

Figure 59: Plot showing how boundary layer thicknesses were extracted from Lucht et al.'s CARS measurements. Vertical lines were selected to indicate the core chamber temperature for each case (blue → low swirl; orange → high swirl), and the corresponding horizontal line is drawn to illustrate the thickness estimate at 90% of the core chamber temperature.

Alharbi used a combination particle tracking velocimetry (PTV) and PIV technique to image the velocity boundary layer at high speeds in the same engine (Alharbi, 2010). Averaged velocity profiles at select CADs are shown in Figure 60. Vertical lines are superimposed onto the plot to give an estimate of the core velocity in

that region, and the corresponding horizontal line identifies the thickness at 90% of the core velocity. At both 30°BTDC (CA 330) and TDC (CA 360), the thicknesses are on the same order as the Lyford-Pike & Heywood and Lucht et al. thickness measurements. Note that velocity is a vector quantity and velocities in the 3rd dimension may indicate thicker velocity boundary layers.

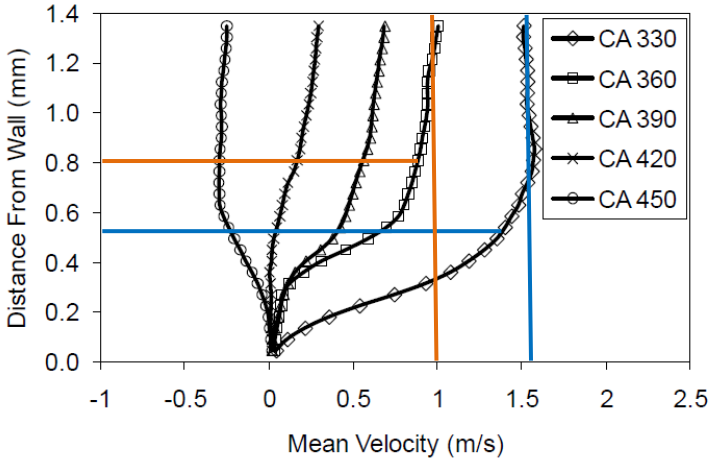

Figure 60: Two dimensional mean velocity boundary layer profiles from Alharbi measured in the same engine.

In the context of previous work, the measured thermal boundary layer thicknesses are of similar magnitude to previously published thermal and velocity boundary layer thicknesses in one case, but smaller in most others. The measurements must be repeated to check for repeatability. If the results of repeated measurements are similar, differences may be attributed to combustion chamber geometry, cylinder head wall temperature, core gas temperature, or flow patterns.

Defining the distance at which the LIF temperature can be confidently measured near the wall is critical. The selection of the cylinder head wall location in the images was taken to be the middle of the reflections in the images. The actual wall location may be a small distance away from this location, so an error of ± 46 μm is assumed (2 pixels) for boundary layer thickness measurements. Ideally, the background subtraction by an averaged background image (pre-dewarping) taken at the same CAD should eliminate the reflections in the LIF images. Then, after each LIF image has been dewarped, the red channel would be divided by the blue channel and the near-zero background levels would either fall to zero or increase to infinity and the locations where wall reflections interferes in the images can be identified. In practice, however, there are complications. The stereo effect described earlier is primarily present in the lateral direction, but a manual shift of one to two pixels is necessary in the vertical direction. Even if this process is successful, engine or optics vibrations cause the location of the cylinder head reflections to move a couple of pixels in some of the images. This results in an imperfect overlap of the background image/LIF image pair, and the subtraction is therefore imperfect. Next, the quality of the overlap of the background subtracted LIF channel images is a function of the effectiveness of the dewarping routine, which will also be imperfect. These effects, when taken together, could give rise to misleading data. Therefore, an alternative method should be used to identify the region where LIF temperatures can be extracted. In Figure 61, the 200 image average ratio profile with both channels background subtracted is shown along with a profile with only the red channel (numerator) background channel subtracted. The influence of the blue channel background is seen to be quite small beyond 0.1 mm from the wall (~6% at 0.1 mm). When the blue channel background is

then subtracted, the true influence of the background on the signal will be far less than this difference. The influence of the background reflections in the red channel is expected to be of less magnitude because of the presence of an additional 300 nm long pass filter, which would suppress scattered laser light at 266 nm. Therefore, beyond 0.1 mm from the wall, imperfections in the overlap (of both background/channel image pairs and channel/channel image pairs) are assumed to have a negligible influence on the ratio. Temperature values (and non-dimensional temperature, T^+, values) within 0.1 mm of the wall ($y^+ = 1.6$) have been omitted from the plots.

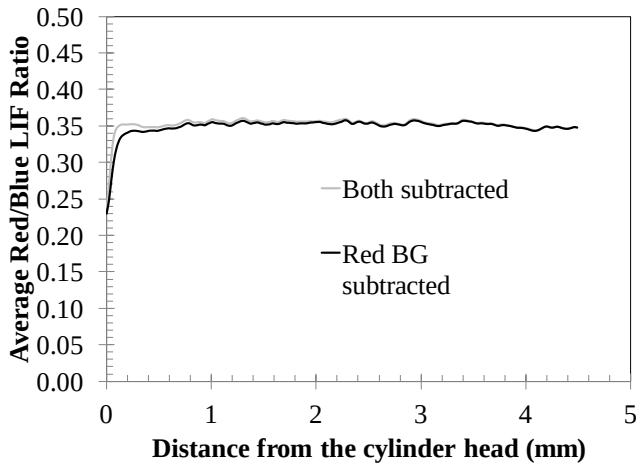

Figure 61: 200 image average boundary layer profiles showing the influence of wall reflections. The influence of blue channel reflections appears to be negligibly small beyond 0.1 mm, and should reduce further with the reflections subtracted. The red channel reflections will have an even smaller influence because of the 300 nm long pass filter.

The temperature profiles can be non-dimensionalized and compared to generalized and ICE thermal boundary layer modeling approaches.

Practical variable density (compressible) flows such as those encountered in the design of aviation vehicles are typically restricted to very high Reynolds numbers, so little work has been done developing the understanding at moderate Reynolds numbers. Therefore, it is only be possible to compare measurements to constant density cases. A generalized turbulent boundary layer with heat transfer development was followed (Schetz, 2010), which is analogous to the velocity logarithmic-law-of-the-wall development. Laminar properties are assumed adequate for the analysis. Utilizing a function to link the inner and outer layers developed by Kader (Kader, 1981), the non-dimensional temperature profile is given in equation 14, using equations 15, 16, and 17.

$$T^+ = \mathrm{Pr}\cdot y^+ \exp\left(-\Gamma\right) + \left[2.12\ln\left(\left(1+y^+\right)\frac{2.5\left(2-y/\delta\right)}{1+4\left(1-\left(y/\delta\right)\right)^2} \right) + C_T\left(\mathrm{Pr}\right) \right] \exp\left(-\frac{1}{\Gamma} \right) \qquad [14]$$

$$\mathrm{Pr} = \frac{c_p \mu}{k} \qquad [15]$$

$$C_T\left(\mathrm{Pr}\right) = \left(3.85\,\mathrm{Pr}^{1/3} - 1.3\right)^2 + 2.12\ln\left(\mathrm{Pr}\right) \qquad [16]$$

$$\Gamma \equiv \frac{0.01\left(y^+\cdot \mathrm{Pr}\right)^4}{1+5y^+\cdot \mathrm{Pr}^3} \qquad [17]$$

where y^+ was defined in equation 8, y is the distance from the wall, and δ is the boundary layer thickness. The boundary layer thickness is often taken as the distance between the

wall and the centerline of a pipe or channel flow in this development. Incropera and Dewitt indicate that it is a reasonable to use the velocity boundary layer thickness equation to estimate the thermal boundary layer thicknesses for turbulent flow over an isothermal flat plate, which is shown in equation 18 (Incropera & Dewitt, 2006).

$$\delta = 0.37 x \, \mathrm{Re}_x^{-1/5} \qquad [18]$$

where x is the distance from the leading edge of the plate, which is taken to be half the cylinder bore. In this development, the non-dimensional temperature T^+ is related to temperature, T, by equation 19.

$$T^+ = \frac{\rho c_p u_T \left(T - T_w\right)}{q_w} \qquad [19]$$

where T_w is the wall temperature, and q_w is the wall heat flux.

The measurements were also compared against the predictions of the five different RANS models described in section 1.2.3.2. The non-dimensional temperature profiles used in these models are summarized in Table 9, along with their validity range and the definition of the non-dimensional temperature. Definitions for S^+ and P^+ can be found in the respective sources.

Author(s)	Temperature Profile	Validity Range	T^+
Launder and Spalding	$T^+ = \Pr y^+$	$y^+ \le 11.63$	$T^+ = \frac{\rho u_T c_p (T_w - T)}{q_w}$
	$T^+ = \Pr_t \left(\frac{1}{0.4187} \ln(9.79 y^+) + P\left(\frac{\Pr}{\Pr_t}\right) \right)$	$y^+ > 11.63$	
Angelberger et al.	$T^+ = \Pr y^+$	$y^+ \le 11.63$	$T^+ = \frac{\rho u_T c_p T}{q_w} \ln\left(\frac{T_w}{T}\right)$
	$T^+ = \Pr_t \left(\frac{1}{0.4187} \ln(9.79 y^+) + P\left(\frac{\Pr}{\Pr_t}\right) \right)$	$y^+ > 11.63$	
Han and Reitz	$T^+ = 2.1 \ln(y^+) + 2.5$	All y+	$T^+ = \frac{\rho u_T c_p T}{q_w} \ln\left(\frac{T_w}{T}\right)$
Huh et al.	$T^+ = \Pr y^+ - 0.5 \Pr S^+ (y^+)^2$	$y^+ \le 13.2$	$T^+ = \frac{\rho u_T c_p (T_w - T)}{q_w}$
	$T^+ = 13.2 \Pr + 2.195 \ln(y^+) - 5.66$ $-S^+(87.12 \Pr + 2.195 y^+ - 28.98)$	$y^+ > 13.2$	$T^+ = \frac{\rho u_T c_p (T_w - T)}{q_w}$
Rakopolous et al.	$T^+ = \frac{1}{0.4767}\left[\ln\left(y^+ + \frac{1}{\Pr 0.4767}\right) - \ln\left(40 + \frac{1}{\Pr 0.4767}\right)\right]$ $+10.2384 + P^+\left(\frac{y^+ - 40 + 117.31\left(0.4767 + \frac{1}{\Pr}\right)}{0.4767 + \frac{1}{\Pr}}\right)$	All y+	$T^+ = \frac{\rho u_T c_p T}{q_w} \ln\left(\frac{T_w}{T}\right)$

Table 9: Non-dimensional temperature profiles from 5 different RANS models.

Since there are two different definitions of T^+ in the table above, the comparisons of the measured temperatures with model predictions were made in the form of two

different plots (i.e. to compare the measured temperatures against the Launder and Spalding model, the appropriate T^+ formula in Table 9 must be used). In order to convert the measured temperatures to non-dimensional temperature, several parameters needed to be estimated. The Woschni global heat transfer correlation, with a scaling factor set to 3.26 (Heywood, 1988), was used to calculate a global convection coefficient. Velocity gradient values at the wall were extracted from combination PTV and PIV measurements taken in the same engine as the current experiments (Lu and Jainski; unpublished), and were used to calculate the friction velocity. Measurements at 400 rpm and 800 rpm were averaged (6359 1/s and 6721 1/s for the cases presented at 44°BTDC and 26°BTDC, respectively). Density was assumed spatially uniform and computed using the ideal gas law (1.38 kg/m^3 and 2.18 kg/m^3 at 44°BTDC and 26°BTDC, respectively; note that the intake stream is throttled). The friction velocity was calculated to be 0.33 at 44°BTDC and 0.28 at 26°BTDC. The mixture specific heat was calculated at the film temperature. Parameters needed to be estimated to calculate T^+ for the models as well. The Prandtl number was calculated over a range of temperatures using N_2 and toluene mixtures for specific heat and viscosity values, and N_2 for thermal conductivity values as a simplification, and was found to vary between 0.74-0.81. Because of the small variation, it was assumed constant throughout the profile at an interpolated value corresponding to the film temperature (equation 20). A value of 0.9 was used for the turbulent Prandtl number (Huh, Chang, & Martin, 1990).

$$T_f = \frac{T_\infty + T_w}{2} \qquad [20]$$

where T_f is the film temperature, and T_∞ is the temperature in the core of the combustion chamber. Density was assumed spatially uniform in this analysis as well. Viscosity and specific heat were evaluated at the film temperature when used outside of the Prandtl number calculation.

The comparisons at 44°BTDC with 45°C intake temperature (green trace in Figure 58) can be seen in Figure 62 and Figure 63, and the comparisons at 26°BTDC with 45°C intake temperature (light grey trace in Figure 58) can be seen in Figure 64 and Figure 65. Note that these profiles were chosen because the former shows the thinnest boundary layer thickness in the current measurements, while the latter shows the largest boundary layer thickness. It is clear the measured LIF temperature shows flatter profiles, which is discussed first. Boundary layer thicknesses are discussed, and the magnitude of the T^+ profiles are then discussed.

As discussed before, previous velocity and thermal boundary layer thickness measurements performed in engines show thicknesses on the order of 0.5 mm (y^+ = 9.7) to 1.0 mm (y^+ = 19.4). Beyond this distance, Lyford-Pike & Heywoods measurements indicate uniform density. If uniform pressure is assumed, then the dT/dy term → 0 in the Schlieren equation in this region and temperature is nearly uniform. All models suggest increasing temperature beyond this region (some to a larger extent than others). In Lucht et al.s measurements (see Figure 59), the temperature profile in the low swirl case at TDC does not flatten out until approximately 1.8 mm (y^+=34.4) from the wall. The models

continue to show a subtle rise in temperature beyond this point. However, in Lucht et al.s high swirl temperature profile in Figure 59, there is a subtle rise in the temperature well beyond ~2.5 mm (y^+ = 47.7). In the current work, the intake configuration produced low swirl, and the resulting flat profiles are consistent with Lucht et al.s flat profile further away from the wall in the low swirl case. Taken together, the model predictions may be more adequate for high swirl cases, and the development of models that are sensitive the engine swirl may be an area of interest. However, given that all three measurement campaigns are in different engines with different operating conditions, this result warrants further experimental investigation.

The shape of the profiles near the wall shows differences and similarities compared to the models. The thickness of the laminar sublayer appears to be overestimated in all but the Han and Reitz and Rakopolous models when compared to both of the presented measured profiles (which again represent the smallest and largest measured average boundary layer). In all measured average profiles in Figure 58, the laminar sublayer appears to reside within the region that is significantly affected by wall reflections ($y < 0.1$ mm; $y^+ < 1.9$). The log region is not evident in the measured thermal boundary layer at 44°BTDC in Figure 62 and Figure 63. In the log region of the measured average thermal boundary layer at 26°BTDC shown in Figure 64 and Figure 65, the shape compares favorably to the Han and Reitz and Rakopolous et al. models.

The magnitude of the T^+ values for both measurements and models should be interpreted with caution. For the experimentally derived T^+ profiles, the parameters and

their respective errors are summarized in Table 10. The total error was estimated to be ± 7.13 for the 44°BTDC, 45°C intake case, using the equation for T^+ shown in equation 18. Measuring the heat flux using a heat flux probe during experiments would reduce the total error and allow a better comparison. This is nearly large enough that all models will reside within the range of uncertainty, so an error analysis for the models is not presented. This error will be a function of the Prandtl number, the turbulent Prandtl number, the friction velocity, the cylinder pressure rise rate, and kinematic viscosity.

The equations for the log layer in Table 9 are not a function of core temperature, and the models do not converge to a single (core) temperature even though they are calculated well beyond the expected boundary layer thickness. The differing magnitudes far from the wall and the continued growth of each T^+ may be a method to characterize the boundary layer thickness. An alternative explanation is that, since temperature continuity must exist between the boundary layer and core regions in the models, implementation of the wall functions may be unique to the specific model. The grid size would also seem to affect the implementation.

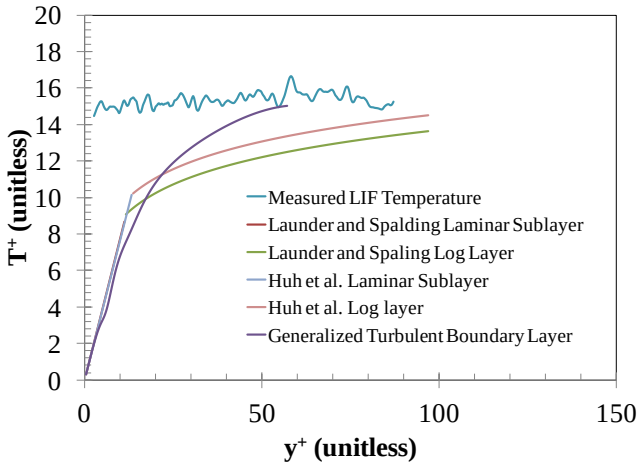

Figure 62: Comparison of LIF temperature measurements at 44°BTDC with 45°C intake temperature with the Launder and Spalding, generalized logarithmic-law-of-the-wall development, and Huh et al. models.

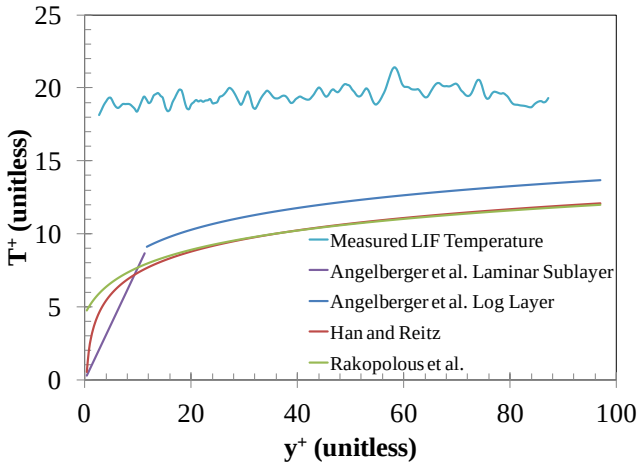

Figure 63: Comparison of LIF temperature measurements at 44°BTDC with 45°C intake temperature with Angelberger et al., Han and Reitz, and Rakopolous et al. models.

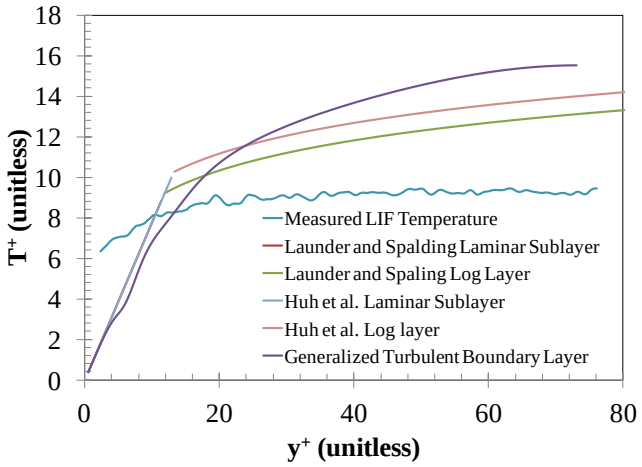

Figure 64: Comparison of LIF temperature measurements at 26°BTDC with 45°C intake temperature with the Launder and Spalding, generalized logarithmic-law-of-the-wall development, and Huh et al. models.

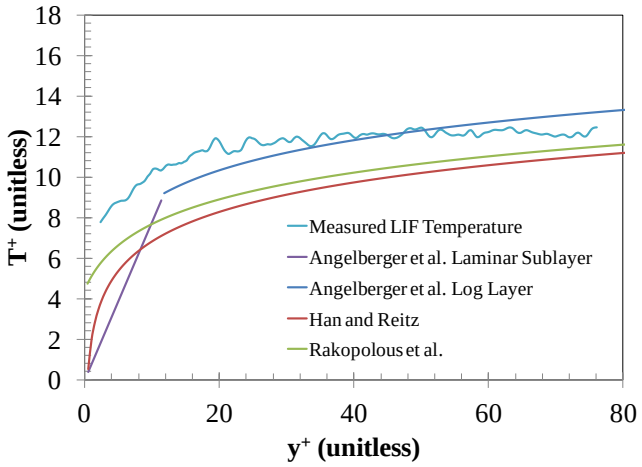

Figure 65: Comparison of LIF temperature measurements at 26°BTDC with 45°C intake temperature with Angelberger et al., Han and Reitz, and Rakopolous et al. models.

Source	Description	Error	Units
Density	Calculated from the ideal gas law. Error is assumed.	1	%
Specific heat	Taken to be the standard deviation of the (calculated) mixture specific heat at 300, 400, 500, 600, and 700 K.	68	J/kgK
Wall heat transfer	Estimated using the Woschni global heat transfer model with a scaling factor of 3.26. No attempt was made to find the appropriate scaling factor for this engine. Error is assumed.	10	%
Wall temperature	The wall temperature was assumed to be equal to the oil/coolant temperature. Error is assumed.	10	°C
Gas temperature	Taken to be the average of the errors in Table 8	21	°C
Friction velocity	This value is assumed. The friction velocity is a function of density, viscosity, and a PTV+PIV measurement technique (2.6% error; Alharbi)	5	%

Table 10: Summary of errors for the experimentally derived T^+ values. For the case presented in Figure 62 and Figure 63 (44°BTDC, 45°C intake data), the total error was calculated to be ± 7.13.

An explanation for the differences and similarities between the measured T^+ profiles and predictions can be aided by evaluation of temperature field images. Since the gradient described earlier is present in ratio images of a uniform temperature field and for measurements in a (non-uniform temperature) motored engine, it is clearly non-physical and must be an artifact of the imaging system. So, normalizing the motored engine ratio images by the static ratio images should eliminate this artifact, and that was found to be the case. The normalization approach is not ideal given the need to manually overlap images (recall the stereoscopic effect), but it allows the images to be evaluated and therefore warrants attention. Sample single shot images at 44°BTDC and 26°BTDC (both at 45°C intake temperature) can be seen in Figure 66 and Figure 67, respectively. The top of the images (z = 0 mm) coincides with the apex of the pent roof cylinder head.

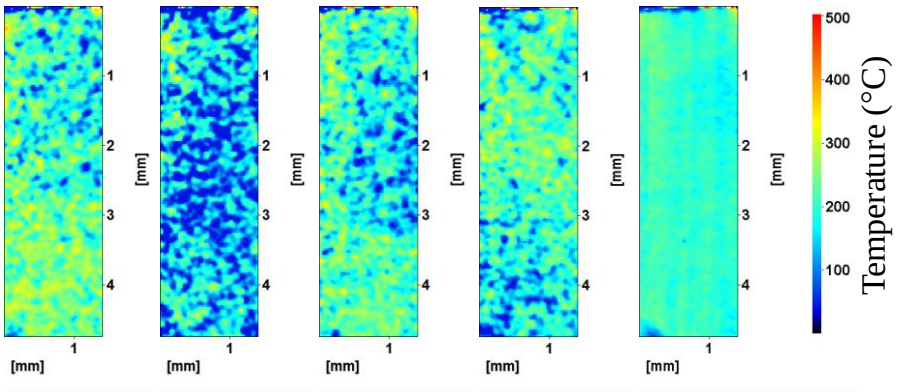

Figure 66: Four sample temperature field images (left four) and a 200 cycle average (right) at 44°BTDC with 45°C intake temperature. The top of the image coincides with the apex of the pent roof combustion chamber.

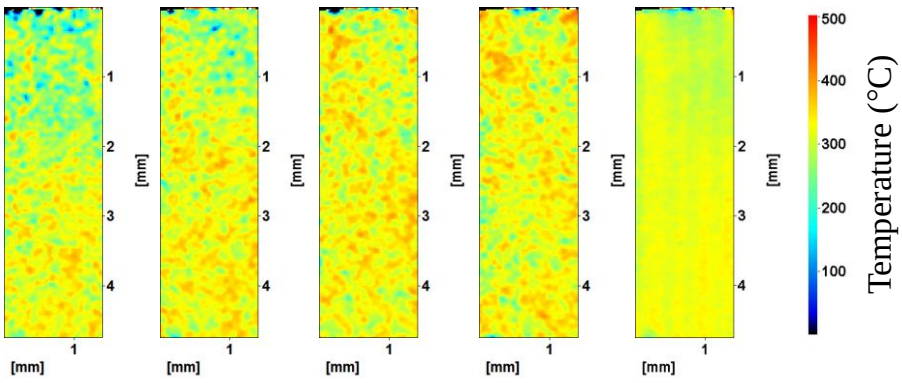

Figure 67: Four sample temperature field images (left four) and a 200 cycle average (right) at 26°BTDC with 45°C intake temperature. The top of the image coincides with the apex of the pent roof combustion chamber.

In the compression stroke in engines, micro-turbulent length scales have been estimated to be on the order of ~1 mm in engines, and the smallest length scale (the Kolmogorov scale) has been estimated to be on the order of ~10 µm (Heywood, 1988). Micro-turbulent length scales vary little with engine speed. Structures appear to be evident on the micro-turbulent length scales, although a larger field of view is necessary to fully resolve the structures. In the second image from the left in Figure 66, the entire

field of view may reside inside of a larger structure, indicating that measurements with a larger field of view are necessary. Speckle in the images is on the order of the Kolmogorov scale. However, since the light sheet thickness was an order of magnitude larger than this length, structures on this scale would probably be averaged out, so the speckle is most likely due to shot noise.

Spatial RMS and spatial AVG values were extracted from 1 mm x 1 mm data analysis windows near the wall and furthest away from the wall to calculate the spatial fluctuation intensity (spatial RMS/spatial AVG). This is an imperfect metric aimed at identifying cycles which have a gradient, or edge of a micro-scale structure, since these cycles should have a higher spatial RMS than those merely with shot noise. The results of the calculations can be seen in Figure 68 and Figure 69, respectively. At 44°BTDC, the spatial fluctuation intensity near the wall is marginally higher than that closer to the core, but nearly the same. Images showed cold pockets in the vicinity of the data analysis windows in the high spatial fluctuation intensity cycles. Distinct hot and cold pockets traveling into and away from the boundary layer would explain the extremely thin average thermal boundary layer thickness in this experiment. At 26°BTDC, the fluctuations are higher near the wall than near the core of the combustion chamber. A smaller degree of interaction between the regions would allow a thicker boundary layer to form. The magnitude of the spatial fluctuation intensity in these plots should be interpreted with caution since small variations in the LIF ratio at lower temperatures leads to large temperature swings (see Figure 57). It would therefore be expected that the

spatial fluctuation intensities at 44°BTDC are considerably larger than those at 26°BTDC.

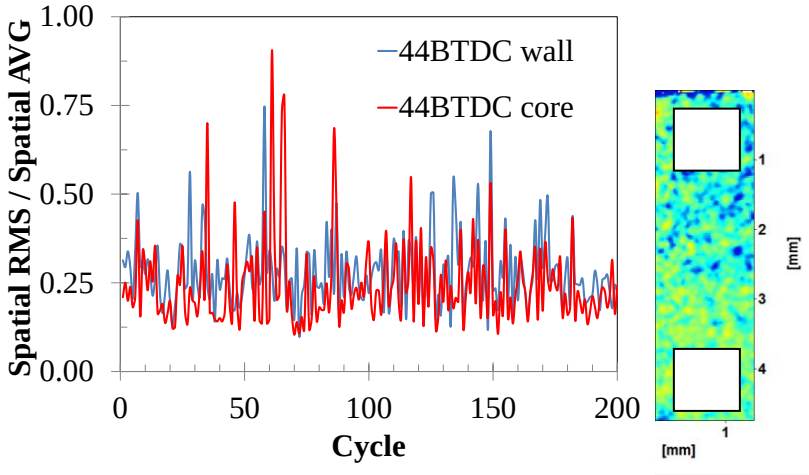

Figure 68: Fluctuation intensity (spatial RMS/spatial AVG) in 1 mm x 1 mm data analysis windows at 44°BTDC with 45°C intake temperature at the wall and near the core of the combustion chamber. The placement of the windows can be seen in the sample image (right).

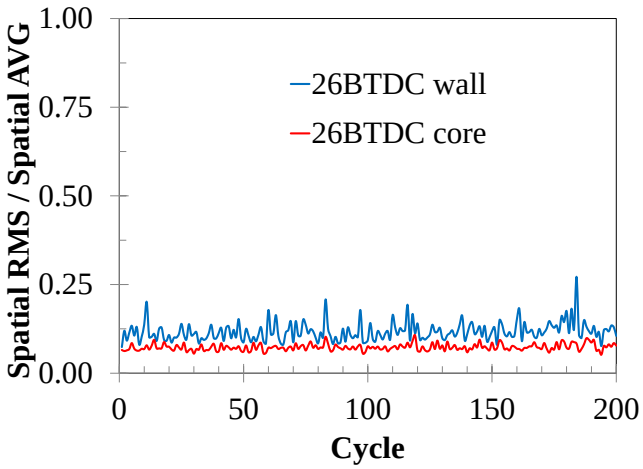

Figure 69: Fluctuation intensity (temporal RMS/temporal AVG) in a 1 mm x 1 mm data analysis window at 26°BTDC with 45°C intake temperature at the wall and near the core of the combustion chamber.

6.3.2 Low Spatial Resolution Measurements

An f = 100 mm UV lens (Sodern Cerco) and new light sheet optics were then installed. The low spatial resolution measurements also revealed a lateral gradient in the ratio images, so they were normalized by homogeneous temperature field images as described above.

Sample single shot images along with a 200 cycle average taken at 44°BTDC are shown in Figure 70. The blacked out areas are regions where the LIF is distorted (between 6-12 mm is the interface between two windows, and below ~15 mm was unusable due to piston ring carbon deposits. The light sheet impinged on the cylinder head slightly offset with respect to the apex of the pent roof cylinder head, in the center of the combustion chamber. Structures appear to be apparent in the single shot images. The first, second, and fourth image from the left could be showing flares similar to those observed traveling on a cold plate in the images presented in Chapter 5. High-speed measurements would help confirm this observation since the structures could be tracked in time and space. The third image from the left shows a considerably larger cold region near the wall, suggesting that even larger FOVs would be interesting to investigate. The averaged image on the right suggests that a 1D thermal boundary layer exists, which emphasizes the importance of temporally resolved measurements.

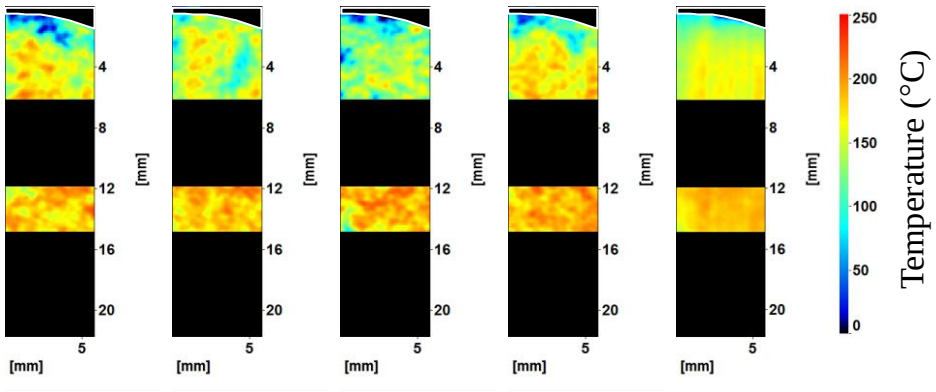

Figure 70: Sample single shot images (left 4) and 200 cycle average image (right) taken at 600 rpm at 44°BTDC, with 45°C intake, oil, and coolant temperature. Structures are apparent near the wall in single shot images, while the averaged image merely shows a 1D thermal boundary layer.

Data analysis windows are again used to calculate the spatial fluctuation intensity to identify the presence of these structures. A 2 mm x 2 mm window (20 x 20 pixel window) was selected near the wall and in the core of the combustion chamber. Note that the window near the wall is close to being in-between the windows used in the high spatial resolution measurements. The results at 44°BTDC and 26°BTDC can be seen in Figure 71 and Figure 72, respectively. The intensities in the near wall window in the 44°BTDC images supports the observation in the high resolution images that there is a high level of interaction of the two windows and their surroundings at this particular CAD and intake temperature (45°C). Intensities in the core of the chamber are considerably lower, as expected. Past measurements by Smith also indicated fluctuations on the order of 5-10% in the core of the combustion chamber (Smith J. R., 1980). The intensities at 26°BTDC near the wall are only marginally higher than in the core of the combustion chamber. Since this window is ~2 mm away from the wall, it is well outside of what the averaged profiles suggest is the thermal boundary layer.

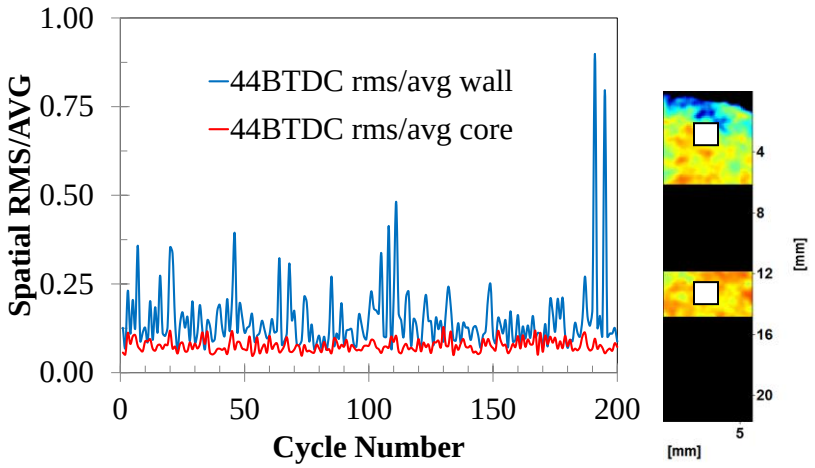

Figure 71: Spatial RMS/spatial AVG in 2 mm x 2 mm windows near the wall and in the core of the combustion chamber at 44°BTDC. Significant differences are seen. The approximate locations of the data analysis windows can be seen in the figure on the right.

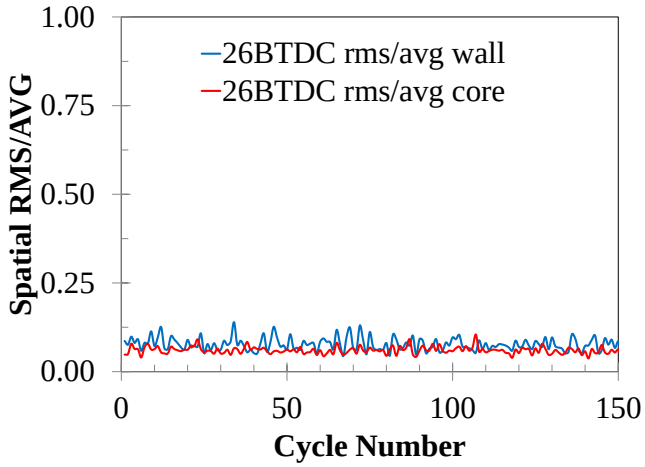

Figure 72: Spatial RMS/spatial AVG in 2 mm x 2 mm windows near the wall and in the core of the combustion chamber 26°BTDC.

One possible influence on the data is steering of the LIF due to varying index of refractions between the fluorescing tracer molecules and the camera. This has been observed in experiments by Fuyoto et al., but in a flat flame burner with the flow moving parallel to a cooled surface which is quite different than the experimental configurations

in this work (Fuyuto, et al., 2010). While the current work has made considerable progress in developing the technique and provided insight into the results that can be extracted from the data, this effect should be investigated in the future. It would be more difficult to correct for this effect using the image splitter in the current work because each channel of the LIF travels through different paths within the combustion chamber before it reaches the detector. The effects may then be different from image to image.

6.4 Conclusions

Two color toluene temperature diagnostics were demonstrated in an engine using a single camera approach with an image splitter. Two different lenses were used; a long distance microscope and a f = 100 mm UV lens. Although the measurements presented produced one image per engine stroke, it is noteworthy that the technique is capable of being extended to high speeds with the acquisition of a commercially available frequency-quadrupled Nd:YAG laser.

High spatial resolution measurements yielded quantitative boundary layer profiles with measurements ~23 μm apart. Measurements as close to 0.1 mm from the wall were found to be minimally affected by laser reflections and the subsequent subtraction from the LIF images. Boundary layer profiles at 44°BTDC, 26°BTDC, and TDC with 45°C and 90°C N_2 intake streams indicated that the diagnostics were working as expected. The boundary layers appeared to be thinner than the thermal boundary layers measured by Lyford-Pike and Heywood and Lucht et al., and the velocity boundary layers measured by Alharbi, in all cases but one which was similar in magnitude. No trend in boundary layer thickness was observed with progression in the engine cycle.

The boundary layer profiles at 44°BTDC and 26°BTDC (both with a 45°C intake stream) were then non-dimensionalized and compared against the predictions of a generalized thermal boundary layer development and five different RANS models. The

normalization is thought to be necessary because of the use of dielectric filers and the associated varying transmission with varying angle of incident light. Although errors were significant, a comparison is still warranted, particularly of the shapes of the profiles. The measurements at 44°BTDC indicated a boundary layer much thinner and flatter than all six predictions. At 26°BTDC, the shape of the boundary layer profile matched the shape of the Han and Reitz and Rakopolous et al. model predictions fairly closely.

High resolution and low resolution images showing an artificial gradient were normalized by a homogeneous temperature field ratio image for analysis. Single shot images showed the presence of micro-turbulent lengh scale pockets of hot and cold gases. Low resolution images showed flares similar to those presented in Chapter 5. These cycle-to-cycle variations could potentially influence engine behavior. Data analysis windows were selected for each set of images, and the spatial fluctuation intensity was calculated. Windows near the wall showed higher spatial fluctuation intensities than those further away from the wall, with the exception of the high resolution images at 44°BTDC which showed nearly equal intensities. The spatial fluctuation intensity metric is overly sensitive to the presence of cold pockets and noise since the sensitivity of the diagnostics is low at low temperatures for the single camera technique. The two camera approach using two different intensifiers (and gains) can be used to mitigate this effect.

A great deal could be learned from this diagnostic technique with the acquisition and use of a high speed laser. Comparisons can then be made at more CADs over hundreds of consecutive cycles. Additional friction velocity measurements from micro-

PIV data at CADs later in the compression stroke would allow comparisons to be made with profiles at 26°BTDC. Temperature measurements in air should then be attempted, with and without combustion.

CHAPTER 7
CONCLUSIONS AND PERSPECTIVES

Advanced combustion devices such as spark ignition direct injection spray guided stratified charge (SIDI SG SC) engines require precise control of the thermo-chemical processes in-cylinder to maximize fuel efficiency and reduce emissions. These processes can involve mixing on bulk and micro scales; compression; spray penetration and evaporation; heat transfer; temperature, pressure, and species heterogeneities; ignition; flame propagation; and wall interactions. In order to control these processes, they must first be understood through non-intrusive measurements. Optical diagnostics have emerged as a useful approach to these measurements.

A commonality between the high level processes mentioned above is that they all involve heterogeneities. A primary example of mixing processes is in the SIDI SG SC engine, where fuel mixes with the oxidizer milliseconds before ignition. Without optical diagnostics capable of measuring this mixing process, a trial and error approach with many hardware iterations would be necessary to achieve stable combustion and avoid misfires and partial burns. Flame propagation studies would have to be done using pressure transducers. The interaction of gases in the core of the combustion chamber with the cold boundary layer simply could not be measured; only the heat flux through the wall could be measured. While the development of optical diagnostics to measure heterogeneities has been ongoing for decades, advances in technology and scientific

knowledge continue to enable new generations of optical diagnostic techniques which are capable of exploring unchartered territory. This work describes the development of new and improved diagnostics.

High speed (CAD resolved) fuel concentration measurements were one area that could benefit from additional attention. These measurements are particularly useful for investigating combustion stability in advanced ICEs such as the SIDI SG SC engine. High speed planar fuel concentration measurements were used simultaneously with a spark plug absorption probe in this work.

Prior to this work, high speed planar fuel concentration measurements for use in an optical engine had lacked suitable signal to noise ratios to be used in an industrial laboratory setting. The measurements had not been shown to simultaneously indicate flame front, or observe fuel outgassing from crevice volumes. However, the scientific knowledge generated by this previous work had enabled the current work. The signal to noise ratio was improved; the ability of the technique to observe the flame front in lean combustion conditions was demonstrated; and the ability to image outgassing was demonstrated. Increasing laser pulse energy (using a simultaneously fired dual laser approach) had increased the signal to noise ratio to approximately 8.25:1 from 5:1. So-called homogeneous charge images appeared to have small gradients, which prompted a further study investigating fuel concentration heterogeneities in early injection cases. This would be a very interesting study for HCCI engine researchers, who are interested in this information for its impact on combustion phasing, noise, and durability. Although

this study was not successful due to time limitations and experimental difficulties, it is encouraging that these measurements may be possible despite the shot noise limitation of measurements of this type.

The spark plug absorption probe effectively measured these fuel heterogeneities in the early injection case. While this information is certainly interesting, a technique that can measure in 2D or 3D is more desirable. The probe was shown to be effective for use in SIDI SG SC engines with certain geometries. Also, since the probe was capable of measuring exhaust gases, important engine events were observed in the traces.

OH radical measurements are also an area which needed attention. LIF of hydroxyl radicals for ignition and extinction studies at high speeds has been complicated by the need for expensive and bulky dye lasers and pump systems. This work showed the potential for using a high speed frequency-quadrupled Nd:YLF laser emitting at 263 nm for excitation of OH. An intra-cavity frequency-doubled laser was externally frequency-quadrupled using a KD*P crystal. A commercial laser manufacturer may consider building an intra-cavity frequency-quadrupled laser for combustion system researchers. As will be discussed later, this source could have multiple applications.

The last area to be discussed is temperature field diagnostics and their application to ICEs. Several different diagnostic strategies have been developed and applied in previous studies; each with their own strengths and drawbacks. It was determined that a single laser, two detection band approach was best suited for quantitative, 2D

measurements in engines. This approach required only one laser, one intensified camera, and is insensitive to tracer number density. Note that both LIF and spark plug absorption probe measurements described in this work showed that, for direct injection, a uniform tracer number density is not achieved with early injection. Therefore, since most all advanced ICEs have direct injection, a system to create a premixed stream of intake air and tracer must be added (which resembles an old ICE technology; port fuel injection). Prior to this work, the single laser, two detection band approach had utilized a 248 nm excimer laser. Commercial lasers operating at this wavelength are not capable of repetition rates for CAD resolved measurements at useful engine speeds. The approach taken in this work utilized a frequency-quadrupled Nd:YAG laser emitting at 266 nm. Measurements in a heated jet demonstrated that the technique had worked, and measurements of the heated jet impinging on a cold, polished, metal surface had demonstrated that the technique worked near surfaces. These were the first high speed measurements of its kind, which are presented in Chapter 5.

An understanding of in-cylinder temperature, thermal boundary layers, and heat transfer is becoming increasingly important in the development of advanced internal combustion engines. SIDI SG SC engine misfiring cycles have recently been shown probabilistically to have flames that interact with the cylinder head boundary layer. Also, HCCI engine combustion phasing, noise, and durability are thought to be dependent upon temperature distribution and the hot core gas interaction with the cold boundary layer walls. This knowledge has generated interest in learning more about thermal boundary layers. However, prior to this work, there have simply not been any published attempts

with sufficient spatial and temporal resolution to resolve the thermal boundary layer in an ICE. Previous work has generated thermal boundary layer thicknesses and point-wise cycle-averaged temperatures at several locations within the boundary layer. Low spatial resolution 2D LIF measurements in a plane nearly parallel to the wall were made, along with unpublished work in a plane perpendicular to the wall. However, these LIF measurements were dependent upon uniform tracer number density and laser light intensity. What was needed in a diagnostic system and experiment was some combination off all of the desirable measurement characteristics, and this was provided in the current work.

Temporally and spatially resolved boundary layer profiles were measured and described in Chapter 6. High speed equipment was used, with the exception of a high speed laser because one was not available. The results showed thinner boundary layers than previous work. No trend was observed in boundary layer thickness as the engine cycle progressed. Experiments at 44°BTDC and 26°BTDC were non-dimensionalized and compared against the prediction of a generalized turbulent boundary layer treatment and five different RANS models. At 44°BTDC, the measurements showed a considerably thinner boundary layer and flatter profile than all predictions. The models should be reconsidered in this light. At 26°BTDC, the measurements showed a profile that was similar in shape to the Han and Reitz and Rakopolous et al. models.

High resolution and low resolution temperature field images were then presented. Single shot images showed the presence of micro-turbulent lengh scale pockets of hot

and cold gases, and low resolution images showed flares similar to those presented in Chapter 5. Data analysis windows were selected for each set of images, and the spatial fluctuation intensity was calculated. Windows near the wall showed higher spatial fluctuation intensities than those further away from the wall, with the exception of the high resolution images at 44°BTDC which showed nearly equal intensities. The spatial fluctuation intensity metric is overly sensitive to the presence of cold pockets (and merely sensitive to hot pockets) and noise since the sensitivity of the diagnostics is low at low temperatures for the single camera technique. The two camera approach using two different intensifiers (and gains) can be used to mitigate this effect.

With the utility of the technique demonstrated, it is a natural progression to extend it to high speeds and make further comparisons against RANS models. In addition, the results can guide next-generation heat transfer models which would rely on LES. Cycle-to-cycle variations can be represented in LES models and should be better able to account for the structures observed in the current work.

In addition to extending the technique to high speeds, the diagnostics have the potential to be used to simultaneously measure velocity fields (via PIV) and flame front (via OH LIF). The single camera and image splitter setup may allow for a 45 degree filter to be installed to reflect Mie scattering from oil droplets for PIV. Two approaches could be used to acquire OH signals. As demonstrated in Chapter 4, OH radicals can be excited with a frequency-quadrupled Nd:YLF laser emitting at 263 nm. The temperature red-shift behavior of toluene exists when excited at 248 nm and 266 nm, and will likely

do the same at 263 nm. Alternatively, a tunable frequency-quadrupled Nd:YAG laser emitting at 266.188 nm could be used to excite OH via the A-X (2,0) $P_1(10)$ line (Sick & Wermuth, 2004). If flame luminosity can be adequately suppressed, either through engine operation or filters, temperature can be measured in unburned regions. The OH emission spectrum when excited at 266.188 nm can be seen in Figure 73. The fluorescence would be detected in both channels individually, and with a ratio that is likely quite different than the toluene temperature ratio measurements.

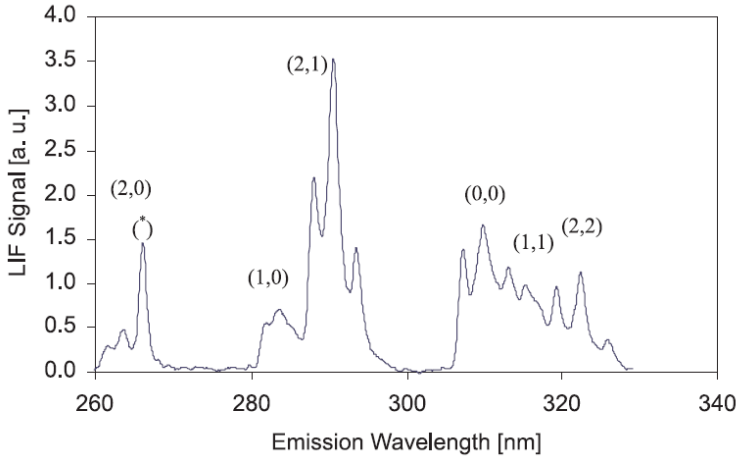

Figure 73: Emission spectrum of OH radicals after excitation with 266.188 nm light. The vibrational bands are indicated in parenthesis (v', v") (Sick & Wermuth, 2004). The spectrum will show up in both the red and blue channels, but will very likely have a different signal level and should be detectable.

BIBLIOGRAPHY

Aculight Corporation. (2004 йил 25-May). *Patent Storm*. Retrieved 2009 йил 20-May from Methods and devices for efficient generation of ultraviolet light - US Patent 6741620: http://www.patentstorm.us/patents/6741620/description.html

Adrian, R. (2007). Hairpin Vortex Organization in Wall Turbulence. *Physics of Fluids*, 041301-041301-16.

Alharbi, A. (2010). *High-Speed High-Resolution Vector Field Measurements and Analysis of Boundary Layer Flows in an Internal Combustion Engine.* Ann Arbor: University of Michigan.

Alkidas, A. (1980). Heat Transfer Characteristics of a Spark-Ignition Engine. *Transactions of the ASME: Journal of Heat Transfer*, 189-193.

Allocca, L., Alfuso, S., De Vita, A., Montanaro, A., & Rosa, P. (2004). Experimental Study of High Pressure Sprays for SIDI Engines. *11th International Symposium on Flow Visualization.* Notre Dame.

Angelberger, C., Poinsot, T., & Delhaye, B. (1997). Improving Near-Wall Combustion and Wall Heat Transfer Modeling in SI Engine Computations. *SAE*(SAE Paper 972881).

Annand, W. J. (1963). Heat Transfer in the Cylinders of Reciprocating Internal Combustion Engines. *Proceedings of the Institution of Mechanical Engineers, 177*(36), 973-996.

Annand, W. J., & Ma, T. H. (1970-1971). Instantaneous Heat Transfer Rates to the Cylinder Head Surface of a Small Compression-Ignition Engines. *Proceedings of the Institution of Mechanical Engineers*, 976-987.

Arcoumanis, C., & Kamimoto, T. (2009). *Flow and Combustion in Automotive Engines.* Verlag Berlin Heidelberg: Springer.

Arnold, A., Lange, B., Bouche, T., Heitzmann, T., Schiff, G., W., K., et al. (1992). Absolute temperature fields in flames by 2D-LIF of OH using excimer lasers and CARS spectroscopy. *Physical Chemistry, 96,* 1388-1392.

Baritaud, T., & Heinze, T. (1992). Gasoline Distribution Measurements with PLIF in a SI Engine. *Society of Automotive Engineers, 101*, 922355.

Barker, J. R. (1995). *Progress and problems in atmospheric chemistry* (Vol. 3). Singapore: World Scientific.

Bechtel, J., & Blint, R. (1980). Structure of a Laminar Flame-Wall Interface by Laser Raman Spectroscopy. *Applied Physics Letters, 37*(6), 576-578.

Behina, M., Parneix, S., Shabany, Y., & Durbin, P. A. (1999). Numerical Study of Turbulent Heat Transfer in Confined and Unconfined Impinging Jets. *International Journal of Heat and Fluid Flow*, 1-9.

Berg, T., Beushausen, V., Thiele, O., & Voges, H. (2006). Fibre optics spark plug sensor for the optimisation of engine combustion processes. *Motortech. Z.*, *67*, pp. 2-6.

Beyrau, F., Brauer, A., Seeger, T., & Leipertz, A. (2004). Gas-phase temperature measurements in the vaporizing spray of a gasoline direct-injection injector by use of pure rotational coherent anti-stokes raman scattering. *Optics Letters*, 247-249.

Board on Energy and Environmental Systems. (n.d.). *The National Academies Press*. Retrieved 2009 йил 5-May from Review of the Research Program of the FreedomCAR and Fuel Partnership: Second Report: http://books.nap.edu/openbook.php?record_id=12113&page=5

Böhm, B., Heeger, C., Boxx, I., Meier, W., & Dreizler, A. (2009). Time-resolved conditional flow field statistics in extinguishing turbulent opposed jet flames

using simultaneous highspeed PIV/OH-PLIF. *Proceedings of the Combustion Institute, 32*(2), 1647-1654.

Bork, B., Bohm, B., Heeger, C., & Chakravarthy, S. R. (2010). 1D High-Speed Rayleigh Measurements in Turbulent Flames. *Applied Physics B: Lasers and Optics, 101*, 487-491.

Borman, G., & Nishiwaki, K. (1987). Internal-Combustion Engine Heat Transfer. *Progress in Energy and Combustion Science*, 1-46.

Bright Crystals Technology Inc. (n.d.). *Bright Crystals Technology INC*. Retrieved 2009 йил 20-May from CLBO-Cesium lithium borate, is a newly developed nonlinear optical crystal.: http://www.brightcrystals.com/english/readnew.asp?NewsID=4916

Brouwer, L. D., Müller-Markgraf, W., & Troe, J. (1988). Thermal Decomposition of Toluene: A Comparison of Thermal and Laser-Photochemical Activation Experiments. *The Journal of Physical Chemistry*, 4905-4914.

Burton, C. S., & Noyes Jr., W. A. (1968). Electronic Energy Relaxation in Toluene Vapour. *Journal of Chemical Physics, 49*, 1705.

Caton, J. (2011). Heat Transfer Characteristics of Conventional and High Efficiency Reciprocating Engines. *7th US National Combustion Meeting.* Atlanta: Combustion Institute.

Chang, J., Guralp, O., Filipi, Z., Assanis, D., Kuo, T. W., Najt, P., et al. (2004). New Heat Transfer Correlation for an HCCI Engine Derived from Measurements of Instantaneous Surface Heat Flux. *SAE*(SAE Paper 2004-01-2996).

Cho, K. (2003). *Characterization of Combustion & Heat Transfer in a Direct Injection Spark Ignition Engine Through Measurements of Instantaneous Combustion Chamber Surface Temperature.* Ann Arbor: University of Michigan.

Clemens, N. (2002). Flow Imaging. In J. Hornak, *Encyclopedia of Imaging Science and Technology* (pp. 390-419). New York: John Wiley and Sons.

Cundy, M. (2008). *Development of high-speed optical diagnostics for the investigation of combustion instabilities in a spark ignition direct injection gasoline engine.* Ann Arbor: University of Michigan.

Cundy, M., & Sick, V. (2009). Hydroxyl Radical Imaging at kHz Rates using a Frequency-Quadrupled Nd:YLF Laser. *Applied Physics B*, 241-245.

Cundy, M., Schucht, T., Thiele, O., & Sick, V. (2009). High-Speed Laser-Induced Fluorescence and Spark Plug Absorption Sensor Diagnostics for Mixing and Combustion Studies in Engines. *Applied Optics*, B94-B104.

Dao, K., Uyehara, O., & Myers, P. (1973). Heat Transfer Rates at Gas-Wall Interfaces in Motored Piston Engine. *SAE*, SAE Paper 730632.

Davidhazy, A. (1998 йил 22-December). *Rochester Institute of Technology*. Retrieved 2011 йил 6-May from Basics of Focusing Schlieren Systems: http://people.rit.edu/andpph/text-schlieren-focus.html

Dec, J., & Hwang, W. (2009). Characterizing the Development of Thermal Stratification in an HCCI Engine Using Planar-Imaging Thermometry. *SAE*(SAE Paper 2009-01-0650).

Dec, J., & Sjober, M. (2003). A Parametric Study of HCCI Combustion -- the Sources of Emissions at Low Loads and the Effects of GDI Fuel Injection. *SAE*(SAE Paper 2003-01-0752).

Demtröder, W. (1998). *Laser Spectroscopy: Basic Concepts and Instrumentation* (Vol. 2nd edition). Heidelberg: Springer.

Dieke, G. H., & Crosswhite, H. M. (1962). The ultraviolet bands of OH fundamental data. *Journal of Quantitative Spectroscopy and Radiative Transfer*, 97-200.

Drake, M. C., Fansler, T. D., Cundy, M., & and Sick, V. (2009). High-repetition-rate Mie scattering and particle-image-velocimetry for flow and combustion diagnostics in a direct-injection gasoline engine. *6th U. S. National Combustion Meeting.* Ann Arbor: The Combustion Institute.

Drake, M. C., Fansler, T. D., Solomon, A. S., & Szekely Jr., G. A. (2003). Piston fuel films as a source of smoke and hydrocarbon emissions from a wall-contolled spark-ignited direct-injection engine. *Society of Automotive Engineers*, 2003-01-0547.

Dronniou, N., & Dec, J. (2011 йил 22-February). Investigating the Development of Thermal Stratification from the Near-wall Regions to the Bulk-gas in an HCCI Engine with Planar Imaging Thermometry. *(AEC/HCCI Meeting Presentation)*.

Dutta Roy, S., & Gangopadhyay, S. (2009). A new walk-off compensated multipass scheme for large enhancement of conversion efficiency for fourth harmonic generation. *Applied Physics B*.

Eckbreth, A. (1996). *Laser Diagnostics for Combustion Temperature and Species* . Amsterdam: Gordon and Breach.

Eichelber, G. (1939). Some New Investigations on Old Combustion Engine Problems. *Engineering, 148*, 463-466 and 547-550.

Einecke, S., Schulz, C., & Sick, V. (2000). Measurement of Temperature, Fuel Concentration and Equivalence Ratio Fields Using Tracer LIF in IC Engine Combustion. *Applied Physics B: Lasers and Optics, 71*, 717-723.

Fajardo, C. M., & Sick, V. (2007). Flow field assessment in a fired spray-guided spark-ignition direct-injection engine based on UV particle image velocimetry with sub crank angle resolution. *Proceedings of the Combustion Institute, 31*, pp. 3023-3031.

Fajardo, C., & Sick, V. (2008). Development of a high-speed UV particle image velocimetry technique and application for measurements in internal combustion engines. *Experiments in Fluids*.

Fansler, T. D., & Drake, M. C. (2006). "Designer diagnostics" for developing direct-inection gasoline engines. *Journal of Physics: Conference Series, 45*, 1-17.

Fansler, T. D., Drake, M. C., & Böhm, B. (2008). High-speed Mie-scattering diagnostics for spray-guided gasoline engine development. *8th International Symposium on Internal Combustion Diagnostics.* Baden-Baden.

Fansler, T. D., Stojkovic, B., Drake, M. C., & Rosalik, M. E. (2002). Local fuel concentration measurements in internal combustion engines using spark-emission spectroscopy. *Applied Physics B*, 577-590.

Fansler, T., Drake, M., Duwel, I., & Zimmermann, F. (2006). Fuel-spray and spark-plug interactions in a spray-guided direct-injection gasoline engine. *Proceedings of the Seventh International Symposium on Internal Combustion Diagnostics* (pp. 81-97). Baden-Baden: AVL Deutschland.

Fissenewert, U., Sick, V., & Pucher, H. (2005). Characterization of combustion and NO formation in a spray-guided gasoline direct-injection engine using chemiluminescence imaging, NO-PLIF, and fast NO exhaust gas analysis. *SAE International Journal of Fuels and Lubricants, 114*, 786-803.

Fröhlich, K., & Borgmann, K. (2003). Potentials of Future Fuel Consumption Technologies. *Internationales Weiner Motorensymposium.* Vienna.

Fuyuto, T., Kronemayer, H., Lewerich, B., Brubach, J., Fujikawa, T., Akihama, K., et al. (2010). Temperature and Species Measurement in a Quenching Boundary Layer on a Flat-Flame Burner. *Experiments in Fluids*, 783-795.

Fuyuto, T., Kronemayer, H., Lewerich, B., Brubach, J., Fujikawa, T., Akihama, K., et al. (2010). Temperature and Species Measurement in a Quenching Boundary Layer on a Flat-Flame Burner. *Experiments in Fluids*, 783-795.

Gardon, R., & Akfirat, J. C. (1965). The Role of Turbulence in Determining Heat-Transfer Characteristics of Impinging Jets. *International Journal of Heat and Mass Transfer*, 1261-1272.

Garg, V. K., & Jayaraj, S. (1988). Boundary Layer Analysis for Two-Dimensional Slot Jet Impingement on Inclined Plates. *Journal of Heat Transfer*, 577-582.

General Motors. (n.d.). *General Motors*. Retrieved 2009 йил 12-May from GM Takes New Combustion Technology Out of the Lab and Onto the Road: http://www.gm.com/experience/fuel_economy/news/2007/adv_engines/new-combustion-technology-082707.jsp

Grossmann, F., Monkhouse, P. B., Ridder, M., Sick, V., & Wolfrum, J. (1996). Temperature and Pressure Dependences of the Laser-Induced Fluorescence of Gas-Phase Acetone and 3-Pentanone. *Applied Physics B*, 249-253.

Guibert, P., Modica, V., & Morin, C. (2006). Influence of pressure, temperature and gas phase composition on biacetyl laser-induced fluorescence. *Experiments in Fluids*, 245-256.

Han, Z., & Reitz, R. D. (1997). A Temperature Wall Function Formulation for Variable-Density Turbulent Flows with Application to Engine Convective Heat Transfer Modeling. *International Journal of Heat and Mass Transfer*, 613-625.

Han., D., & Steeper, R. R. (2002). An LIF Equivalence Ratio Image Technique for Multicomponent Fuels in an IC Engine. *Proceedings of the Combustion Institute, 29*, pp. 727-734.

Heywood, J. B. (1988). *Internal Combustion Engine Fundamentals*. New York: McGraw-Hill, Inc.

Hippler, H., Troe, J., & Wendelken, H. J. (1983). UV Absorption Spectra of Vibrationally Excited Toluene Molecules. *Journal of Chemical Physics, 78*(9), 5351-5357.

Hohenberg, G. F. (1979). Advanced Approaches for Heat Transfer Calculations. *SAE*(SAE Paper 790825).

Huber, K., Woschni, G., & Zeilinger, K. (1990). Investigations on Heat Transfer in Internal Combustion Engines under Low Load and Motoring Conditions. *SAE*, SAE Paper 905018.

Huh, K. Y., Chang, I. P., & Martin, J. K. (1990). A Comparison of Boundary Layer Treatments for Heat Transfer Modeling in SI Engine Computations. *SAE*(SAE Paper 900252).

Incropera, F., & Dewitt, D. (2006). *Fundamentals of Heat and Mass Transfer, 6th edition.* New York: John Wiley and Sons.

Kader, B. A. (1981). Temperature and Concentration Profiles in Fully Turbulent Boundary Layers. *International Journal of Heat and Mass Transfer, 24*, 1541-1544.

Kaiser, S., & Long, M. (2005). Quantitative Planar Laser-Induced Fluorescence of Naphthalenes as Fuel Tracers. *Proceedings of the Combustion Institute*, 1555-1563.

Kakuho, A., Nagamine, M., Amenomori, Y., Urushihara, T., & Itoh, T. (2006). In-Cylinder Temperature Distribution Measurement and its Application to HCCI Combustion. *SAE*, SAE Paper 2006-01-1202.

Ketterle, W., Schäfer, M., Arnold, A., & Wolfrum, J. (1992 йил February). 2D single-shot imaging of OH radicals using tunable excimer lasers. *Applied Physics B, 54*(2), 109-112.

Kittler, C., & Dreizler, A. (2007). Cinematographic imaging of hydroxyl radicals in turbulent flames by planar laser-induced fluorescence up to 5 kHz repetition rate. *Applied Physics B, 89*(2-3), 163-166.

Koban, W., Koch, J. D., Sick, V., Wermuth, N., Hanson, R. K., & Schulz, C. (2004). Predicting LIF Signal Strength for Tluene and 3-pentanone under Engine-Related Temperature and Pressure Conditions. *Proceedings of the Combustion Institute, 30*, 1545-1553.

Koban, W., Koch, J. D., Sick, V., Wermuth, N., Hanson, R. K., & Schulz, C. (2005). Predicting LIF signal strength for toluene and 3-pentanone under engine-related temperature and pressure conditions. *Proceedings of the Combustion Institute, 30*, pp. 1545-1553.

Koban, W., Koch, J., Hanson, R., & Schulz, C. (2004). Absorption and fluorescence of toluene vapor at elevated temperatures. *Physical chemistry chemical physics*, 2940-2945.

Koch, J. (2005). *Fuel Tracer Photophysics for Quantitative Planar Laser-Induced Fluorescence.* Menlo Park: Stanford University.

Koch, J. D., & Hanson, R. K. (2003). Temperature and Excitation Wavelength Dependencies of 3-Pentanone Absorption and Fluorescence for PLIF Applications. *Applied Physics B*, 319-324.

Kohse-Hoinghaus, K., & Jeffries, J. B. (2002). *Applied Combustion Diagnostics.* New York: Taylor & Francis.

Kojima, T., & Nishiwaki, K. (1994). Numerical Analysis of Heat Transfer in Heat Insulated Diesel Engines. *JSAE*, 133-140.

Kojima, T., Konno, S., Fujikawa, S., Yasui, K., Yoshizawa, K., Mori, Y., et al. (2000 йил 1-January). 20-W ultraviolet-beam generation by fourth-harmonic generation of an all-solid-state laser. *Optics Letters, 25*(1).

Landenfeld, T., Kufferath, A., & Gerhardt, J. (2004). Gasoline Direct Inection - SULEV Emission Concept. *Society of Automotive Engineers*, 2004-01-0041.

Launder, B. E., & Spalding, D. B. (1974). The Numerical Computation of Turbulent Flows. *Computer Methods in Applied Mechanics and Engineering*, 269-289.

Lawton, B. (1987). Effect of Compression and Expansion on Instantaneous Heat Transfer in Reciprocating Internal Combustion Engines. *Proceedings of the Institution of Mechanical Engineering: Part A*, 175-186.

Liu, K., & Pletcher, R. (2007 йил April). Compressibility and Variable Density Effects in Turbulent Boundary Layers. *Journal of Heat Transfer, 129*, 441-448.

Lozano, A. (1992). *Laser Excited Luminescent Tracers for Planar Concentration Measurements in Gaseous Jets.* Stanford University.

Lucht, R., Walter, T., Dunn-Rankin, D., Dreier, T., & Bopp, S. (1991). Heat Transfer in Engines: Comparison of CARS Thermal Boundary Layer Measurements and Heat Flux Measurements. *SAE*(SAE Paper 910722).

Luong, M., Koban, W., & Schulz, C. (2006). Novel Strategies for Imaging Temperature Distribution using Toluene LIF. *Second International Conference on Optical and Laser Diagnostics* (pp. 133-139). Institute of Physics Publishing.

Luong, M., Zhang, R., Schulz, C., & Sick, V. (2008). Toluene laser-induced fluorescence for in-cylinder temperature imaging in internal combustion engines. *Applied Physics B, 91*, 669-675.

Luque, J., & Crosley, D. R. (1999). *LIFBASE homepage v2.0.2*. (M.-9.-0. SRI International, Editor) From http://www.sri.com/psd/lifbase

Lyford-Pike, E., & Heywood, J. (1984). Thermal Boundary Layer Thickness in the Cylinder of a Spark-Ignition Engine. *International Journal of Heat and Mass Transfer*, 1873-1878.

Lytle, D., & Webb, B. W. (1994). Air Jet Impingement Heat Transfer at Low Nozzle-Plate Spacings. *International Journal of Heat and Mass Transfer*, 1687-1697.

Malcolm, G. P., Curley, P. F., & Ferguson, A. I. (1990). Additive-pulse mode locking of a diode-pumped Nd:YLF laser. *Optics Letters*, 1303-1305.

Maly, R. (1984). Spark Ignition: Its Physics and Effect on the Internal Combustion Engine. In J. Hillard, & G. Springer, *Fuel Economy in Road Vehicles Powered by Spark Ignition Engines* (pp. 91-148). New York and London: Plenum Press.

Martin, H. (1977). Heat and Mass Transfer between Impinging Gas Jets and Solid Surfaces. *Advances in Heat Transfer*, 1-60.

Meier, U., Wolff-Gaßmann, D., & Stricker, W. (2000). LIF imaging and 2D temperature mapping in a model combustor at elevated pressure. *Aerospace Science and Technology, 4*, 403-414.

Miller, J., Slipchenko, M., Meyer, T., Jiang, N., Lempert, W., & Gord, J. (2009 йил 1-May). Ultrahigh-frame-rate OH fluorescence imaging in turbulent flames using a burst-mode optical parametric oscillator. *Optics Letters, 34*(9), 1309-1311.

Mohri, K., Luong, M., Vanhove, G., Dreier, T., & Schulz, C. (2011). Imaging of the Oxygen Distribution in an Isothermal Turbulent Free Jet Using Two-Color Toluene LIF Imaging. *Applied Physics B*, 707-715.

Myers, J. P., & Alkidas, A. (1978). Effects of combustion chamber surface temperature on the exhaust emissions of a single-cylinder spark-ignition engine. *SAE*(SAE Paper 780642).

New York Times. (2008 йил 20-July). *Car Reviews*. Retrieved 2009 йил 5-May from A Sedan Fueled by the Future: http://www.nytimes.com/2008/07/20/automobiles/autosreviews/20AUTO.html

Nishiwaki, K. (1998). Modeling Engine Heat Transfer and Flame-Wall Interaction. *Proceedings of the 4th international symposium on "diagnostics and modelling of*

combustion in internal combustion engines (COMODIA 1998), (pp. 35-44). Kyoto.

Nusselt, W. (1923). Der Warmeubergang in der Verbrennungskraftmaschine (the Heat Transfer in the Internal Combustion Engine). *V. D. I. - Forschungsheft*, 264.

Nusselt, W. (1923). Heat exchange in a spray cooler. *Z. Ver Dtsch. Ing.*, 206.

Ossler, F., Metz, T., & Alden, M. (2001). Picosecond Laser-Induced Fluorescence from Gas-Phase Polycyclic Aromatic Hydrocarbons at Elevated Temperatures. I. Cell Measurements . *Applied Physics B: Lasers and Optics*, 465-478.

Oude Nijeweme, D. J., Kok, J. B., Stone, C. R., & Wyszynski, L. (2001). Unsteady in-cylinder heat transfer in a spark ignition engine: experiments and modelling. *Proceedings of the Institution of Mechanical Engineers, 215*(D), 747-760.

Overbye, V. D., Bennethum, J. E., Uyehara, O. A., & Myers, P. S. (1961). Unsteady Heat Transfer In Engines. *SAE*, 461-494.

Park, H. J. (2009). *Development of an In-Cylinder Heat Transfer Model with Variable Density Effects on Thermal Boundary Layers.* Ann Arbor: University of Michigan.

Peterson, B., & Sick, V. (2009). Simultaneous flow field and fuel concentration imaging at 4.8 kHz in an operating engine. *Applied Physics B*.

Peterson, K. H., Drake, M. C., Fansler, T. D., & Sick, V. (2009). Quantifying effects of spark-plug orientation in a direct-injection gasoline engine using high-repetition-rate particle-image velocimetry. *6th U. S. National Combustion Meeting.* Ann Arbor: The Combustion Institute.

Pope, S. B. (2000). *Turbulent Flows.* Cambridge: Cambridge University Press.

Rakopoulos, C. D., Kosmadakis, G. M., & Pariotis, E. G. (2010). Critical Evaluation of Current Heat Transfer Models Used in CFD In-Cylinder Engine Simulations and

Establishment of a Comprehensive Wall-Function Formulation. *Applied Energy*, 1612-1630.

Reboux, D., Puechberty, D., & Dionnet, F. (1994). A New Approach of Planar Laser Induced Fluorescence Applied to Fuel/Air Ratio Measurement in the Compression Stroke of an Optical S.I. Engine. *SAE*, SAE Paper 941988.

Rothamer, D. A., & Ghandhi, J. B. (2003). Determination of flame-front equivalence ratio during stratified combustion. *Society of Automotive Engineers*, 2003-01-0069.

Rothe, E. W., & Andresen, P. (1997). Application of tunable excimer lasers to combustion diagnostics: a review. *Applied Optics, 36*(18), 3971-4033.

Rothman, L. S., Jacquemart, D., Barbe, A., Benner, D. C., Birk, M., Brown, L. R., et al. (2005). The HITRAN 2004 molecular spectroscopic database. *Journal of Quantitative Spectroscopy Radiative Transfer, 96*(2), 139-204.

Sanders, S., Wang, J., Jeffries, J., & Hanson, R. (2001). Diode-Laser Absorption Sensor for Line-of-Sight Gas Temperature Distributions. *Applied Optics, 40*(24), 4404-4415.

Schetz, J. (2010). *Boundary Layer Analysis.* Reston, Va.: American Institute of Aeronautics and Astronautics.

Schulz, C., & Sick, V. (2005). Tracer-LIF diagnostics: quantitative measurement of fuel concentration, temperature and fuel/air ratio in practical combustion systems. *Progress in Energy and Combustion Science*, 75-121.

Seitzman, J. M., & Hanson, R. K. (1993 йил December). Two-line planar fluorescence for temporally resolved temperature imaging in a reacting supersonic flow over a body. *Applied Physics B, 57*(6), 385-391.

Sick, V., & Wermuth, N. (2004). Single-shot imaging of OH radicals and simultaneous OH radical/acetone imaging with a tunable Nd:YAG laser. *Applied Physics B, 79*, 139-143.

Sick, V., & Westbrook, C. (2009). Diagnostic implications of the reactivity of fluorescence tracers. *Proceedings of the Combustion Institute, 32*, pp. 913-920.

Sjoberg, M., Dec, J., Babajimopoulos, A., & Assanis, D. (2004). Comparing Enhanced Natural Thermal Stratification Against Retarded Combustion Phasing for Smoothing of HCCI Heat-Release Rates. *SAE*(SAE Paper 2004-01-2994).

Smith, J. D. (2006). *Development and Application of High Speed Optical Diagnostic Techniques for Conducting Scalar Measurements in Internal Combustion Engines.* Ann Arbor: University of Michigan.

Smith, J. D., & Sick, V. (2005). Crank-angle resolved imaging of biacetyl laser-induced fluorescence in an optical internal combustion engine. *Applied Physics B: Lasers and Optics, 81*(5), 579-584.

Smith, J. D., & Sick, V. (2005 йил November). High-speed fuel tracer fluorescence and OH radical chemiluminescence imaging in a spark-ignition direct-injection engine. *Applied Optics, 44*(31), 6682-6691.

Smith, J. D., & Sick, V. (2006). Quantitative, Dynamic Fuel Distribution Measurements in Combustion-Related Devices Using Laser-Induced Fluorescence Imaging of Biacetyl in Iso-Octane. *Proceedings of the Combustion Institute*, *31*.

Smith, J. D., & Sick, V. (2007). Quantitative, dynamic fuel distribution measurements in combustion-related devices using laser-induced fluorescence imaging of biacetyl in iso-octane. *Proceedings of the Combustion Institute* (pp. 747-755). Elsevier Inc.

Smith, J. D., & Sick, V. (2007). The Prospects of Using Alcohol-Based Fuels in Stratified-Charge Spark-Ignition Engines. *Society of Automotive Engineers*, 2007-01-4034.

Smith, J. R. (1980). Temperature and Density Measurements in an Engine by Pulsed Raman Spectroscopy. *SAE*(SAE paper 800137).

Smyth, K., & Crosley, D. (2002). Detection of Minor Species with Laser Techniques. In K. Kohse-Hösinghaus, & J. B. Jeffries, *Applied Combustion Diagnostics* (pp. 9-68). New York: Taylor and Francis.

Snyder, J., Dronniou, N., Dec, J., & Hanson, R. (2011). PLIF Measurements of Thermal Stratification in an HCCI Engine Under Fired Operation. *SAE*, SAE Paper 2011-01-1291.

Thurber, M. C., Grisch, F., & Hanson, R. K. (1997). Temperature Imaging with Single- and Dual-Wavelength Acetone Planar Laser-Induced Fluorescence. *Optics Letters*, 251-253.

U.S. Department of Energy. (2011 йил 21st-September). *U.S. Department of Energy*. Retrieved 2011 йил 30th-September from Fuel Table: http://www.afdc.energy.gov/afdc/pdfs/fueltable.pdf

U.S. Department of Energy. (n.d.). *Alternative Fuels & Advanced Vehicles Data Center*. Retrieved 2009 йил 5-May from Aleternative Fuel Vehicle Emissions: http://www.afdc.energy.gov/afdc/vehicles/emissions.html

Vlachos, D. G., Schmidt, L. D., & Aris, R. (1994). Ignition and Extinction of Flames Near Surfaces: Combustion of CH4 in Air. 1005-1017.

Wang, X., & Stone, C. (2008). A Study of Combustion, Instantaneous Heat Transfer, and Emissions in a Spark Ignition Engine During Warm-up. *Proceedings of the Institution of Mechanical Engineering: Part D; Journal of Automobile Engineering*, 607-618.

Warnatz, J., Maas, U., & Dibble, R. W. (1999). *Combustion.* Berlin: Springer.

Wendland, D. (1968). *The effect of periodic pressure and temperature fluctuations on unsteady heat transfer in a closed system.* Madison: University of Wisconsin.

Wermuth, N., & Sick, V. (2005). Absorption and Fluorescence Data of Acetone, 3-pentanone, Biacetyl, and Toluene at Engine-Specific Combinations of Temperature and Pressure. *Society of Automotive Engineers*, 2005-01-2090.

Wilson, N. D., Watkins, A. J., & Dopson, C. (1993). Asymmetric Valve Strategies and Their Effect on Combustion. *SAE*(SAE Paper 861530).

Woschni, G. (1967). A Universally Applicable Equation for the Instantaneous Heat Transfer Coefficient in the Internal Combustion Engine. *SAE*(SAE Paper 670931), 3065-3083.

Wu, X., & Moin, P. (2009). Direct Numerical Simulation of Turbulence in a Nominally Zero-Pressure-Gradient Flat-Plate Boundary Layer. *Journal of Fluid Mechanics*(630), 5-41.

Yalin, A. P., & Miles, R. B. (1999). Ultraviolet Filtered Rayleigh Scattering Temperature Measurements with a Mercury Filter. *Optics Letters, 24*, 590-592.

Yang, J., Pierce, P., Martin, J., & Foster, D. (1988). Heat Transfer Predictions and Experiments in a Motored Engine. *SAE*, SAE Paper 881314.

Zhang, R. (2007). *Tracer-Based Laser-Induced Fluorescence Diagnostics and their Application to Spark-Ignition Direct-Injection Engines.* Ann Arbor: University of Michigan.

Zhang, R., & Sick, V. (2007). Multi-Component Fuel Imaging in a Spray-Guided, Spark-Ignition, Direct-Injection Engine. *Society of Automotive Engineers*, 2007-71-46.

Zhang, R., Bohac, S., & Sick, V. (2006 йил January). Stability of isooctane mixtures with 3-pentanone or biacetyl as fluorescence tracers in combustion experiments. *Experiments in Fluids, 40*(1), 161-163.

Zhao, F., Lai, M. C., & Harrington, D. L. (1999). Automotive spark-ignited direct-injection gasoline engines. *Progress in Energy and Combustion Science*, 437-562.

Zhao, H., & Ladommatos, N. (1998). Optical Diagnostics for In-Cylinder Mixture Formation Measurement in IC Engines. *Progress in Energy and Combustion Science, 24*, 297-336.

Zimmermann, F., Koban, W., & Schulz, C. (2006). Temperature Diagnostics using Laser-Induced Fluorescence (LIF) of Toluene. *LACSEA.*